CONTENTS

ORIGINAL ARTICLES

MECHANICAL PROPERTIES AND STRUCTURAL FEATURES OF BUTT JOINTS PRODUCED AT FSW OF ALUMINIUM ALLOYS OF DIFFERENT ALLOYING SYSTEMS

A.G. Poklyatskyi[1], S.I. Motrunich[1], V.Ye. Fedorchuk[1], Iu.V. Falchenko[1], M. Sagul[2]

[1]E.O. Paton Electric Welding Institute of the NASU

11 Kazymyr Malevych Str., 03150, Kyiv, Ukraine

[2]Czech Technical University

16636, Prague, Czech Republic

ABSTRACT

The paper presents the results of investigations of the strength, hardness and structure of butt joints on aluminium alloys of different alloying systems, produced by friction stir welding (FSW). It is shown that this process allows producing sound joints of aluminium alloys of different alloying systems, both in similar and dissimilar combinations. This is true not only for aluminium alloys made by casting by the standard technological scheme, but also for granulated alloys, containing the oversaturated solid solution of refractory transition metals, produced by powder metallurgy. It is found that the strength of welded joints produced at FSW of aluminium alloys, depends on the chemical compositions and mechanical properties of these alloys. Maximum ultimate strength is demonstrated by welded joints of the following high-strength alloys: 1995 (483 MPa), 1963 (473 MPa) and D16 (441 MPa), which is due to a slight degree of metal softening in the thermomechanical impact zone (TMIZ), which is where the samples fail at mechanical stretching. Destruction of samples of welded joints of dissimilar aluminium alloys also runs in this zone or on its boundary with the heat-affected zone (HAZ) from the side of the softer alloy. Their ultimate strength is on the level of the joints of the respective similar alloys. It is shown that intensive plastic deformation of metal at FSW of dissimilar aluminium alloys results in formation of grains of practically globular shape in the weld nugget in the permanent joint zone, their size not exceeding 4–6 μm. In granulated alloy welding, the oversaturated solid solution is preserved in the granules, just their mechanical refinement takes place, resulting in a fine dense structure of the weld nugget, and the granules containing an oversaturated solid solution of refractory transition metals, are uniformly distributed over the entire volume of the matrix in the weld metal.

KEYWORDS: aluminium alloys, friction stir welding, hardness, strength, structure

INTRODUCTION

Aluminium alloys are widely used in manufacture of diverse flying vehicles, watercraft, railway, wheeled and tracked transport, building and bridge structures. This is largely due to obvious advantages of aluminium, compared to other structural materials: it is three times lighter than steel, has high corrosion resistance and electric conductivity, features considerable specific strength, antimagnetism and absence of cold-shortness threshold. Here, the majority of aluminium alloys are readily treatable and they can weld well that allows their application in manufacture of various structural components [1].

Depending on the functional purpose of such components, the required semi-finished products and respective alloying systems and compositions of aluminium alloys are selected for their manufacture. The world market proposes to users approximately three hundred compositions of structural aluminium alloys, which have different physicomechanical properties and are produced in the form of bars, flat, profiled, and extruded profiles, wires and foil [2, 3].

In addition to conventional aluminium alloys produced by the standard casting technology, the fraction of composite materials is growing in the proposed kinds of semi-finished products. These composite materials contain reinforcing particles of Al_2O_3 aluminium oxide, or SiC silicon carbide [4, 5]. It provides high values of the modulus of elasticity, wear and high-temperature resistance, as well as low values of specific weight and coefficients of thermal expansion and friction. Granulated aluminium alloys take up a significant place in the range of structural alloys, owing to application of powder metallurgy achievements. During their production it is possible to essentially increase the level of alloy doping by such refractory transition metals as chromium, zirconium, titanium, vanadium, etc., owing to a high rate of granule cooling during crystallization. At granule crystallization, these metals form anomalously oversaturated solid solutions. At further technological heating, dispersed intermetallics form owing to decomposition of such solid solutions, which ensures a significant hardening of the alloys [6, 7]. Creation of quasicrystalline materials should be noted among new achievements in the

Table 1. Chemical composition of the studied aluminium alloys

Alloy grade	Weight fraction of chemical elements, % (balance — Al)											
	Si	Fe	Cu	Mn	Mg	Cr	Zn	Ti	Zr	Li	Sc	Other
AMg5M	0.50	0.50	0.10	0.7	5.2	–	0.20	0.09	–	–	–	0.05 Be
AMg6M	0.40	0.40	0.10	0.8	6.3	–	0.20	0.10	–	–	–	0.05 Be
D16	0.50	0.50	4.5	0.7	1.6	0.10	0.25	0.15	0.05	–	–	–
1460	0.10	0.15	3.1	0.1	0.1	0.05	0.25	0.06	0.12	2.3	0.12	0.08 Be
6013	0.58	0.20	0.95	0.26	1.0	–	–	0.03	–	–	–	–
1963	0.15	0.25	1.9	–	2.9	–	6.8	–	0.15	–	–	–
1995	0.15	0.20	–	0.23	2.8	0.65	4.95	0.20	–	–	–	–
1419	0.15	0.20	–	2.0	–	1.05	–	0.60	0.60	–	–	0.60 V

sphere of manufacturing modern aluminium alloys. They contain intermetallics in the form of nanosized quasicrystalline particles, which ensure high physico-mechanical properties of such materials [8, 9].

However, realization of potential possibilities of such promising materials in welded structure fabrication largely depends on correct selection of the methods to produce sound permanent joints. While various welding processes are used with success for the majority of batch-produced alloys, the above-mentioned advanced materials require application of solid state welding so as to preserve the advantages of parent material in the welds [5, 10, 11].

Selection of materials during manufacture of welded structure components largely depends on their functional purpose and operating conditions. Therefore, in order to ensure certain properties of individual elements or components, it is necessary to weld not only similar, but also dissimilar aluminium alloys, which may differ both by the alloying system, and by their production method [3].

The objective of this work is evaluation of the effectiveness of application of friction stir welding (FSW) to produce sound joints of dissimilar aluminium alloys, including granulated ones.

MATERIALS, PROCEDURES AND EQUIPMENT

Aluminium alloys 2 mm thick of different alloying systems were used for investigations. Their composi-

Table 2. Mechanical properties of the studied aluminium alloys

Alloy grade	Ultimate strength σ_t, MPa	Yield limit $\sigma_{0.2}$, MPa	Relative elongation δ,%	Bend angle α, deg
AMg5M	338	161	21.8	180
AMg6M	359	220	22.3	96
D16	445	315	18.5	83
1460	486	445	17.7	37
6013	410	317	8.0	96
1963	560	530	6.3	54
1995	610	527	7.1	26
1419	300	260	12.8	115

tion is given in Table 1. Among the presented materials are common alloys (AMg5M, AMg6M and D16), advanced high-strength alloys (1460 and 1963) and 6013 alloy of increased high-temperature resistance, which were produced by the standard technological scheme, as well as 1995 and 1419 alloys produced using powder metallurgy. Mechanical properties of the studied alloy sheets are given in Table 2.

In keeping with the requirements to welded joints of critical structures, standard chemical etching of the sheets was performed in NaOH solution with subsequent clarification in HNO_3 solution, and directly before welding mechanical scraping of the sheet surfaces was conducted in the zone of weld formation.

FSW was performed in a laboratory unit developed at PWI at tool rotation frequency $N = 1420$ rpm, using a special tool with the shoulder of 12 mm diameter, and 1.85 mm long tip in the form of a truncated cone with 3.4 mm diameter at the shoulder base and 12° angle of inclination of the cone generatrix [12]. The produced welded joints were used to make sections for studying their structural features. The ultimate strength of welded joints was determined at static uniaxial tension of standard flat samples with 15 mm width of the working zone in an all-purpose servohydraulic system MTS 318.25. Structural features of the welded joints were evaluated using optical electron microscope MMT-1600B. Metal hardness in different zones of the produced butt welded joints was measured on the sample face surfaces in ROCKWELL instrument at loading $P = 600$ N.

INVESTIGATION RESULTS AND DISCUSSION

Conducted experimental studies showed that sound formation of aluminium alloy welds at FSW is ensured at different rates of linear displacement of the tool. So, optimal welding speed for AMg5M alloy at tool rotation frequency of 1420 rpm is equal to 16 m/h, and for 1460 alloy — 14 m/h, for AMg6M alloy — 12 m/h, and for D16 alloy it is 10 m/h. Sound welded joints of 6013 alloy can be produced at welding speed of
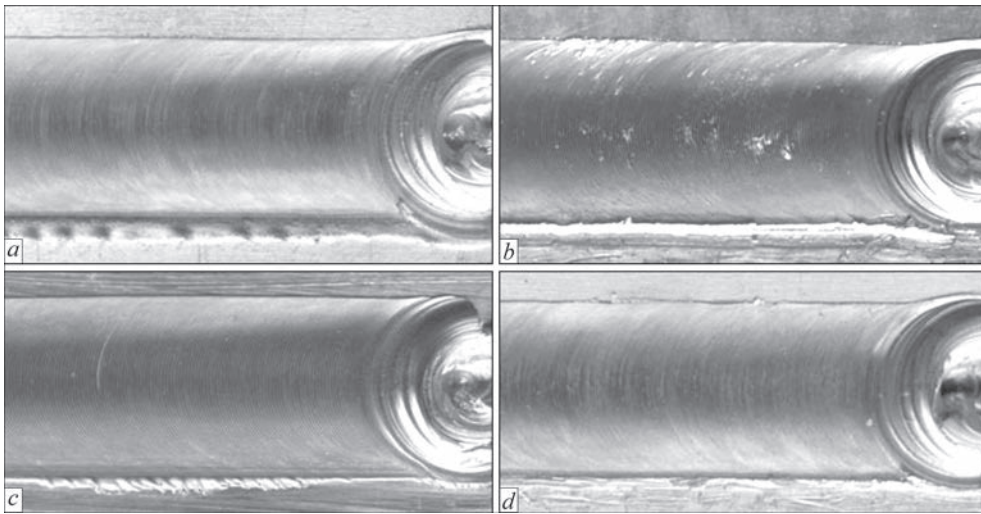
Figure 1. Appearance of the face surface of welds produced at FSW in the optimal modes of aluminium alloys in a similar combination: *a* — 6013; *b* — 1963; *c* — 1995; *d* — 1419
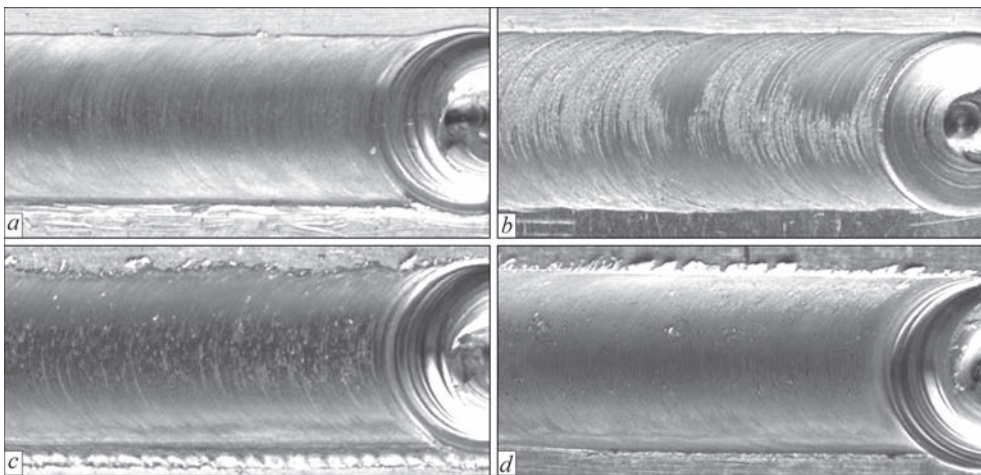
Figure 2. Appearance of the face surface of welds produced by FSW in the optimal modes of aluminium alloys in dissimilar combinations: *a* — AMg6M + 6013; *b* — AMg6M + 1419; *c* —1460 + 6013; *d* — 1460 + 1995 (the first specified alloy is placed on top — from the advancing side)

38 m/h, those of 1963 alloy — 10 m/h, 1995 and 1419 alloys — 26 m/h. Appearance of such welded joints is given in Figure 1.

Results of experimental studies showed that in order to produce sound joints of dissimilar aluminium alloys, FSW should be performed at a smaller speed of the tool linear displacement for the selected alloy pair that allows reducing the probability of development of internal weld defects in the form of discontinuities. Appearance of some sound butt welded joints of aluminium alloys in the dissimilar combination, produced by friction stir welding, is given in Figure 2.
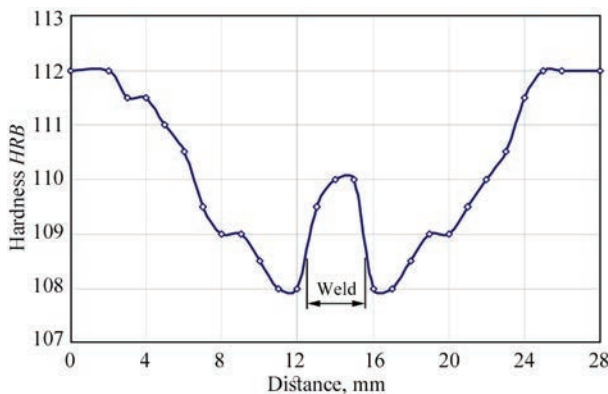
Figure 3. Hardness distribution in FSW butt joints of 2 mm aluminium alloy 1963
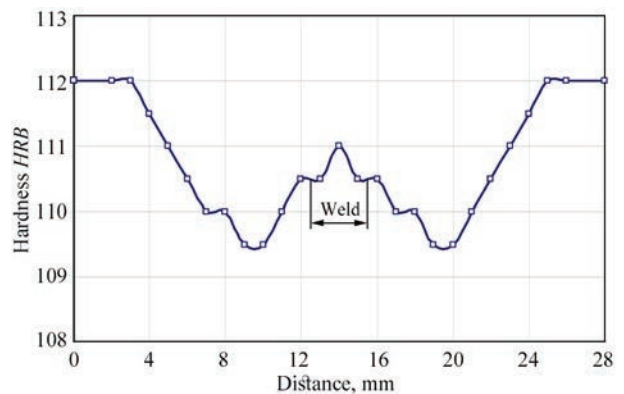
Figure 4. Hardness distribution in FSW butt joints of 2 mm granulated aluminium alloy 1995

5
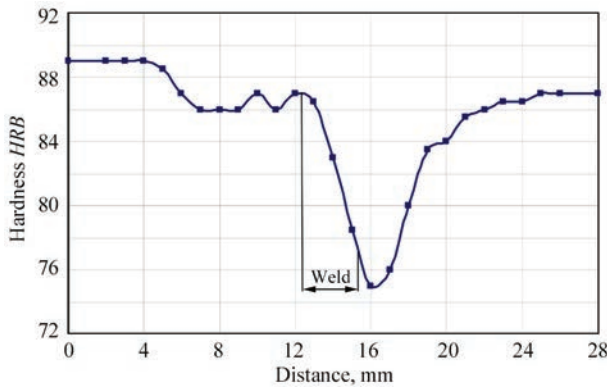
Figure 5. Hardness distribution in butt joints, produced at FSW of AMg6M alloy (left) to 1419 alloy (right) 2 mm thick
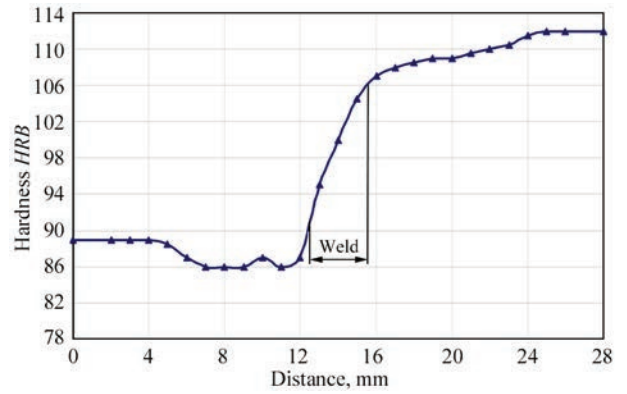
Figure 6. Hardens distribution in butt joints produced at FSW of AMg6M alloy (left) to 1963 alloy (right) 2 mm thick

Measurements of metal hardness in the welding zone showed that the degree of its softening depends on the aluminium alloy chemical composition. Here, for the majority of the alloys weld metal hardness is somewhat higher, that in the thermomechanical impact zone (TMIZ), due to formation of a fine-crystalline metal structure. So at FSW of 6013 alloy with a higher corrosion resistance the weld metal hardness is equal to *HRB* 87–88, and in TMIZ it is *HRB* 85–86. For high-strength 1963 alloy of Al–Cu–Mg–Zn alloying system the maximum degree of metal softening is also observed in the TMIZ, whereas in the weld it is on the level of *HRB* 109–110 (Figure 3).

Ductile low-alloyed granulated 1419 alloy has the hardness of weld metal and adjacent regions on the level of *HRB* 75–76, whereas for the base metal it is

Table 3. Ultimate strength of butt joints produced at FSW of similar aluminium alloys

Number	Alloy grade	Ultimate strength, MPa	Fracture site	Broken sample photo
1	AMg5M	315 <u>310</u> 313	HAZ TMIZ	
2	AMg6M	334 <u>329</u> 332	HAZ TMIZ	
3	D16	443 <u>439</u> 441	TMIZ/HAZ$_{ret}$	
4	1460	310 <u>307</u> 309	TMIZ	
5	6013	238 <u>230</u> 234	TMIZ/HAZ$_{ret}$	
6	1963	482 <u>462</u> 473	TMIZ	
7	1995	490 <u>478</u> 483	TMIZ	
8	1419	257 <u>253</u> 255	TMIZ	

equal to *HRB* 87 (Figure 6). At FSW of high-strength granulated 1995 alloy the degree of metal softening in the welding zone is quite small: in the weld metal hardness is equal to *HRB* 110.5–111.0, whereas for the base metal it is on the level of *HRB* 112, and in TMIZ it is equal to *HRB* 109.5–110.5 (Figure 4).

Measurements of metal hardness in the zone of formation of permanent joints, produced at dissimilar combination of aluminium alloys showed that compared to welding of similar alloys changes in metal hardness occur only in the welds and regions adjacent to them in TMIZ. So, for instance, in welding AMg6M alloy to 1419 alloy, the weld metal hardness from AMg6M side is equal to *HRB* 85–87, and from 1419 side it is *HRB* 77–79 (Figure 5).

Welding of AMg6M alloy to high-strength 1963 alloy ensures weld metal hardness on the level of *HRB* 90–95 from AMg6M side, and from 1963 side it is *HRB* 104–106 (Figure 6), while minimal metal hardness (*HRB* 86) is observed in TMIZ from the side of AMg6M alloy, as it is for similar joints of this alloy.

A similar situation is observed also in welding other studied joints of dissimilar aluminium alloys: an abrupt change of weld metal hardness or its smooth transition at a combination of dissimilar alloys take place. So, an abrupt change of weld metal hardness takes place in welding the following alloys to each other: AMg5M + 1995, AMg6M + 1963, AMg6M + 1419, 1460 + 6013 and 1460 + 1995, whereas the combination of AMg6M + 6013, D16 + 1963 and D16 = 1995 alloys ensures a smooth change of metal hardness in the joint zone. For instance, in welding AMg5M alloy to 1995 alloy weld metal hardness from the side of AMg5M alloy is on the level of *HRB* 84–90, whereas from the side of 1995 alloy it is much higher (*HRB* 104–108). In welding AMg6M alloy to 6013 alloy the weld metal hardness is approximately the same from both the sides (*HRB* 87–89).

Experimental studies revealed that at FSW of aluminium alloys in a similar combination, the strength of their welded joints and sample fracture site depend on the chemical compositions and mechanical proper-

Table 4. Ultimate strength of butt joints produced at FSW of dissimilar aluminium alloys

Number	Alloy grade	Ultimate strength, MPa	Fracture site	Broken sample photo
1	AMg5M + 1995	316 <u>309</u> 314	HAZ$_{AM5M}$ TMIZ$_{AM5M}$	
2	AMg6M + 6013	236 <u>231</u> 234	TMIZ /HAZ$_{6013}$	
3	AMg6M + 1963	336 <u>330</u> 333	HAZ$_{AMg6M}$ TMIZ$_{AMg6M}$	
4	AMg6M + 1419	259 <u>252</u> 256	TMIZ$_{1419}$	
5	D16 + 1963	445 <u>440</u> 442	TMIZ/HAZ$_{D16}$	
6	D16 + 1995	442 <u>439</u> 440	TMIZ/HAZ$_{D16}$	
7	1460 + 6013	237 <u>232</u> 234	TMIZ/HAZ$_{6013}$	
8	1460 + 1995	312 <u>306</u> 309	TMIZ$_{1460}$	
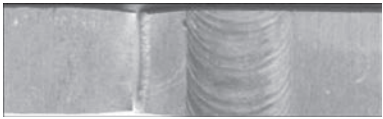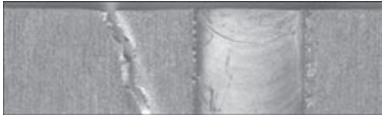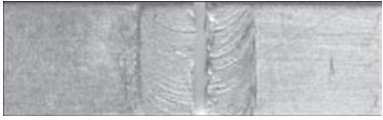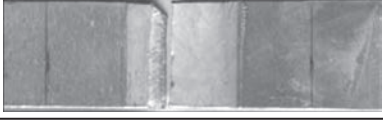
ties of the welded alloys (Table 3). In most cases the welded joint samples fail in TMIZ. Some samples of AMg65M and AMg6M alloys fail in the HAZ. Now, for D16 and 6013 alloy joints the characteristic site of sample destruction is the boundary between TMIZ and HAZ from the retreating side (HAZ_{ret}).

So, the maximum ultimate strength is found in welded joints of high-strength 1995 (483 MPa), 1963 (473 MPa) and D16 alloys (441 MPa) that is due to a slight (*HRB* <2.5) degree of metal softening in TMIZ, which is where the samples fail at static tension. At FSW of high-strength 1460 alloy a rather significant softening (*HRB* 24) of the metal takes place in the zone of permanent joint formation, resulting in ultimate strength of its welded joints being on the level of 309 MPa. Welded joints of 1419 (255 MPa) and 6013 alloys (234 MPa) have minimal ultimate strength that is also due to a high ($\approx$ *HRB* 12) degree of metal softening in TMIZ and lower strength of the base material.

At FSW of aluminium alloys in a dissimilar combination, the welded joint strength and sample destruction site also depend on the chemical composition and mechanical properties of the materials being welded (Table 4).

So, in welding AMg5M or AMg6M alloys to high-strength 1995 and 1963 alloys, which are only slightly softened here, the joint sample fracture runs in the HAZ or TMIZ from the side of AMg5M or AMg6M alloys, and their strength is the same, as in welding these alloys in a similar combination. The same regularities are preserved also in welding other alloys. For instance, welded joints of 1460 + 1995 alloys fail in TMIZ, and those of D16 + 1963 and D16 + 1995 alloys — on the boundary of TMIZ and HAZ from the side of 1460 and D16 alloys, which have lower strength. The ultimate strength of such joints of dissimilar alloys is on the level of joints of the respective similar alloys. Samples of joints, produced at FSW of AMg6M alloy to 6013 and 1419 alloys fail on the boundary of the HAZ and TMIZ from the side of lower-strength alloys.

As a result of experimental studies it was determined that in solid state friction stir welding of the above-mentioned aluminium alloys in a similar combination, grain refinement takes place in the zone of permanent joint formation as a result of intensive plastic deformation of the metal. In welding of alloys produced by the standard casting technology, grains
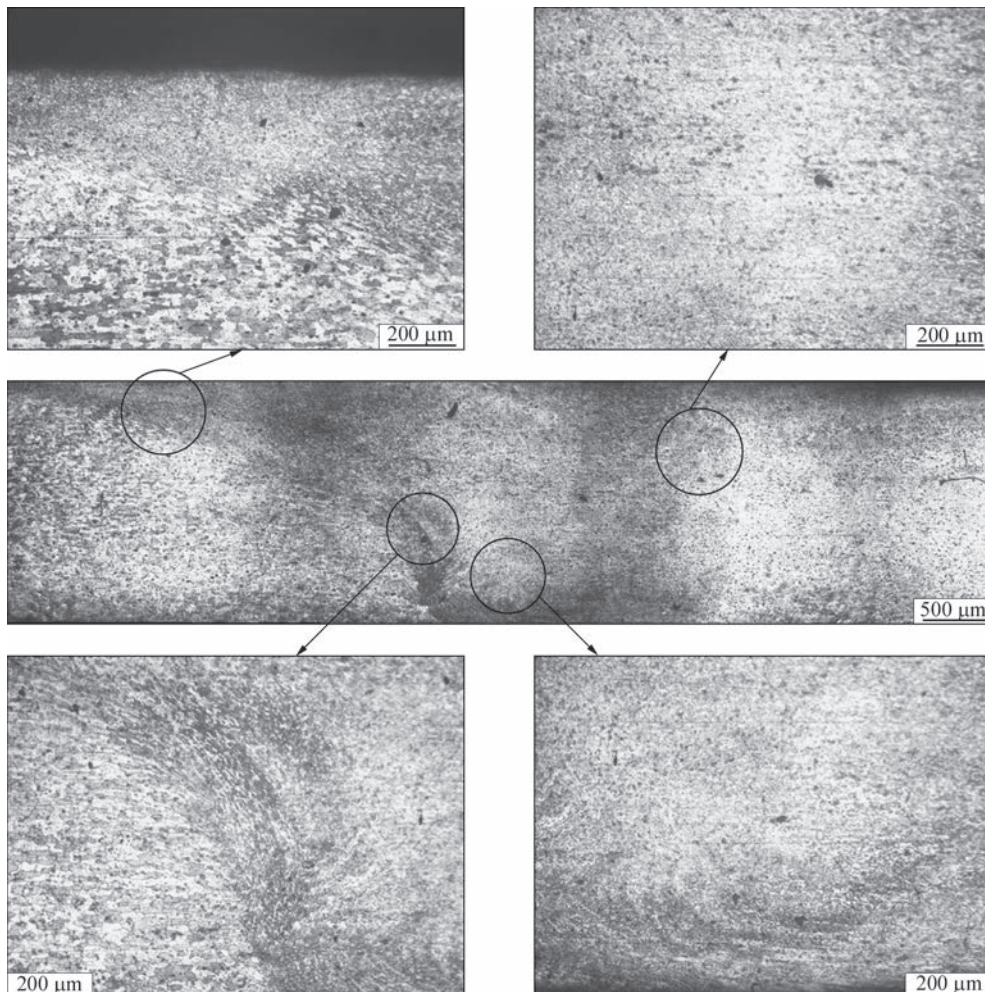
Figure 7. Microstructure of welded joint of 2 mm aluminium alloy 6013, produced by FSW
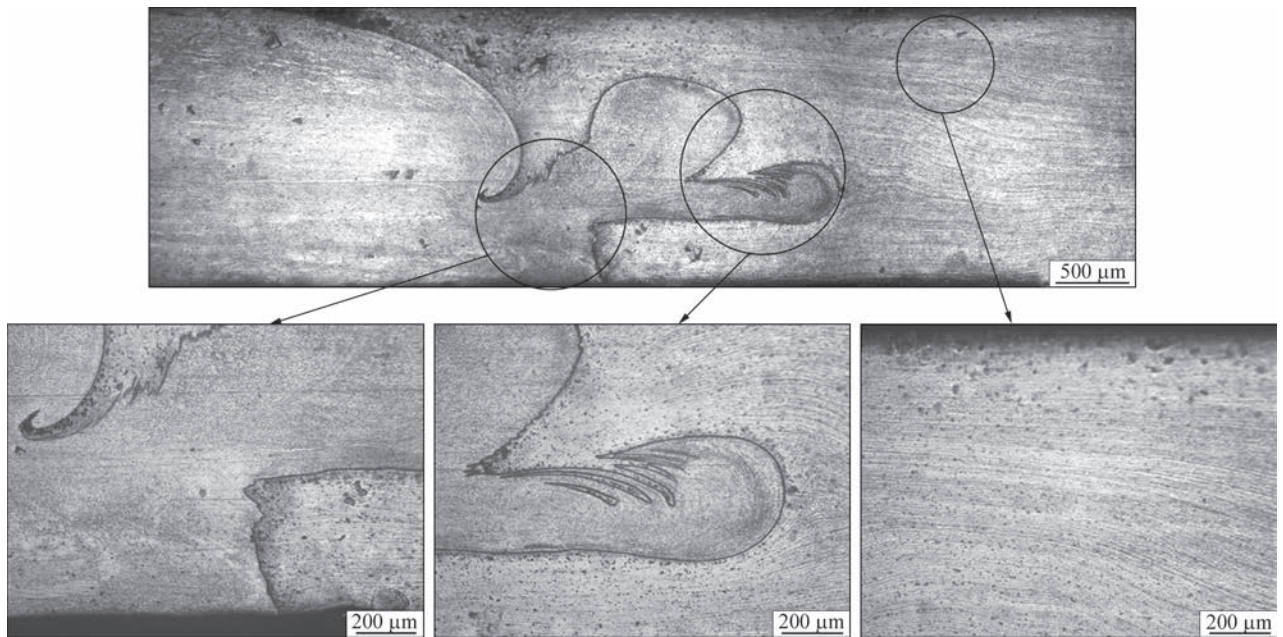
Figure 8. Microstructure of a 2 mm dissimilar welded joint produced at FSW of 1460 aluminium alloy (left) to granulated 1995 aluminium alloy (right)

of a practically globular shape form in the weld nugget, the size of which does not exceed 4–6 μm. In the zone of thermomechanical impact along the boundaries of the weld to base metal transition a more coarse-grained structure (6–8 μm) is observed, compared to the weld nugget, and most of the grains are elongated in the direction of the tool rotation. Here, a more abrupt change of the direction of grain orientation is found from the advancing side, where the directions of rotation and linear displacement of the tool coincide, than from the opposite retreating side. In HAZ the base material structure is preserved, and no surface melting of the structural components takes place (Figure 7). In granulated alloy welding the oversaturated solid solution is preserved in the granules, just their mechanical refinement takes place, resulting in the weld nugget having a finely dispersed dense structure of the weld, and in the zone of weld to base material transition just the direction of the rolling stock texture changes under the impact of the rotational and translation movement of the welding tool.

At FSW of aluminium alloys in a dissimilar combination the welded joint structure changes. Complete mixing of the materials being joined is observed only in the weld upper part, which is equal to 20–25 % of their thickness. In the weld center and lower part individual regions of completely unmixed volumes of the alloys being welded are readily visible. These regions formed as a result of plastic deformation of the metal and its mass transfer by the working surfaces of the tool tip and shoulder. Here, the grain dimensions in the weld central part are approximately the same, as at FSW of the studied alloys in a similar combination,

which is indicative of an intensive plastic deformation of the metal. In TMIZ of dissimilar welded joints, slight differences from similar joints are observed, which are also partly caused by the presence of completely unmixed metal volumes, and partly — by a change in the conditions of weld formation, as a result of different ductility of the alloys being welded. The base metal structure in the HAZ does not change (Figure 8).

CONCLUSIONS

1. Weld formation in the solid state welds at FSW allows producing sound permanent joints of aluminium alloys of different alloying systems, both in the similar and dissimilar combinations. This is true not only for aluminium alloys produced by the standard casting technology, but also for granulated alloys, containing an oversaturated solid solution of refractory transition metals, manufactured using powder metallurgy.

2. Degree of metal softening in the welds depends on the chemical composition of aluminium alloys and their heat hardening ability. The minimal difference between base metal and weld metal hardness is observed at FSW of granulated aluminium alloy 1995 ($HRB \leq 1.5$) and high-strength aluminium alloy 1963 ($HRB \leq 3.5$), prone to hardening in the air. In welding common heat-hardened aluminium alloys 6013 and 1419 weld metal hardness is much ($HRB > 9$) lower than that of the base metal. In joints produced at a dissimilar combination of aluminium alloys, an abrupt or smooth change of hardness at transition from one alloy to another one is observed in the weld metal, depending on the degree of softening of the alloys being welded.

3. Strength of welded joints, produced at FSW of aluminium alloys both in similar and dissimilar combinations, depends on chemical compositions and mechanical properties of these alloys. The maximum ultimate strength is found in welded joints of high-strength 1995 (483 MPa), 1963 (473 MPa), and D16 (441 MPa) alloys that is due to a slight degree of metal softening in TMIZ, which is where the samples fail at static tension. Destruction of samples of welded joints of dissimilar aluminium alloys runs in TMIZ or on the boundary of TMIZ and HAZ from the side of the lower strength alloy. Their ultimate strength is on the level of joints of the respective similar alloys.

4. AT FSW of aluminium alloys both in similar and dissimilar combinations, grains of a practically globular shape, the size of which does not exceed 4–6 μm, form in the weld nugget, owing to intensive plastic deformation of the metal in the permanent joint zone. In welding granulated alloys, the oversaturated solid solution is preserved in the granules, and just their mechanical refinement takes place. As a result, the weld nugget has a finely dispersed dense structure, and the refractory alloying elements do not precipitate from the solid solution in the form of aluminides, which can significantly lower the properties of welded joints of such alloys.

REFERENCES

1. Ishchenko, A.Ya., Labur, T.M. (2013) *Welding of modern structures from aluminium alloys.* Kyiv, Naukova Dumka [in Russian].
2. Ishchenko, A.Ya., Labur, T.M., Bernadsky, V.M., Makovetskaya, O.K. (2006) *Aluminium and its alloys in modern welded structures.* Kyiv, Ekotekhnologiya [in Russian].
3. Beletsky, V.M., Krivov, G.A. (2005) *Aluminium alloys (Composition, properties, technology, application)*: Refer. Book. Ed. by I.N. Fridlyander. Kyiv, KOMINTEKh.
4. Ryabov, V.R., Pavlenko, Yu.V. (1991) Welding of composite materials (Review). *The Paton Welding J.*, **3**, 46–56.
5. Ishchenko, A.Ya., Kharchenko, G.K., Falchenko, Yu.V. et al. (2006) Vacuum solid phase joint of dispersion-hardened composite materials. *Nanosistemy, Nanomaterialy, Nanotekhnologii*, **3**, 747–756 [in Russian].
6. Yasuhiro, Uetani, Ryotaro, Nagata, Hidetoshi, Takadi et al. (2007) Effect of granule size in semi-solid slurry on rheo-extrusion of A7075 aluminum alloy. *Mat. Sci. Forum*, **561–565**, 291–294. DOI: https://doi.org/10.4028/www.scientific.net/MSF.561-565.291
7. Guojiang, Dong, Changcai, Zhao, Yaxin, Peng, Ying, Li (2015) Hot granules medium pressure forming process of AA7075 conical parts. *Chinese J. of Mechanical Eng.*, **28**, 580–591. DOI: https://doi.org/10.3901/CJME.2015.0217.019
8. Inoue, A., Kimura, H. (2000) High-strength aluminium alloys containing nano-quasicrystalline particles. *Mater. Sci. and Eng.* **1**, 1–10.
9. Milman, Yu.V., Sirko, A.I., Yefimov, M.O. et al. (2006) High-strength alloys reinforced by nanosize quasi-crystalline particles for elevated temperature application. *High-Temperature Materials and Processes*, **1–2**, 19–29.
10. Poklyatsky, A.G., Ishchenko, A.Ya., Fedorchuk, V.E. (2011) Friction stir welding of composite, granulated and quasicrystalline aluminium alloys. *The Paton Welding J.*, **7**, 2–7.
11. Milman, Yu.V., Zakharova, N.P., Yefimov, M.O. et al. (2019) Structure and mechanical properties of welded joints of Al–Cr–Fe–Ti system with quasi-crystalline phase. *Elektronnaya Mikroskopiya i Prochnost Materialov*, **25**, 17–26 [in Russian].
12. Ishchenko, A.Ya., Poklyatsky, A.G. (2010) *Tool for friction stir welding of aluminium alloys*. Pat. 54096, Ukraine, Int. Cl. B23K 20/12; Fill. 30.04.2010, Publ. 25.10.2010 [in Ukrainian].

ORCID
A.G. Poklyatskyi: 0000-0002-4101-2206,
S.I. Motrunich: 0000-0002-8841-8609,
V.Ye. Fedorchuk: 0000-0002-9929-3231,
Iu.V. Falchenko: 0000-0002-3028-2964,
M. Sagul: 0000-0001-5091-6381

CONFLICT OF INTEREST
The Authors declare no conflict of interest

CORRESPONDING AUTHOR
S.I. Motrunich
E.O. Paton Electric Welding Institute of the NASU
11 Kazymyr Malevych Str., 03150, Kyiv, Ukraine.
E-mail: paton.testlab@gmail.com

SUGGESTED CITATION
A.G. Poklyatskyi, S.I. Motrunich, V.Ye. Fedorchuk, Iu.V. Falchenko, M. Sagul (2023) Mechanical properties and structural features of butt joints produced at FSW of aluminium alloys of different alloying systems. *The Paton Welding J.*, **4**, 3–10.

JOURNAL HOME PAGE
https://patonpublishinghouse.com/eng/journals/tpwj

MATERIALS AND TECHNOLOGICAL APPROACHES TO WELDING OF COMBINED JOINTS BETWEEN MARTENSITIC AND AUSTENITIC STEELS USED IN POWER MACHINE BUILDING (REVIEW)

M.O. Nimko, V.Yu. Skulskyi, T.V. Ivanenko

E.O. Paton Electric Welding Institute of the NASU
11 Kazymyr Malevych Str., 03150, Kyiv, Ukraine

ABSTRACT

A review of recent foreign research literature is given, dedicated to the choice of welding materials and relevant approaches to welding of combined joints between martensitic and austenitic steels, which are widely used at the moment in the global and domestic power machine building. The typical representatives of martensitic and austenitic steels are considered; the problems arising in the joints of dissimilar steels during high-temperature operation, in particular, the process of carbon diffusion from a less alloyed steel to a more alloyed one and arising of thermal stresses due to the difference in the coefficients of thermal expansion of the combined steels are mentioned; technological approaches to reduce the negative impact of the abovementioned factors are described, as well as the promising welding materials used in the manufacture of such joints and their comparative analysis are given. At the end of the review, a table is given in which literary references are classified depending on the grade of combined steels and welding materials used in the manufacture of welded joints in relevant literary references.

KEYWORDS: welding materials, joints of dissimilar steels, martensitic steels, austenitic steels, nickel alloys, carbon diffusion, decarbonized interlayer

INTRODUCTION

The main thermodynamic cycle of thermal power plants used in modern heat power engineering is the Rankine cycle with steam overheating. To implement this heat cycle, different sections of a water-steam circuit at a power plant should have different parameters of temperature and pressure of the working body. In order to make the construction of a power plant cheaper, the sections with lower steam parameters are manufactured of low-alloy bainitic steels with 0.50–2.25 % Cr (tubes of boiler walls, operate at a temperature of 550–580 °C) and martensitic steels with 9–12 % Cr (upper sections of boiler wall tubes, collectors, main steam lines, for temperatures of up to 625–630 °C), sections with higher steam parameters that require enhanced fatigue strength and scale resistance — from more valuable austenitic steels (superheater coils, operating temperatures are up to 660–680 °C) [1]. To manufacture a closed water-steam circuit, these sections are joined between each other by welding, forming a joint of dissimilar steels. For example, in thermal power plants operating at ultra-supercritical steam parameters and maximum temperatures of 600 °C, 4674 joints may be used only between martensitic and austenitic steels [2].

The appearance of new steels, predetermined by the need of increasing the steam parameters to supercritical and ultra-supercritical levels and the corresponding increase in efficiency of power plants,

required new studies of the features of welding of combinations of these steels with steels operating on other temperature modes.

The aim of the work was a description of the state-of-the-art of developing problems typical for producing joints between modern martensitic and austenitic steels, as well as analysis of welding materials, in particular, nickel-based materials used in recent decades in research works on creating approaches to welding of dissimilar steels.

BASIC STEEL GRADES FOR TUBE SYSTEMS OF OVERHEATED STEAM

This section considers alloying of the main types of martensitic and austenetic steels, welding of whose combination represents a relevant problem for modern thermal power engineering.

To the class of modern martensitic steels, most common in power machine building, steels of the system with a base alloying 9Cr–1Mo: P91 (X10CrMoVNb9-1 according to EN), T92 (X10CrWMoVNb9-2) belong (Table 1).

P91 steel was developed at the National Laboratory in Oak Ridge in the late 1970s and is a modified version of P9 steel (9Cr–1Mo) with controlled additions of vanadium, niobium and nitrogen to improve the high-temperature mechanical properties of steel due to dispersion strengthening by precipitation of carbonitrides MX (where M is vanadium or niobium, and X is carbon or nitrogen). Typical operation temperatures

Table 1. Nominal chemical composition of the most widespread modern martensitic steels [1]

Steel grade	Mass fraction, %									
	C	Si	Mn	Cr	Mo	W	V	Nb	N	B
P91	0.10	0.35	0.45	9.0	0.95	–	0.22	0.08	0.05	–
P/T92	0.09	0.25	0.50	9.0	0.50	1.8	0.20	0.05	0.05	0.003

of this steel in high pressure vessels and tube systems of thermal power plants amount to 580–600 °C [1].

P92/T92 steel is the next modification of P91 steel. The new steel was developed in the "Nippon Steel Corporation" in the 1990s for operation at temperatures of 600 °C and higher and the steam pressure of about 25 MPa. The further improvement in creep resistance in this steel was achieved by the addition of tungsten, which was partially replaced by molybdenum and boron. The initial purpose of adding W and B was an increase in the fraction of solid solution-strengthening and limitation of coarsening of dispersion precipitates [1].

With regard to austenitic steels, it was found that steels of 08Kh18N10 type (S304H, 316L, etc.), originally developed for using in the corrosive environment, also have excellent high-temperature properties. Austenitic stainless steels used in the power machine building and mentioned in this review, are given in Table 2.

Steels operating in corrosion environment have a low carbon content, usually below 0.03 %, which helps to prevent the formation of intercrystalline corrosion. Such steels are designated by the letter L at the end of the name. High-temperature variants of these steels (with the designation H at the end of the name) have a carbon content of about 0.08 %, which contributes to a slight enhancement in the creep resistance.

To provide a sufficient resistance to corrosion and oxidation at temperatures of ~700 °C, it is necessary to increase the content of chromium in steels to 20–25 %. Two classic high-temperature steels in this range of chromium content are 310 and Alloy 800H. However, both have very low creep resistance at 700 °C, although steel 310 is also used at higher temperatures because of its excellent corrosion resis-

tance. To improve the creep resistance, steel HR3C was additionally developed [1].

Additions of Ti and Nb in austenitic steels help to prevent the development of intercrystalline corrosion and additions of Mo improve the pitting corrosion resistance and provide a slight increment to the creep resistance. Nitrogen helps to increase the strength at elevated temperatures by two mechanisms: due to a solid solution strengthening and through the formation of fine-dispersion niobium nitrides.

PROBLEMS ARISING DURING OPERATION OF DISSIMILAR JOINTS

Welded joints of dissimilar steels are characterized in certain areas by a very sharp gradient in the microstructure, physical properties, chemical potential and, as a consequence, in mechanical properties. The main factors responsible for failures during the creep of joints of dissimilar heat-resistant steels are:

- difference in physical properties;
- decarbonization/carbonization in the area of contact of steels due to the difference in the chemical composition of steels and, accordingly, their chemical potential.

Additional stresses in the joints of dissimilar steels can arise because of mismatch of physical properties: for example, austenitic steels have a coefficient of thermal expansion (CTE) by 30 % greater than the martensitic — typical CTE values are 18 and 13–14 μm/m·K, respectively [3]. A cyclic temperature effect on the operation of power plants plays an important role in premature failure of these joints. The difference in the coefficients of thermal expansion and thermal conductivity between the base metal and the weld metal lead to the formation of thermal stresses in a welded joint during numerous launches and

Table 2. Nominal chemical composition of austenitic steels [1]

Steel grade	Mass fraction, %									
	C	Si	Mn	Cr	Ni	Mo	N	Nb	Ti	Other
S304H	0.10	0.2	0.8	18.0	9.0	–	0.1	0.4	–	3.0 Cu
316L	0.03	0.6	1.6	16.0	12.0	2.5	–	–	–	–
347H	0.08	0.6	1.6	18.0	10.0	–	–	0.8	–	–
310	0.08	0.6	1.6	25.0	20.0	–	–	–	–	–
HR3C	0.08	0.4	1.6	25.0	20.0	–	0.2	0.45	–	–
Alloy 800H	0.08	0.5	1.2	21.0	32.0	–	–	–	0.5	0.4 Al
Tempaloy AA-1	0.10	0.3	1.5	18.0	10.0	–	–	0.3	0.2	0.02 B 3.0 Cu

shutdowns of power plants during operation. These cyclic stresses imposed on residual welding stresses and stresses from external load/internal steam pressure can cause critical failure of such joints in the conditions of fatigue and creep. Typically, such failures occur in the HAZ of martensitic steel directly near the fusion line as a result of the propagation of circumferential cracks [4].

A more significant mechanism that affects the time and place of failure in the joints of dissimilar steels, which are exposed to the creep effect, is a structural heterogeneity caused by residual stresses and a gradient of the chemical composition of steels. A difference in chemical potentials between martensitic and austenitic steels leads to migration (diffusion) of carbon across the fusion line of steel with a lower chromium content in steel with a higher chromium content [3]. As a result, after a while, at a high-temperature exposure in steel with a lower content of chromium (usually martensitic steel), near the fusion line a decarbonized interlayer begins to form and propagate, which has reduced hardness and strength, and can serve as a place of specimen failure in the future. Also it was noted that:

● carbon migration significantly reduces the nanohardness and the yield strength of a decarbonized interlayer, which becomes the weakest area in the whole joint [5];

● when the operation temperature grows, the probability of failure on a decarbonized interlayer during a high-cyclic fatigue increases [6];

● a decarbonized interlayer significantly reduces the fatigue resistance of joints during creep at high loads, however, when the test loads are reduced, this effect becomes less noticeable [7].

The abovementioned mechanisms impose restrictions on the use of dissimilar steels of austenitic materials for welding, which, in addition to thermal stresses due to a sharper CTE gradient and carbon diffusion on the side of the martensitic steel to the austenitic weld, can also lead to the formation of a decarbonized interlayer in the fusion zone. In [8], it was shown that microcracks may originate in such a decarbonized interlayer. Such microdefects are mainly originated in the transition zone and have an intergranular nature. It is noted [9] that during failure in a decarbonized interlayer, the interaction of adjacent carbonized and decarbonized areas is critical, that have extreme physical and chemical heterogeneity in the narrow area: in the carbonized zone, microcracks originate and further propagate to the decarbonzied zone, where increased stresses are located.

To overcome the mentioned problem, it was proposed to use nickel-based welding materials, which both in laboratory studies as well as during operation showed a significant improvement in the service life of the joints compared to the joints, welded by chromium-nickel austenitic materials [4]. This is clear, as far as nickel-based weld metal has an intermediate CTE between martensitic and austenitic steels, which respectively leads to a decrease in the value of cyclic thermal stresses in welded joints. Additionally, the use of nickel materials significantly reduces the degree of carbon migration from martensitic steel into the weld metal due to a low gradient of carbon activity, as well as a low carbon diffusion coefficient in nickel alloys.

Therefore, at present time, nickel-based materials are preferred in the manufacture of welded joints between martensitic and austenitic steels. There is a point of view that the use of nickel materials can five times increase the service life of welded joints compared to the joints that use austenitic iron-based materials [4].

The main disadvantage of nickel-based materials is their worse weldability compared to austenitic materials, which requires the advanced qualification of welders. Also, in the literature information can be found describing a tendency of nickel-based metal to the formation of hot cracks in the joints of dissimilar alloys, but most of the information refers to dissimilar joints between nickel alloys and austenitic steels [10, 11].

TECHNOLOGICAL APPROACHES TO WELDING OF DISSIMILAR STEELS

In addition to the traditional performance of the multipass welded joint, the approach with the preliminary cladding of martensitic steel by nickel welding material, subsequent heat treatment of the cladding edge on the mode of tempering of martensitic steel and, then, final welding with the austenitic side of the joint [2, 12–14] (Figure 1).
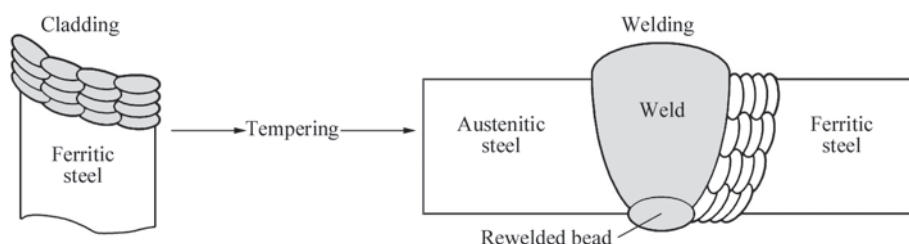

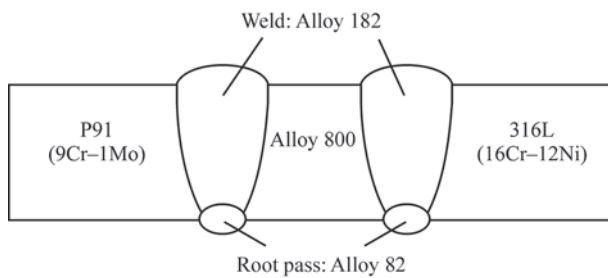**Figure 1.** Scheme of producing welded joint with preliminary cladding

Figure 2. Scheme of joining martensitic and austenitic steel through the insert of the material Alloy 800 [13, 17, 18]

The further technological approaches, aimed at reducing the effect of difference in thermophysical properties between martensitic and austenitic steels, are based on the use of inserts with intermediate CTE. The use of an intermediate insert of Alloy 800 (high-nickel INCOLOY) was proposed, and it is shown that the use of such inserts can lead to a significant decrease in cyclic thermal stresses [4]. Alloy 800 was selected based on the fact that it has an intermediate coefficient of thermal expansion between martensitic and austenitic steels, as well as acceptable creep resistance and oxidation resistance. It is assumed that the use of trimetallic joint with an insert of Alloy 800 can four times increase the duration of service life of welded joint of dissimilar steels compared to conventional bimetallic joint [4].

In the series of works [10, 15–18], Sireesha et al. studied the microstructure and mechanical properties of welded joints P91 + Alloy 800 and Alloy 800 + + 316L as a part of trimetallic joint of P91/Alloy 800/316L: based on the tests on hot cracks formation and results of mechanical and metallographic tests, the comparison of welding materials was carried out. Based on the results of these works, the autors proposed to use the materials Inconel 82 to produce root passes and Inconel 182 — for filling (Figure 2). On the joints produced by the recommended welding materials, the effect of high-temperature aging at 625 °C on the microstructure and mechanical properties and crack formation in thermal cycling in the range of 20–650 °C preriliminary heat treated by the recommended welding materials were studied. The results of this study showed that even in the most unfavorable conditions of thermocyclic testing there is no formation of cracks or oxide undercuts.
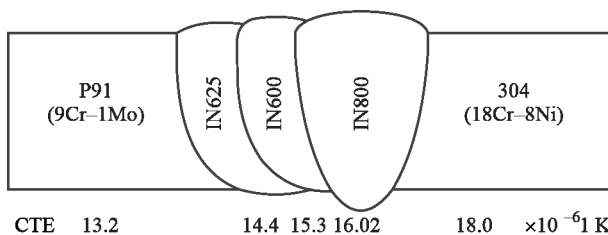

Figure 3. Scheme of producing transition three-metallic weld with a gradient CTE [21, 22]

But in the later work of Lakh et al. [19], the limited prospect of using similar joints with an insert of Alloy 800 is shown. As a result of testing the joints from ferritic-martensitic steels (P9, P91, 2.25Cr–1Mo) with Alloy 800 at 550 °C on creeping, the authors found that the creep resistance of such joints is lower than the creep resistance of the corresponding ferritic steels. It was determined that with a decrease in the load during the creep tests, the place of failure is shifted from the base metal of ferritic steel into the area of intercritical temperatures of HAZ of ferritic steel, which leads to the formation of cracks of type IV. At the lowest loads, the failure occurs in the fusion zone between the ferritic steel and the weld metal and is associated with very low ductility during creeping in this area.

A new approach to welding joints of dissimilar steels was proposed, which was based on the use of transition joints with a filler metal from several steels or alloys [20]. It was assumed that filler materials should have the value of CTE in the range between martensitic and austenitic steels and should be arranged during the weld formation at an increase of CTE from martensitic steel to austenitic.

This approach was partially tested in two works [21, 22], in which two joints of P91 steel with 304 steel were produced by friction stir welding: the first used three-layer transition weld Inconel 625/Inconel 600/Inconel 800 (Figure 3), in the second — a single-layer weld made by the material Inconel 600. Three materials in the first joint were selected based on their value of CTE (Inconel 625 — $14.40 \cdot 10^{-6}$ K^{-1}; Inconel 600 — $15.30 \cdot 10^{-6}$ K^{-1}; Inconel 800 — $16.02 \cdot 10^{-6}$ K^{-1}), that provided a gradient variation of CTE in the joint between P91 steel ($13.18 \cdot 10^{-6}$ K^{-1}) and 304 steel ($18.0 \cdot 10^{-6}$ K^{-1}). The results of the calculations (finite element method) and the creep tests showed that three-metallic joint has better mechanical properties and creep resistance than a simple joint due to a lower stress distribution in the joint. The disadvantage of the three-metallic joint was the presence of a soft interlayer in HAZ of P91 steel, the formation of which could be associated with carbon diffusion in the adjacent alloy Inconel 625 (the alloy contains 22 % of Cr).

In this connection, the promising research area is the development of heat-resistant welding material based on nickel or iron-nickel, which could have the lowered content of chromium (~ 9% Cr) for prevention of carbon diffusion and CTE close to martensitic steels (~ $14 \cdot 10^{-6}$ K^{-1}). One of the first steps in this direction was the study of Electric Power Research Institute (EPRI) and the development of welding material HFS6 associated with them developed in the 1980s. HFS6 has never reached a commercial use due
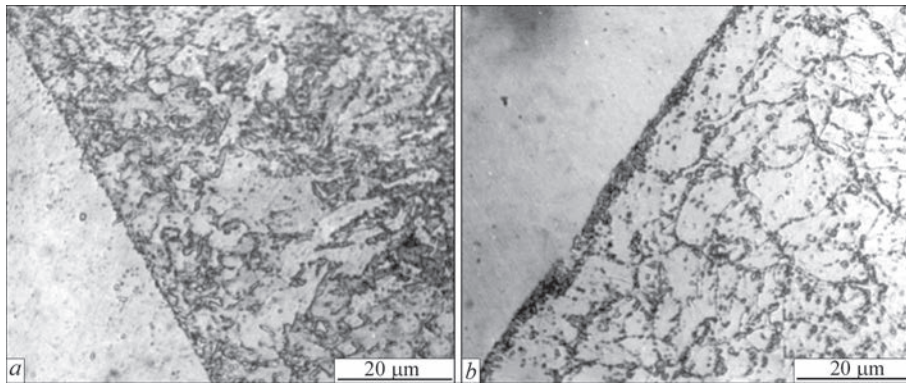
Figure 4. Microstructure of HAZ of P91 steel together with the fusion zone (weld Inconel 182) before and after thermal cycling: *a* — tempering at 760 °C, 50 h; *b* — tempering at 760 °C, 50 h + thermocycling 20–625 °C [16]

to the succeptibility to the liquation cracking in the weld metal, but the data obtained in the research program on its development were of great importance in the future [23]. In 2002, the development of electrodes EPRI P87 was initiated and already in 2009 it was reported about their successful commercial use in the construction of thermal coal power plant in the USA. On the basis of chemical composition of electrodes, a solid wire was later developed for using in TIG welding. A characteristic feature of this nickel-based material is the content of chromium and carbon, close to the content of these elements in P91 steel, which should facilitate the elimination of carbon migration (and formation of carbides of type I) across the fusion zone between the weld, made by P87 and martensitic steel. In addition, P87 has an acceptable CTE value similar to CTE of other nickel-based materials [24].

A broader overview of the types of transition welds, which can be found in the joints of ferritic and austenitic steels in power machine building is given in [4].

CARBON DIFFUSION WHEN USING NICKEL-BASED MATERIALS

Most researchers assume that traditional nickel-based materials (Alloy 82/182/617/625 etc.) can not effectively restrain carbon diffusion from martensitic steel to a weld, since most nickel alloys used as welded

materials contain a large number of carbide-forming agents (Cr, Mo, Nb, Ti).

Regarding the joints between martensitic and austenitic steels, in [16] it was shown, that in the joint P91 + Alloy 800, produced by the electrodes Inconel 182, after a long tempering for 20 and 50 h at a temperature of 760 °C and a subsequent thermocycling in the range of 20–625 °C/3025 h at the boundary between P91 steel and nickel weld, carbon migration and formation of a dark-etched area with an increased hardness occur (Figure 4).

In [12], already after tempering at 760 °C/2 h, the formation of a carbonized interlayer in cladding by Inconel 182 and the formation of a soft area in HAZ of P91 steel (Figure 5) was observed. Analysis of the results of mechanical tensile tests of the miniature specimens from different areas of the cladded joint P91 + 316L showed that HAZ of P91 steel had the lowest values of long-term strength and resistance to ductile instability both at a room temperature and at a temperature of 550 °C.

Some of the works give controversial data on the effectiveness of traditional nickel alloys in counteracting carbon migration, possibly predetermined by the lack of a single approach to the evaluation of a decarbonized HAZ area of a low-carbon steel in the combined welded joints.
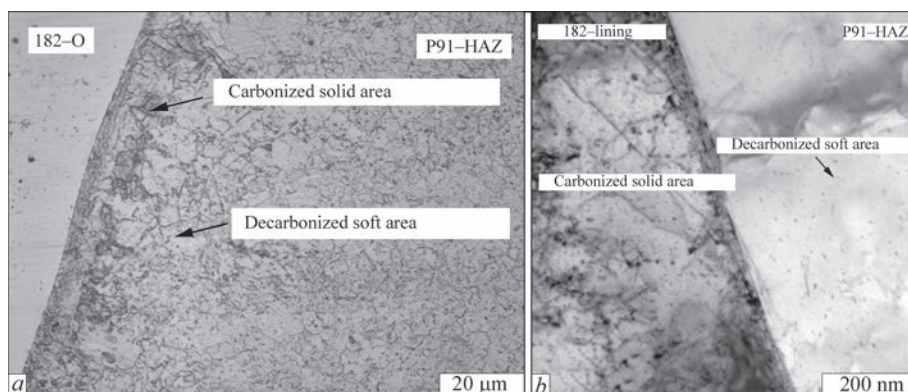

Figure 5. Microstructure of the fusion zone of P91/Inconel 182 after tempering at 760 °C, 2 h: *a* — optical microimage (etched side of P91); *b* — TEM image [12]

15
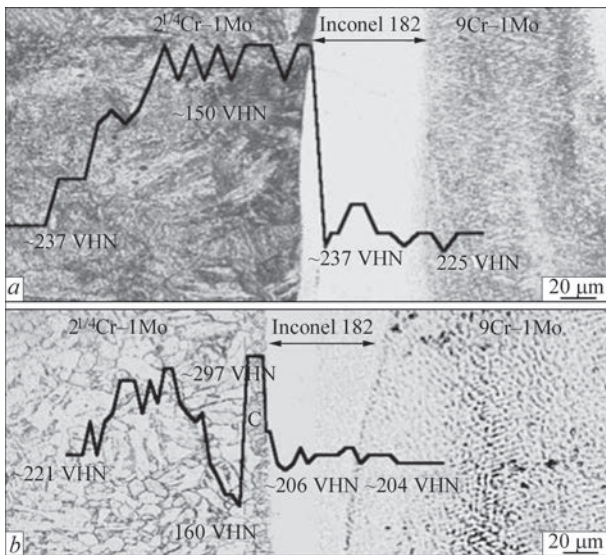
Figure 6. Microstructure and hardness profile in the transition joint, made with a cladding layer of Inconel 182 of 0.1 mm thickness after heat treatment at 750 °C with the duration: *a* — 1 h; *b* — 15 h [25]

For example, in the work of Anand et al. [25] by using of the calculation methods, carbon diffusion was studied in surfacing "substrate of 2.25Cr–1Mo/ intermediate interlayer of Inconel 182 (0.1 mm)/layer of 9Cr–1Mo (2 mm)" at a temperature of 750 °C and an exposure of up to 15 h.

The results of the calculation in the triple Fe–Cr–C system on the basis of the finite difference method showed that the efficiency of lining with a nickel material depends on its thickness: in the joints, the lining thickness of which was 40 μm, the formation of

strengthened carbonized areas near the fusion zone and their absence in the joints with the lining of 80 μm thickness and higher was predicted, i.e., with an increase in lining thickness, its effectiveness in the removal of carbon migration grows. These results were confirmed experimentally by metallography and measuring hardness of deposits, tempered at 750 °C for 1 and 15 h, which showed the absence of formation of solid areas in a nickel weld or steel 9Cr–1Mo (Figure 6).

Regarding the new material EPRI P87, in [26] its high efficiency in restraining carbon migration from martensitic steel T92 was shown, which significantly exceeds that compared to traditional nickel alloys. It is shown that in the joints made by Inconel 82 after tempering at 760 °C, 30 min, a decarbonized area in some places was 18 times wider, and in the case of Inconel 617 — by 24 times wider than in the joints of EPRI P87 (Figure 7). In [27] on the plate of P91 steel, three deposits were performed: by the material EPRI P87 (9 % Cr), by austenitic stainless 309 steel (22–25 % Cr) and by Inconel 625 (20–23 % Cr). After surfacing, the plate was normalized at a temperature of 1060 °C, 2 h and tempered at a temperature of 760 °C, 2 h. The results of metallographic examinations shown in Figure 8, confirm the benefits of a new material in restraining decarbonization.

SELECTION OF MATERIALS FOR WELDING TYPICAL JOINTS

Analysis of literature data shows that recently for welding of typical combined joints in the power machine

Figure 7. Transition zone between T92 steel and weld, made by the material EPRI P87 (*a*), Inconel 82 (*b*) and Inconel 617 (*c*) after tempering at 760 °C, 30 min [26]

Figure 8. Transition zone between P91 steel and weld, made by the material ER 309 (*a*), Inconel 625 (*b*) and EPRI P87 (*c*) after normalization at 1060 °C, 2 h and tempering at 760 °C, 2 h [27]

building, the materials most commonly used in research works are Alloy 82 and Alloy 182 (Table 3). The typical chemical composition of the most common nickel-based welding materials is given in Table 4.
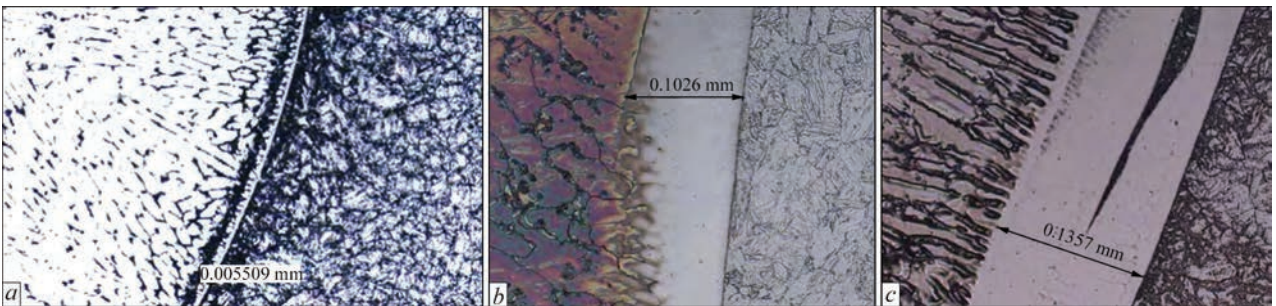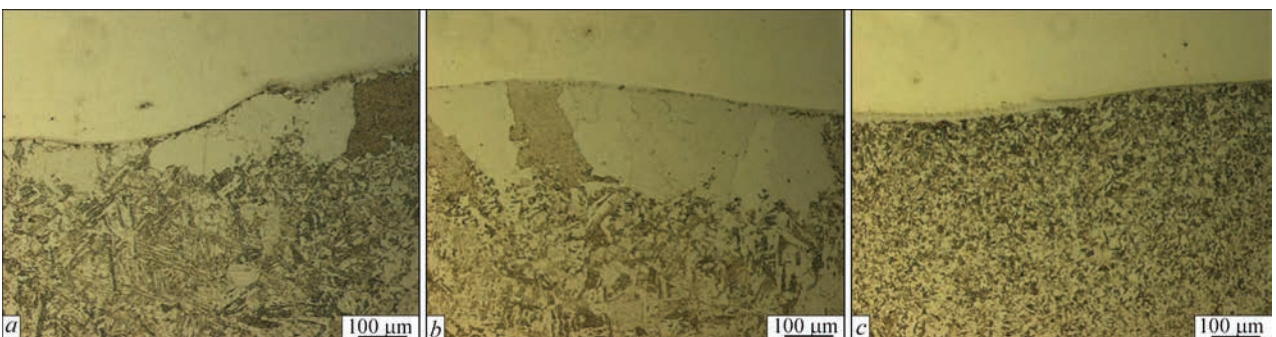
Some works provide comparative studies of microstructure and mechanical properties of various welding materials regarding a specific combination of welded steels. Thus, in [33], the comparisons of welding materials T-304H, Alloy 617 and Alloy 82 were made based on the criteria of tests on impact toughness and static bending of the joints T92 + 304 (postweld tempering at 630–670 °C, 2 h). It is shown that in the produced compositions of welded joints,

the welds produced by the electeodes T-304H had the lowest impact toughness. When comparing the materials Alloy 617 and Alloy 82, the first was preferred, since the welds in the welded joints produced by Alloy 617 had a higher value of ultimate strength than the welds produced by Alloy 82.

Comparative studies of properties of the joints of steels T92 + 304, made using welding materials Alloy 625 and Alloy 82, showed that welded joints with the welds of Alloy 625 had the best microstructural and mechanical properties [35].

Huysmans et al. [2] performed aging at 625 °C, 10000 h of joints T92 + 304, produced by the weld-

Table 3. Typical combined joints found in recent research literature and materials used for their welding

Martensitic steel	Austenitic steel	Welding materials	Literary sources
P91	S304H	Alloy 625, Alloy 600	21, 22, 28
		EPRI P87	23
	S304L	Alloy 182	14
		AWSER90S-B9 (9CrMoV–N)	29
	316L	Alloy 182	10, 12, 13, 15, 16, 17, 18, 19
		Alloy82	10, 15
	310HCbN	EPRI P87	23
	347H	Alloy 82	30, 31, 32
		Rutox (19Cr–20Ni)	30
		ER90S-B3	32
		EPRI P87	23
T92	S304H	Alloy 82	33, 34, 35, 36, 37
		Alloy 617	2, 33, 38
		T-304H	33
		Alloy 625	35
		EPRI P87	2, 23
	316H	Alloy 82	39, 40, 41, 42
	Tempaloy AA-1	EPRI P87	26
		Alloy 82	
		Alloy 617	
	310	Alloy 82	2
		EPRI P87	23
	347HFG	EPRI P87	23
	HR3C	Alloy 82	43
		EPRI P87	2

Table 4. Chemical composition of typical nickel-based welding materials

Alloy	Mass fraction, %									
	C	Si	Mn	Cr	Ni	Mo	Nb	Ti	Fe	Other
Alloy 82	≤ 0.1	≤ 0.5	2.5–3.5	18.0–22.0	≥ 67.0*	–	2.0–3.0**	≤ 0.75	≤ 3.0	Cu ≤ 0.5
Alloy 182	≤ 0.1	≤ 1.0	5.0–9.5	13.0–17.0	≥ 59.0*	–	1.0–2.5**	≤ 1.0	≤ 10.0	Cu ≤ 0.5
Alloy 600	≤ 0.15	≤ 0.5	≤ 1.0	14.0–17.0	≥ 72.0*	–	–	–	6.0–10.0	Cu ≤ 0.5
Alloy 617	0.05–0.15	≤ 1.0	≤ 1.0	20.0–24.0	≥ 44.5	8.0–10.0	–	≤ 0.6	≤ 3.0	Co 10.0–15.0 Al 0.8–1.5 Cu ≤ 0.5 B ≤ 0.006
Alloy 625	≤ 0.1	≤ 0.5	≤ 0.5	20.0–23.0	≥ 58.0	8.0–10.0	3.15–4.15**	≤ 0.4	≤ 5.0	Co ≤ 1.0 Al ≤ 0.4
EPRI P87 [24]	≤ 0.1	≤ 0.3	≤ 1.5	≤ 9.0	Balance	≤ 2.0	≤ 1.0	–	≤ 38.0	Negligible additions of Al, Ti, N, B

Note. *The content of Ni + Co is indicated. **The content of Nb + Ta is indicated.

ing wires Alloy 617, Alloy 82 and EPRI P87 (TIG). It was determined that in the joints produced by the wire Alloy 617, when aging in HAZ of T92 steel, carbides of type I precipitate, which can lead to preliminary failures in a high-temperature creep. After the same aging conditions, the material P87 showed itself better than other, and it is stated that preference should be given to the technologies of a preliminary cladding of the edge with tempering before conventional welding. Alloy 82 was recognized by the authors of the study as a good alternative to the material P87. However, it was established that at longer high-temperature exposures in the joints, produced by Alloy 82, near the fusion line of T92 steel, more single-oriented carbides are formed, which can subsequently lead to failure.

According to the results of the mentioned works for the joints T92 + 304, based on the improvement in the quality of joints, the following conditional comparative classification of welding materials can be composed: T-304H < Alloy 617 ≈ Alloy 82 < Alloy 625 < EPRI P87.

The materials Alloy 617, Alloy 82 and EPRI P87 were also studied in [26] in the joints T92 + Tempaloy AA-1. In the tests on static tension and impact toughness, the best results were shown by the material Alloy 82; Alloy 617 and EPRI P87 showed similar lower values, which still exceeded the minimum level recommended by the European standards. During tests of all three joints on bending, the angle of bending was maintained at 180° without the formation of microcracks. The measurements of microhardness in the state after tempering at 760 °C, 30 min showed that the joints produced by the material Alloy 82, the strongest softening occurred in the decarbonized area. It is assumed that namely in this area, in the future the failure will be occurred during high-temperature operation under high pressure.

The comparative evaluation of the materials Alloy 82 and Alloy 182 with respect to the joint of steels P91 + 316 is given in [10, 13]. In general, these materials have similar properties, but researchers give preference to Alloy 182. In particular, it is noted that in the conditions of fatigue thermocycling, the welds of type Alloy 182 showed a lower tendency to failure formation than the welds made by Alloy 82.

In [30] the comparisons of mechanical properties and microstructures of joints P91 + 347 were made, produced by the wire Alloy 82 (TIG), electrodes Rutox-Ast, Rutox-B (MAW) and in a combined method «root Alloy 82 (TIG) + filling Rutox-Ast (MAW)». The best results by mechanical properties (ultimate strength, ductility) were demonstrated by the joint produced by the wire Alloy 82, at the second place —

Rutox-Ast (MAW), further — combined method and Rutox-B (MAW) at the end.

In recent years, the use of autogenous methods of welding of dissimilar joints of martensitic and austenitic steels, in particular, TIG welding using activated fluxes being in a suspended state in a solution of a carrier, such as methanol, ethanol or acetone (A-TIG). Typical joints of martensitic and austenitic steels were investigated in connection with this method of welding: P91 + 316L [44, 45], P92 + 304H [36, 46], P91 + 304L [47].

The researchers, who compared A-TIG process and conventional TIG welding with filler wire, note [36] that welds made with autogenous A-TIG welding have increased values of tensile strength and lowered values of impact toughness compared to conventional welding with the wire. The reason for this is that the structure of autogenous weld consists of untempered martensite, whereas when performing multi-pass welding by the wire, additional tempering of the already produced weld with the help of subsequent beads is performed. Due to this fact, the joints produced with the help of A-TIG process require much longer exposure in the postweld heat treatment than the standard joints to acquire the acceptable mechanical properties.

CONCLUSIONS

1. One of the major problems during welding of martensitic and high-alloy austenitic steels is a diffusion reduction of carbon concentration in less alloy metal, contacting with a more alloyed metal containing energetic carbide-forming elements — primarily, chromium, as well as molybdenum, titanium, niobium. The areas depleted with carbon are the zones of possible failure of joints during operation.

2. The main technological measure aimed at reducing carbon depletion of martensitic steel remains traditional nickel-based seam welding. The most common are electrode materials of type Alloy 82, Alloy 182, Alloy 600, Alloy 617 and Alloy 625.

3. It was established that the use of nickel-based welding materials does not completely restrain the carbon redistribution due to their high chromium content (13–24 %), as well as other carbide-forming elements.

4. Highly-effective in restricting carbon depletion of martensitic steel is a new nickel-based electrode of grade EPRI P87 with 9 % of chromium, developed by the Electric Power Research Institute EPRI, USA. It was experimentally shown that under the same thermal conditions of producing joints, the width of depleted carbon interlayer when using electrode P87 will be 18–24 times lower than in welding with the electrodes Alloy 82 and Alloy 617.

5. The redistribution of carbon between the less alloyed martensitic steel and the more alloyed weld is affected not only by the difference in the chemical potential of carbon in steels, caused by different content of carbide-forming elements, as well as a stressed state caused by different value of coefficients of thermal expansion of contacting metals. To reduce the stress level in the fusion zone, there are welding methods with the minimization of gradient of CTE in the joint, which involve welding using a transition insert or by layering of several electrode materials with an intermediate (between α- and γ-steels) coefficient of thermal expansion.

6. Based on studying the structure and mechanical characteristics of joints of dissimilar steels, the following most acceptable welding materials for subsequent combinations of steels were identified: T92 + SS304 — EPRI P87; P91 + SS316 — Alloy 182; P91 + SS347 — Alloy 82.

On the example of the joint T92 + SS304, it was found that as to the efficiency of impact on metal quality in the joint zone, the welding materials can be positioned as follows: T-304H < Alloy 617 ≈ Alloy 82 < Alloy 625 < EPRI P87.

REFERENCES

1. Shibli, A. (2014) *Coal power plant materials and life assessment.* Woodhead Publ.

2. Huysmans, S., Vekeman, J., Hautfenne, C. (2017) Dissimilar metal welds between 9Cr creep strength enhanced ferritic steel and advanced stainless steels–creep rupture test results and microstructural investigations. *Weld World*, **61**, 341–350.

3. Dak, G., Pandey, C. (2020) A critical review on dissimilar welds joint between martensitic and austenitic steel for power plant application. *J. of Manufacturing Processes*, **58**, 377–406.

4. Bhaduri, A. K., Venkadesan, S., Rodriguez, P., Mukunda, P. G. (1994) Transition metal joints for steam generators-An overview. *Int. J. of Pressure Vessels and Piping*, 58(**3**) 251–265.

5. Wu, Q., Xua, Q., Jianga, Y., Gonga, J. (2020) Effect of carbon migration on mechanical properties of dissimilar weld joint. *Engineering Failure Analysis*, **117**, 104935, 1–10.

6. Zhang, W.-Ch., Zhu, M.-L., Wang, K., Xuan, F.-Zh. (2018) Failure mechanisms and design of dissimilar welds of 9 % Cr and CrMoV steels up to very high cycle fatigue regime. *Int. J. of Fatigue*, **113**, 367–376.

7. Yong, J., Zuo, Zh., Jianming, G. (2015) Carbon diffusion and its effect on high temperature creep life of Cr5Mo/A302 dissimilar welded joint. *Acta Metallurgica Sinica*, 51(**4**), 393–399.

8. Frei, J., Alexandrov, B. T., Rethmeier, M. (2019) Low heat input gas metal arc welding for dissimilar metal weld overlays. Pt III: Hydrogen-assisted cracking susceptibility. *Welding in the World*, **63**, 591–598.

9. Ul-Hamid, A., Tawancy, H.M., Abbas, N.M. (2005) Failure of weld joints between carbon steel pipe and 304 stainless steel elbows. *Eng. Failure Analysis*, **12**, 181–191.

10. Sireesha, M., Albert, S. K., Shankar, V., Sundaresan, S. (2000) A comparative evaluation of welding consumables for dissimilar welds between 316LN austenitic stainless steel and Alloy 800. *J. of Nuclear Materials*, **279**, 65–76.

11. Singh, S., Singh, A.B., Kumar, M. et al. (2021) Dissimilar metal welds used in AUSC power plant, fabrication and structural integrity issues. *IOP Conf. Series: Materials Sci. and Eng.*, **1017**, 012022.

12. Karthick, K., Malarvizhi, S., Balasubramanian, V., Gourav Rao, A. (2018) Tensile properties variation across the dissimilar metal weld joint between modified 9Cr–1Mo ferritic steel and 316LN stainless steel at RT and 550 °C. *Metallography, Microstructure and Analysis*, **7**, 209–221.

13. Lee, H.-Y., Lee, S.-H., Kim, J.-B., Lee, J.-H. (2007) Creep–fatigue damage for a structure with dissimilar metal welds of modified 9Cr–1Mo steel and 316L stainless steel. *Int. J. of Fatigue*, **29**, 1868–1879.

14. Mahajan, S., Chhibber, R. (2020) Investigations on dissimilar welding of P91/SS304L using nickel-based electrodes. *Materials and Manufacturing Processes*, 35(**9**), 1010–1023.

15. Sireesha, M., Shankar, V., Albert, S. K., Sundaresan, S. (2000) Microstructural features of dissimilar welds between 316LN austenitic stainless steel and alloy 800. *Mater. Sci. and Engin.*, **A292**, 74–82.

16. Sireesha, M., Albert, S. K., Sundaresan, S. (2002) Thermal cycling of transition joints between modified 9Cr–1Mo steel and Alloy 800 for steam generator application. *Int. J. of Pressure Vessels and Piping*, **79**, 819–827.

17. Sireesha, M., Albert, S. K., Sundaresan, S. (2003) Metallurgical changes and mechanical behavior during high temperature aging of welds between Alloy 800 and 316LN austenitic stainless steel. *Mater. Sci. and Technol.*, 19(**10**), 1411–1417.

18. Sireesha, M., Albert, S. K., Sundaresan, S. (2005) Influence of high-temperature exposure on the microstructure and mechanical properties of dissimilar metal welds between modified 9Cr–1Mo steel and Alloy 800. *Metallurg. and Mater. Transact. A*, **36A**, 1495–1506.

19. Laha, K., Chandravathi, K.S., Parameswaran, P. et al. (2012) A comparison of creep rupture strength of ferritic/austenitic dissimilar weld joints of different grades of Cr–Mo ferritic steels. *Metallurg. and Mater. Transact. A*, **43A**, 1174–1186.

20. Brentrup, G.J., Snowden, B.S., DuPont, J.N., Grenestedt, J.L. (2012) Design considerations of graded transition joints for welding dissimilar alloys. *Welding J.*, 91, 252–259.

21. Akram, J., Kalvala, P.R., Misra, M., Charit, I. (2017) Creep behavior of dissimilar metal weld joints between P91 and AISI 304. *Mater. Sci. and Engin. A*, **688**, 396–406.

22. Akram, J., Kalvala, P.R., Chalavadi, P., Misra, M. (2018) Dissimilar metal weld joints of P91/Ni alloy: Microstructural characterization of HAZ of P91 and stress analysis at the weld interfaces. *J. Mater. Engin. and Performance*, 27(**8**), 4115–4128.

23. Siefert, J.A., Tanzosh, J.M., Shingledecker, J.P. (2010) Weldability of EPRI P87. In: *Proc. of the 6th Int. Conf. on Advances in Materials Technology for Fossil Power Plants (August 31–September 3, 2010, Santa Fe, New Mexico, USA)*, 995–1013.

24. Siefert, J.A., Tanzosh, J.M., Shingledecker, J.P. et al. (2011) EPRI P87: A promising new filler metal for dissimilar metal welding. *Welding J.*, 90(**3**), 30–34.

25. Anand, R., Sudha, C., Karthikeyan, T. et al. (2009) Effectiveness of Ni-based diffusion barriers in preventing hard zone formation in ferritic steel joints. *J. of Materials Sci.*, **44**, 257–265.

26. Urzynicok, M., Jachym, R., Kwiecinski, K. et al. (2013) Application of EPRI87 in dissimilar welding austenitic-martensitic welded joints of TEMPALOY AA-1 and T92 steel grades. In: *Proc. of 7th Int. Conf. on Advances in Materials Technology for Fossil Power Plants (October 22–25, 2013 Waikoloa, Hawaii, USA)*, 992–1005.

27. Coleman, K., Gandy, D. (2007) Alternative filler materials for DMWs involving P91 materials. In: *Proc. of 5ᵗʰ Int. Conf. on Advances in Materials Technology for Fossil Power Plants (October 3–5, 2007, Marco Island, Florida, USA)*, 940–967.

28. Sirohi, S., Pandey, C., Goyal, A. (2021) Role of the Ni-based filler (IN625) and heat-treatment on the mechanical performance of the GTA welded dissimilar joint of P91 and SS304H steel. *J. of Manufacturing Processes*, **65**, 174–189.

29. Thakare, J.G., Pandey, C., Mahapatra, M.M., Mulik, R.S. (2019) An assessment for mechanical and microstructure behavior of dissimilar material welded joint between nuclear grade martensitic P91 and austenitic SS304 L steel. *J. of Manufacturing Processes*, **48**, 249–259.

30. Mittal, R., Sidhu, B.S. (2015) Microstructures and mechanical properties of dissimilar T91/347H steel weldments. *J. Materials Proc. Technology*, **220**, 76–86.

31. Senthil, T.S., Siva Kumar, G. (2015) Dissimilar steel welding of super heater coils for power boiler applications. *American J. of Materials Research*, 2(**5**), 44–49.

32. Arunkumar, N., Duraisamy, P., Veeramanikandan, S. (2012) Evaluation of mechanical properties of dissimilar metal tube welded joints using inert gas welding. *Int. J. of Eng. Research and Applications*, 2(**5**), 1709–1717.

33. Liang, Z., Gui, Y., Zhao, Q. (2018) Investigation of microstructures and mechanical properties of T92 martensitic steel/Super304 austenitic steel weld joints made with three welding consumables. *Archives of Metallurgy and Materials*, 63(**3**), 1249–1256.

34. Cao, J., Gong, Y., Zhu, K. et al. (2011) Microstructure and mechanical properties of dissimilar materials joints between T92 martensitic and S304H austenitic steels. *Materials and Design*, **32**, 2763–2770.

35. Chen, G., Zhang, Q., Liu, J. et al. (2013) Microstructures and mechanical properties of T92/Super304H dissimilar steel weld joints after high-temperature ageing. *Materials and Design*, **44**, 469–475.

36. Sharma, P., Kumar Dwivedi, D. (2019) Comparative study of activated flux-GTAW and multipass-GTAW dissimilar P92 steel-304H ASS joints. *Materials and Manufacturing Processes*, 34(**11**), 1195–1204.

37. Xu, L., Wang, Y., Jing, H. et al. (2016) Deformation Mechanism and Microstructure Evolution of T92/S30432 Dissimilar Welded Joint During Creep. *J. Mater. Eng. and Performance*, **25**, 3960–3971.

38. Liang, Z., Zhao, Q., Deng, J., Wang, Y. (2017) Influence of aging treatment on the microstructure and mechanical properties of T92/Super 304H dissimilar metal welds. *Materials at High Temperatures*, 35(**2**), 1–8.

39. Čiripová, L., Falat, L., Ševc, P. et al. (2018) Ageing effects on room-temperature tensile properties and fracture behavior of quenched and tempered T92/TP316H dissimilar welded joints with Ni-based weld metal. *Metals*, **8**, 791–806.

40. Falat, L., Výrostková, A., Svoboda, M., Milkovič, O. (2011) The influence of PWHT regime on microstructure and creep rupture behaviour of dissimilar T92/TP316H ferritic/austenitic welded joints with Ni-based filler metal. *Kovove Materialy*, 49(**6**), 417–426.

41. Falat, L., Čiripová, L., Kepič, J. et al. (2014) Correlation between microstructure and creep performance of martensitic/austenitic transition weldment in dependence of its post-weld heat treatment. *Eng. Failure Analysis,* **40**, 141–152.

42. Falat, L., Kepič, J., Čiripová, L. et al. (2016) The effects of postweld heat treatment and isothermal aging on T92 steel heat-affected zone mechanical properties of T92/TP316H dissimilar weldments. *J. of Materials Research*, 31(**10**), 1532–1543.

43. Cao, J., Gong, Y., Yang, Z.G. (2011) Microstructural analysis on creep properties of dissimilar materials joints between T92 martensitic and HR3C austenitic steels. *Mater. Sci. and Engin. A*, **528**, 6103–6111.

44. Fei, Z., Pan, Z., Cuiuri, D. et al. (2020) Effect of post-weld heat treatment on microstructure and mechanical properties of deep penetration autogenous TIG-welded dissimilar joint between creep strength enhanced ferritic steel and austenitic stainless steel. *The Int. J. of Advanced Manufacturing Technology*, **108**, 3207–3229.

45. Vidyarthy, R.S., Kulkarni, A., Dwivedi, D.K. (2017) Study of microstructure and mechanical property relationships of A-TIG welded P91–316L dissimilar steel joint. *Mater. Sci. and Engin. A*, **695**, 249–257.

46. Sharma, P., Kumar Dwivedi, D. (2019) A-TIG welding of dissimilar P92 steel and 304H austenitic stainless steel: Mechanisms, microstructure and mechanical properties. *J. of Manufacturing Processes*, **44**, 166–178.

47. Thakare, J.G., Pandey, C., Gupta, A. et al. (2021) Role of the heterogeneity in microstructure on the mechanical performance of the Autogenous Gas Tungsten Arc (GTA) welded dissimilar joint of F/M P91 and SS304L steel. *Fusion Eng. and Design*, **168**, 112616, 1–13.

ORCID

M.O. Nimko: 0000-0002-9672-4921,
V.Yu. Skulskyi: 0000-0002-4766-5355

CONFLICT OF INTEREST

The Authors declare no conflict of interest

CORRESPONDING AUTHOR

V.Yu. Skulskyi
E.O. Paton Electric Welding Institute of the NASU
11 Kazymyr Malevych Str., 03150, Kyiv, Ukraine.
E-mail: vsku@paton.kiev.ua

SUGGESTED CITATION

JOURNAL HOME PAGE

https://patonpublishinghouse.com/eng/journals/tpwj

NUMERICAL METHOD OF MULTISCALE MODELING OF THE STRESS-STRAIN STATE OF LARGE-SIZED STRUCTURES IN SITE WELDING

O.S. Milenin, O.A. Velykoivanenko, G.P. Rozynka, N.I. Pivtorak

E.O. Paton Electric Welding Institute of the NASU
11 Kazymyr Malevych Str., 03150, Kyiv, Ukraine

ABSTRACT

A multiscale procedure was proposed for modeling the kinetics of stress-strain state of large-sized structures during site welding. This procedure is based on finite element solution of nonstationary thermoplasticity problems, characteristic for fusion welding technologies, at the mesoscale level with fine spatial breakdown of the region and with subsequent transfer of a certain amount of calculation data into a macroscopic model of a large-scale structure. Algorithms of the respective averaging of the properties and stress-strain state parameters are proposed for this purpose, which allows performing analysis of large-sized structures during welding without the need to involve significant computing power. A characteristic example of site welding of a cylindrical structure of a large diameter is used to show the applicability of the developed approach for prediction of spatial distribution of stresses and strains. Here, the most effective method is calculation of the stress fields, where a much greater sparseness of the spatial breakdown can be achieved, while calculation of the strained state is much more sensitive to finite element size.

KEYWORDS: large-sized structures, welding, stress-strain state, mathematical modeling, multiscale method, resource intensity of calculation

INTRODUCTION

Solution of the characteristic problems of optimization of the technological processes of site welding of large-sized structures is related to a number of objective difficulties because of the length of the welds, and, at the same time, local influence of welding heating. In particular, a necessary step is prediction of the current and residual stress-strain state (SSS) of the structures, which is due to the need to guarantee the admissibility of their shape change, local resistance and resistance to different types of fracture [1–3]. Experimental determination of development of the temperature, stress and strain fields in welding, in order to guarantee the proper quality of the end product, is made more complicated by material consumption of the structure and significant associated financial costs, so that application of modern methods of numerical modeling of the welding processes is rational. It allows establishing the qualitative and quantitative regularities of the influence of welding on the state of a specific structure, both at mounting, and in further operation.

Appearance of new methods of prediction of the state of large-sized structures, including those with a large number of welds, corresponds to development of understanding of physical-mechanical processes in continuous media, mathematical models, describing them, numerical methods and computer technologies. Modern principles of discrete description of

the kinetics of nonstationary multiphysical processes (primarily, by finite element methods) provide ample possibilities for solving the fundamental and applied problems. The adequacy and accuracy of the obtained numerical results depends, in particular, on the fineness of spatial breakdown, i.e. size of the finite element (FE), which is sufficient to obtain the exact solution of the necessary differential equations in the difference formulation of the problem [4]. However, as regards numerical description of the state of large-sized structures in welding, it means an excessive resource intensity of the problems, as, on the one hand, the high gradient of temperatures, stresses and strains in the welding area requires fine spatial breakdown, which cannot be used over the entire structure, and on the other hand, the great difference in FE dimensions leads to instability of the schemes of solving the respective boundary problems [5]. This caused development of simplified models, which allow describing with the required accuracy the separate technological and physical-mechanical processes in welding and related processes.

In particular, the methods of inherent strain or shrinkage functions became widely accepted for prediction of residual shape change of large-sized structures as a result of site welding [6, 7]. This class of methods involves the assumption that the residual plastic strains, caused by welding (precalculated or experimentally measured) can be assigned as the initial state of a specific structure, which is particularly

convenient in the case of presence of a large number of similar welds: in ship plating, stringer panels, etc. [8–10]. The disadvantage of the above methods is the fact that they do not allow following the current SSS of the structures during welding, but consider only the problem of the residual strained state. Moreover, in the absence of data on the kinetics of the temperature field and strained state during welding, objective difficulties arise in determination of the effective region for assigning the initial integrated or distributed plastic strains in the weld metal and HAZ. So-called 2D-X models allow modeling of the current state of large-sized structures [11], however, their applicability is quite limited. Therefore, further development of the numerical methods of prediction of the current SSS of large-sized structures during site welding is practically important, in particular, in the case of typical cylindrical pressure vessels, which is the purpose of this work.

As it was said above, one of the features of the state of large-sized structures in welding is the different scale of physical-mechanical processes in the welding area and on the periphery. This complicates the numerical realization of the respective mathematical models by the common methods, but it makes application of multilevel multiscale models rational. So, development of temperatures and SSS is of a local nature in welding, and it can be described by joint models of heat conductivity and elasto-plastic medium. For a range of cases, the local current and residual distributions of stresses and strains can be described within the simplified two-dimensional models, which allows application of small FE for their description without any significant increase of the calculation time. Transfer of a certain array of calculated data to the full three-dimensional model of a large-sized

structure with its own finite element breakdown (such, which allows conducting the respective real-time calculations) with further calculation of the general SSS is formalized by the algorithm of multiscale interconnection between the calculation levels.

So, within the scope of this work, two scale levels were considered, which are typical for the problems of prediction of the kinetics of temperature and stress-strain states of large-sized structures, namely the mezolevel, on which the welding processes are usually described, with the characteristic spatial scale of approximately 1 mm, and the macrolevel, which is characteristic for the problems of deformation of large-sized structures with the spatial scale of 1 cm and more. A finite element solution of the respective joint interrelated problems was used for a numerical description of the kinetics of the nonstationary temperature and stress-strain states in the site welding region. The respective algorithms and mathematical formulations are a development of complex approaches developed by the authors [12–14], in the context of a multiscale problem statement.

So, the kinetics of the temperature field was predicted by a numerical solution of a nonstationary heat-conductivity equation of a fast-moving heat source in the two-dimensional approximation. It allowed not only taking into account the temperature dependencies of heat conductivity and heat capacity of the structure material, but reduce as much as possible the spatial breakdown of the calculation area without any essential increase of calculation time.

Based on the calculated temperature fields in the structure cross-section at its site welding, the boundary problem of nonstationary thermoplasticity of the structure material was formulated with the respective finite element realization based on eight node FE (Figure 1). So, increment of the strain tensor can be presented in keeping with following expression:

$$d\varepsilon_{ij} = d\varepsilon_{ij}^e + d\varepsilon_{ij}^p + \delta_{ij}d\varepsilon_T, \qquad (1)$$

where $d\varepsilon_{ij}^e$; $d\varepsilon_{ij}^p$; $\delta_{ij} d\varepsilon_T$ are the components of strain tensor increase due to the elastic deformation mechanism, instant plasticity strains and kinetics of the nonuniform temperature field, respectively.

Strain increase, which is due to the kinetics of temperature T, is equal to

$$d\varepsilon_T = \alpha \, dT, \qquad (2)$$

where α is the coefficient of linear temperature expansion of the material.

The tensors of mechanical stresses σ_{ij} and elastic strains $d\varepsilon_{ij}^e$ are related to each other by the generalized Hooke's law, i.e.
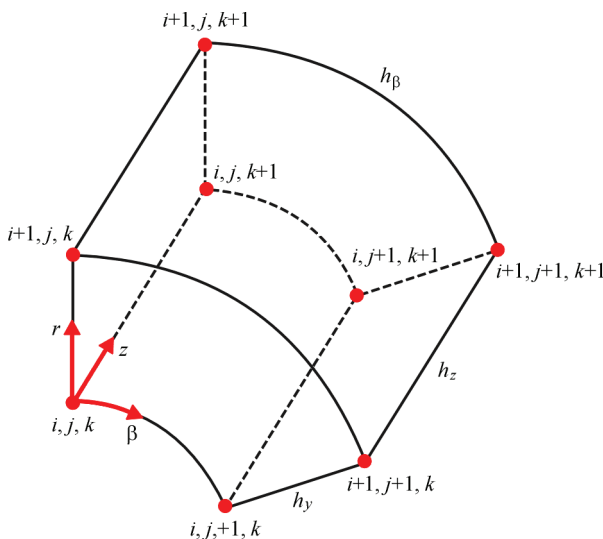

Figure 1. Scheme of an eight-node finite element in a cylindrical system of coordinates

$$\varepsilon_{ij}^e = \frac{\sigma_{ij} - \delta_{ij}\sigma}{2G} + \delta_{ij}(K\sigma + \varphi), \qquad (3)$$

where $\sigma = \dfrac{(\sigma_{\beta\beta} + \sigma_{zz} + \sigma_{rr})}{3}$ is the mean value of normal components of stress tensor σ_{ij}, $K = \dfrac{1-2\nu}{E}$ is the bulk compression modulus; $G = \dfrac{E}{2(1+\nu)}$ is the shear modulus; E is the Young's modulus; ν is the Poisson's ratio; ν is the bulk strain.

Depending on the stressed state in a specific FE, increase of instant plasticity strains $d\varepsilon_{ij}^p$ can be calculated, using a linear dependence of scalar function Λ and deviator component of the stress tensor, namely [12]:

$$d\varepsilon_{ij}^p = d\Lambda(\sigma_{ij} - \delta_{ij}\sigma). \qquad (4)$$

Quantitative value of function Λ depends on the stressed state in the considered area of the structure, as well as on the shape of material yield surface Φ, which is characterized by yield limit σ_y:

$$d\Lambda = 0, \text{ if } \sigma_i < \sigma_y,$$
$$d\Lambda > 0, \text{ if } \sigma_i = \sigma_y, \qquad (5)$$
$$\sigma_i > \sigma_y \text{ state is inadmissible.}$$

where $\sigma_i = \sqrt{\dfrac{1}{2}\sigma_{ij}\sigma_{ij}}$ is the stress intensity.

The strain tensor growth can be presented in the form of superposition of the increase of the respective components [13]:

$$\Delta\varepsilon_{ij} = \Psi(\sigma_{ij} - \delta_{ij}\sigma) + \delta_{ij}(K\sigma + \Delta\varepsilon_y) -$$
$$- \frac{1}{2G}(\sigma_{ij} - \delta_{ij}\sigma)^* - (K\sigma)^*, \qquad (6)$$

where δ_{ij} is the Kronecker symbol, "*" refers the respective variable to the previous tracking step; Ψ is the material state function, which determines the plastic flow condition according to Mises criterion:

$$\Psi = \frac{1}{2G}, \text{ if } \sigma_i < \sigma_y,$$
$$\Psi > \frac{1}{2G}, \text{ if } \sigma_i = \sigma_y, \qquad (7)$$
$$\sigma_i > \sigma_y \text{ state is inadmissible.}$$

Determination of Ψ function is performed by iteration at each step of numerical tracking (by time or by loading increase), which allows solving the non-linearity by the plastic flow of the material. Based on the specific meaning of Ψ function from (7), the strain field is determined at each loading step, taking into account $\sigma_y(T)$ dependencies:

$$\Delta\varepsilon_{ij} = \left(\Psi - \frac{1}{G}\right)(\sigma_{ij} - \delta_{ij}\sigma). \qquad (8)$$

Here, at each step of iteration by Ψ, stresses σ_{ij} are calculated according to the following algorithm (summing up is performed by the repeating indices) [14]:

$$\sigma_{ij} = \frac{1}{\Psi}\left(\Delta\varepsilon_{ij} + \delta_{ij}\frac{\Psi - K}{K}\Delta\varepsilon\right) + J_{ij}, \qquad (9)$$

where

$$\Delta\varepsilon = \frac{\Delta\varepsilon_{ii}}{3},$$
$$J_{ij} = \frac{1}{\Psi}\left[(b_{ij} - \delta_{ij}b) + \delta_{ij}\left(K\sigma^* - \frac{\Delta\varepsilon_y}{K}\right)\right],$$
$$b = \frac{b_{ii}}{3}, \qquad (10)$$
$$b_{ii} = \left(\frac{\sigma_{ij}}{2G}\right)^* + \delta_{ij}\left[\sigma^*\left(K - \frac{1}{2G}\right)^* - \Delta\varphi\right].$$

The connection between the components of strain tensor $\Delta\varepsilon_{ij}$ and displacement increment vector ΔU_i has the following mathematical expression:

$$\Delta\varepsilon_{ij} = \frac{\Delta U_{i,j} + \Delta U_{j,i}}{2}, \qquad (11)$$

where the comma denotes differentiation within FE.

The stress tensor components satisfy the equations of statics for internal FE and the boundary conditions for the surface elements. In their turn, the components of $\Delta U_i = (\Delta U, \Delta V, \Delta W)$ vector meet the corresponding conditions on the boundary.

The solved system of equations in the variables of displacement increment vector in FE nodes at each step of tracking and iteration by Ψ is determined by minimizing the following functional (Lagrangian variational principle):

$$E_I = -\frac{1}{2}\sum_V (\sigma_{ij} + J_{ij})\Delta\varepsilon_{ij}V_{m,n,r} + \sum_{S_P} P_i\Delta U_i\Delta S_P^{m,n,r}, \qquad (12)$$

where $\displaystyle\sum_V$ is the operator of the sum of internal FE; $\displaystyle\sum_{S_P}$ is the operator of the sum of surface FE, on which the components of force vector P_i are assigned, i.e. the subsequent system of equations allows deriving the solution in the components of the displacement increment vector at each step of tracking and iteration by Ψ for a specific FE:

$$\frac{\partial E_I}{\partial \Delta U_{m,n,r}} = 0, \quad \frac{\partial E_I}{\partial \Delta V_{m,n,r}} = 0, \quad \frac{\partial E_I}{\partial \Delta W_{m,n,r}} = 0. \qquad (13)$$

23

At consideration of cylindrical structures with a circumferential weld, the assumptions of a two-dimensional model of a plane stressed state can be used. In such a description the stress tensor σ_{ij} ($i, j = r, \beta, z$) includes four nonzero components σ_{rr}, σ_{zz}, $\sigma_{\beta\beta}$, σ_{rz}. Strain increase tensor $\Delta\varepsilon_{ij}$ contains similar nonzero components. The components of this tensor are connected with the components of displacement increase ΔU_r and ΔU_z by the following relationships:

$$\Delta\varepsilon_{rr} = \frac{\partial \Delta U_r}{\partial r}, \quad \Delta\varepsilon_{zz} = \frac{\partial \Delta U_z}{\partial z},$$

$$\Delta\varepsilon_{rz} = \frac{1}{2}\left(\frac{\partial \Delta U_r}{\partial z} + \frac{\partial \Delta U_z}{\partial r}\right), \quad \Delta\varepsilon_{\beta\beta} = \frac{\Delta U_r}{r}. \quad (14)$$

The connection between σ_{ij} and $\Delta\varepsilon_{ij}$ can be described as follows:

$$\begin{aligned}
\sigma_{rr} &= A_1 \Delta\varepsilon_{rr} + A_2(\Delta\varepsilon_{\beta\beta} + \Delta\varepsilon_{zz}) + Y_{rr}, \\
\sigma_{\beta\beta} &= A_1 \Delta\varepsilon_{\beta\beta} + A_2(\Delta e_{rr} + \Delta\varepsilon_{zz}) + Y_{\beta\beta}, \\
\sigma_{zz} &= A_1 \Delta\varepsilon_{zz} + A_2(\Delta\varepsilon_{rr} + \Delta\varepsilon_{\beta\beta}) + Y_{zz}, \\
\sigma_{rz} &= A_3 \Delta\varepsilon_{rz} + Y_{rz},
\end{aligned} \quad (15)$$

where

$$A_1 = \frac{\Psi + 2K}{3K\Psi}, \quad A_3 = \frac{1}{\Psi}, \quad A_2 = A_1 - A_3 = \frac{\Psi - K}{3K\Psi},$$

$$Y_{ij} = \frac{1}{\Psi}\left(\frac{\sigma_{ij} - \delta_{ij}\sigma}{2G}\right)^* + \delta_{ij}\frac{(K\sigma)^* - \Delta\varphi}{K}. \quad (16)$$

Equations (15), (16) form a system of linear algebraic equations for strains (displacements), which is the base of finite element realization of the numerical solution.

As noted above, application of a similar approach for description of the temperature state, current and residual SSS of a large-sized structure based on fine spatial breakdown is complicated or impossible, because of an excess resource consumption of such a problem. However, increase of the steps of spatial breakdown in the macroscale approach can lead to a loss of accuracy of the calculation model right up to a significant distortion of the results. Therefore, the results obtained in keeping with the mezoscale calculation were used as the initial data for macroscale calculation, but taking into account the integral interpretation required for it. That is, in order to track the state of one FE of the macroscopic problem it is necessary to use an averaged state of several FE of the mezoproblem during the entire technological cycle of site welding. The result of such averaging should be the integral values of mechanical properties of the material of a nonuniformly heated structure and parameters of its current deformed state. So, a simplified approach can be used for averaging the material mechanical properties, namely Young's modulus, the coefficient of linear thermal expansion and yield limit, similar to the rule of mixtures. This is substantiated by the characteristically small gradients of properties at distances of the order of FE size, that is necessary for a stable solution of the boundary problem of nonstationary thermoplasticity in the definition of (1)–(13). Therefore, if the state of mn element in the macroproblem is described by several elements ij in the mezoscale definition, the respective mechanical characteristics can be evaluated as follows:

$$E'_{mn} = \frac{\sum_i \sum_j E(T_{ij}) s_{ij}}{\sum_i \sum_j s_{ij}}, \quad \alpha'_{mn} = \frac{\sum_i \sum_j \alpha(T_{ij}) s_{ij}}{\sum_i \sum_j s_{ij}}, (17)$$

where s_{ij} is the area of ij-th FE; T_{ij} is the temperature in ij point; " ′ " refers the parameter to the macroproblem.

It should be noted that relationship (17) was formulated in a two-dimensional definition, but averaging from a two-dimensional to a three-dimensional problem can be realized similarly.

Development of SSS in a macroscopic definition requires allowing for the force factor, namely nonuniform deformation of the material. In order to calculate the distribution of the current and residual SSS, which satisfies the condition of equilibrium (13) and does not get any significant distortion on coarse spatial grids, the following spatial averaging was proposed for the numerical components of the matrix (15)–(16) and material state function Ψ, defined according to (7):

$$A'_{kmn} = \frac{\sum_i \sum_j A_{k\,mn} s_{ij}}{\sum_i \sum_j s_{ij}}, \quad k = 1, 2, 3;$$

$$Y'_{mn} = \frac{\sum_i \sum_j Y_{ij} s_{ij}}{\sum_i \sum_j s_{ij}}; \quad \Psi'_{mn} = \frac{\sum_i \sum_j \Psi_{ij} s_{ij}}{\sum_i \sum_j s_{ij}}. \quad (18)$$

Solution of the system of linear algebraic equations (15) in the framework of formulation of a macroscopic problem of SSS allows obtaining equilibrium distributions of the structure stress and strain fields at each tracking step.

The limits of applicability and features of the developed multiscale approach were studied on the characteristic example of site welding of circumferential joints of a cylindrical structure from AMg6 aluminium alloy ($E = 71$ GPa, $v = 0.3$, $\sigma_y = 170$ MPa, $\alpha = 2.26\cdot10^{-5}$ 1/°C at 20 °C) of diameter $D = 3900$ mm and with wall thickness $t = 10$ mm; welding was performed in the following mode: $U = 20$ V, $I = 380$ A,
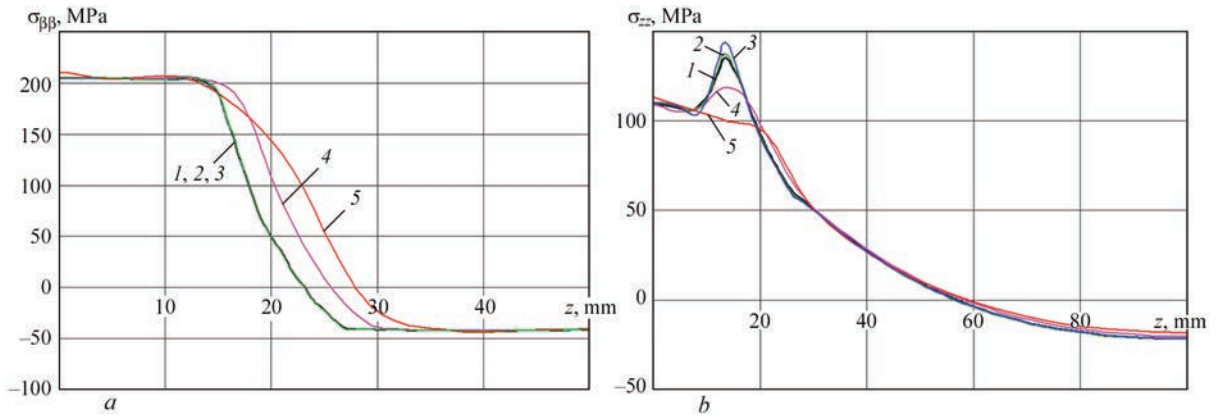
Figure 2. Calculated distribution of residual postweld circumferential $\sigma_{\beta\beta}$ (*a*) and axial σ_{zz} (*b*) stresses: *1* — control 3D calculation at $h_r = h_z = h_\beta = 1$ mm; *2* — multiscale calculation at $h_r = 4$ mm; $h_z = h_\beta = 1$ mm; *3* — multiscale calculation at $h_r = 8$ mm, $h_z = h_\beta = 1$ mm; *4* — multiscale calculation at $h_z = 4$ mm, $h_r = h_\beta = 1$ mm *5* — multiscale calculation at $h_z = 8$ mm; $h_r = h_\beta = 1$ mm (in Figure 2, *a*, curves *1*, *2* and *3* practically coincide)

$v_w = 2.23$ mm/s. It should be noted that selection of the studied structure corresponds to the typical structural solutions for space applications, in particular, rocket-carrier fuel tanks, although the versatility of the proposed approach allows consideration of a wide range of materials, structural elements and welding technologies.

The mezoscale definition was realized within the joint solution of the problem of temperature field kinetics in welding and development of an elastoplastic deformed and stressed states of the structure in the area of the joint in the two-dimensional definition, which allowed application of fine and regular spatial finite element breakdown with the linear size of the element $h_r = h_z = 1$ mm in the radial and axial directions. At formulation of the three-dimensional problem the linear size of finite elements in the radial and axial directions was multiplied by 2, 4 and 8 times, and the stress and strain fields, obtained within the multiscale formulation of the problem and direct three-dimensional modeling with spatial step $h_r = h_z = h_\beta = 1$ mm, were compared.

As shown in Figure 2, comparisons of the calculated distributions of circumferential $\sigma_{\beta\beta}$ and axial σ_{zz} stresses for different macroscale spatial breakdown confirm the high degree of correspondence of the results of multiscale modeling to direct calculations. Significant differences appear, when the characteristic spatial distribution of local stresses becomes smaller than one step of the macroscale problem, where the respective averaging takes place (in particular, at h_z increase up to 8 mm). Here, in other structure areas, where the residual stress gradient is less significant, the correspondence of the calculations by two approaches is high (error of less than 2 %). Such an accuracy of the multiscale approach is related to the physical essence of mathematical formulation (18), namely transfer of the averaged internal energy of

the deformed material. It allows application of the proposed procedure for analysis of the stressed state of large-sized welded structures, in particular under the impact of complex operational load, as well as for brittle strength analysis. It should be noted that the maximum value of residual stresses is somewhat higher than the room temperature material yield limit. It is attributable to the fact that the cylindrical structure is characterized by a two-axial stressed state, so that the stress intensity value σ_i is somewhat lower than some individual components of the stress tensor, but σ_i itself determines the material flow surface Φ, in keeping with the Mises yield condition, in particular in the form of (5).

Similar calculations of strain field kinetics showed that the influence of multiscale approach on the error of the results of prediction of the residual deformed state is significantly higher (Figure 3). So, increase of h_r within the selected range only slightly influences the calculated value of circumferential strains $\varepsilon_{\beta\beta}$ (the error is equal to approximately 1.7 %), whereas for longitudinal strains ε_{zz} the satisfactory result of multiscale modeling is observed for a slight increase of spatial breakdown (two times up to 2 mm size). The conclusion about the relatively low possibilities for h_z increase is similar: rarefaction of spatial breakdown up to 4 times allows obtaining a satisfactory value of multiscale prediction error $\varepsilon_{\beta\beta}$ (error of less than 7 %), while for obtaining correct results for ε_{zz}, h_z increase should not be greater than 2 times up to 2 mm size.

Such analysis results are explained by that one of the main assumptions of finite element modeling is the uniformity of properties of each of the FE. A significant increase of element size leads to incorrect definition of the problem, which is manifested, primarily, in the strain field not corresponding to the true solution on fine meshes. This instability, however, corresponds, first of all to the deformed state in the
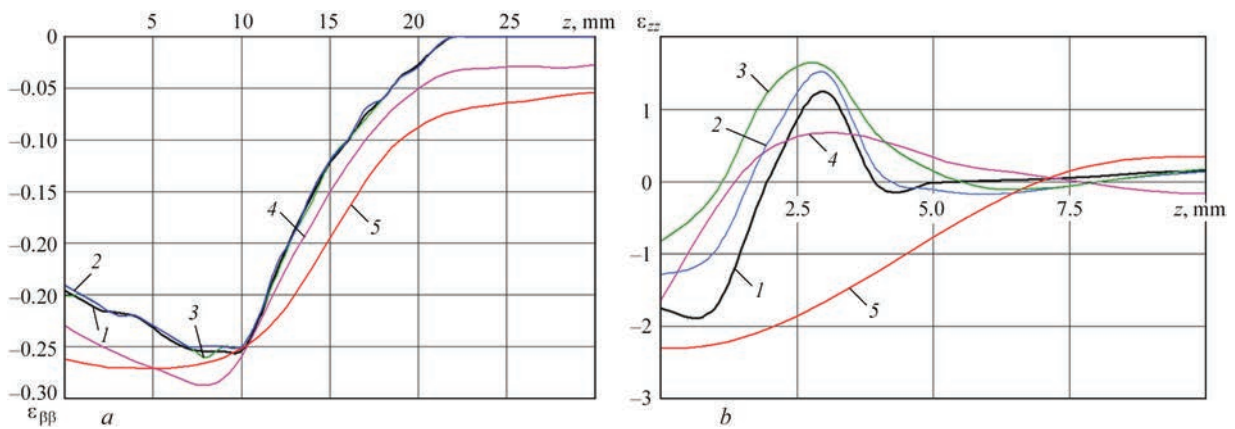
25

Figure 3. Calculated distribution of residual postweld circumferential $\varepsilon_{\beta\beta}$ (*a*) and axial ε_{zz} (*b*) strains (see Figure 2 for description of curves *1–5*)

axial direction, where the maximum strain gradient is observed, whereas for $\varepsilon_{\beta\beta}$ and stressed state the possibilities for optimization of calculations for large-sized structures by application of the proposed multiscale approach are much higher.

As shown by calculations, simultaneous increase of spatial steps in the radial and axial directions only slightly changes the made conclusions, as the instability of individual solutions as a result of rarefaction in the axial direction prevails.

Despite the fact that in this work a concrete case of a welded large-sized structure from an aluminium alloy was considered, the derived results are sufficiently general to enable a wider application of the developed procedure and general recommendations for the cases of structures from other materials, of different geometrical dimensions, or those manufactured with application of other technologies or modes of site welding. A fundamental difference will be in the current and residual stress and strain gradients, which will determine the admissible linear averaging size (17), (18). For instance, reduction of the HAZ (at application of smaller heat input or at lower heat conductivity of the material of the large-sized structure) will determine the proportionally smaller size of spatial breakdown of the macroscopic problem in the welding area, but larger on the periphery, where the respective stress and strain gradients will be significantly smaller.

CONCLUSIONS

1. In order to develop efficient methods of analysis of the technological processes of welding without any significant increase of resource intensity of the respective calculations, a multiscale approach of numerical prediction of the kinetics of temperatures and stress-strain state was proposed. This procedure is based on finite element solution of the problems of nonstationary thermoplasticity, characteristic for fusion welding technologies, on the mezoscale level with fine spatial breakdown of the structure in a two-dimensional defi-

nition with subsequent transfer of a certain volume of the calculation data into a three-dimensional macroscopic model with a sparse mesh. For this purpose, the algorithms of the respective averaging of the properties and parameters of the stressed-strained state were proposed, which allows conducting analysis of the state of large-sized structures during welding without the need to involve considerable computing power.

2. The high correspondence of the results of finite element calculations of the stressed state within the developed model and control calculations by standard approaches was demonstrated in the case of site welding of a circumferential weld of a large-sized pressure vessel from AMg6 aluminium alloy. It is shown that a significant increase (up to eight times) of spatial finite element breakdown is possible, until the characteristic spatial breakdown of local stresses becomes smaller than one step of the macroscale problem, where the respective averaging takes place.

3. It is shown that the possibilities of application of the proposed approach for prediction of the deformed state of large-sized structures are limited as a result of shrinkage processes at nonuniform heating in welding. This is due to high calculated strain gradients, particularly in the axial direction. In such a case, spatial averaging of the properties of the material of the structure being welded, may lead to convergence of the problem within the finite element definition, and to a wrong solution.

REFERENCES

1. Deng, D., Murakawa, H., Liang, W. (2007) Numerical simulation of welding distortion in large structures. *Comput. Methods Appl. Mech. Engrg.*, **196**, 4613–4627. DOI: http://dx.doi.org/10.1016/j.cma.2007.05.023

2. Park, J.-U., An, G., Woo, W. et al. (2014) Residual stress measurement in an extra thick multi-pass weld using initial stress integrated inherent strain method. *Marine Structures*, **39**, 424–437. DOI: http://dx.doi.org/10.1016/j.marstruc.2014.10.002

3. Zhang, L., Michaleris, P., Marugabandhu, P. (2007) Evaluation of applied plastic strain methods for welding distortion

prediction. *J. of Manufacturing Sci. and Eng.*, **129**, 1000–1010. DOI: http://dx.doi.org/10.1115/1.2716740

4. Liu, R.-F., Wang, J.-C. (2022) Application of finite element method to effect of weld overlay residual stress on probability of piping failure. *Inter. J. of Pressure Vessels and Piping*, **200**, 104812. DOI: https://doi.org/10.1016/j.ijpvp.2022.104812

5. Li, S., Coraddu, A., Oneto, L. (2022) Computationally aware estimation of ultimate strength reduction of stiffened panels caused by welding residual stress: From finite element to data-driven methods. *Engineering Structures*, **264**, 114423. DOI: https://doi.org/10.1016/j.engstruct.2022.114423

6. Bayraktar, C., Demir, E. (2022) A thermomechanical finite element model and its comparison to inherent strain method for powder-bed fusion process. *Additive Manufacturing*, **54**, 102708. DOI: https://doi.org/10.1016/j.addma.2022.102708

7. Takezawa, A., To, A.C., Chen, Q. et al. (2020) Sensitivity analysis and lattice density optimization for sequential inherent strain method used in additive manufacturing process. *Computer Methods in Applied Mechanics and Engineering*, **370**, 113231. DOI: https://doi.org/10.1016/j.cma.2020.113231

8. Liangfeng, L., Cheng, L., Jie, S., Yansong, Z. (2022) Numerical prediction of welding deformation in ship block subassemblies via the inhomogeneous inherent strain method. *J. of Manufacturing Processes*, **80**, 860–873. DOI: https://doi.org/10.1016/j.jmapro.2022.06.044

9. Honaryar, A., Iranmanesh, M., Liu, P., Honaryar, A. (2020) Numerical and experimental investigations of outside corner joints welding deformation of an aluminum autonomous catamaran vehicle by inherent strain/deformation FE analysis. *Ocean Engineering*, **200**, 106976. DOI: https://doi.org/10.1016/j.oceaneng.2020.106976

10. Makhnenko, O.V., Muzhichenko, A.F., Seyffarth, P. (2009) Application of mathematical modelling in thermal straightening of shipbuilding panels. *Paton Welding J.*, **1**, 6–11.

11. Makhnenko, V.I., Milenin, A.S., Semyonov, A.P. (2007) Mathematical modelling of thermal-deformation processes in braze-welding of butt joints of the titanium-aluminium type. *Paton Welding J.*, **11**, 5–9.

12. Makhnenko, V.I., Pochinok, V.E. (2006) *Strength calculation of welded joints with crack-like imperfections*. PWI, NASU.

13. Makhnenko, V.I. (2006) *Safe service life of welded joints and assemblies of modern structures*. Kyiv, Naukova Dumka [in Russian].

14. Velikoivanenko, E., Milenin, A., Popov, A. et al. (2019) Methods of numerical forecasting of the working performance of welded structures on computers of hybrid architecture. *Cybernetics and Systems Analysis*, 55(**1**), 117–127. DOI: https://doi.org/10.1007/s10559-019-00117-8

ORCID

O.S. Milenin: 0000-0002-9465-7710

CONFLICT OF INTEREST

The Authors declare no conflict of interest

CORRESPONDING AUTHOR

O.S. Milenin
E.O. Paton Electric Welding Institute of the NASU
11 Kazymyr Malevych Str., 03150, Kyiv, Ukraine.
E-mail: asmilenin@ukr.net

JOURNAL HOME PAGE

https://patonpublishinghouse.com/eng/journals/tpwj

STRUCTURE AND PROPERTIES OF INGOTS PRODUCED FROM SHEET SCRAPS OF VT1-0 TITANIUM BY ELECTROSLAG REMELTING IN AN OPEN MOULD

D.I. Bilonyk[1], O.Ye. Kapustyan[1], I.A. Ovchynnykova[2], I.M. Bilonyk[1], G.M. Laptieva[1]

[1]National University "Zaporizka politekhnika"
64 Zhukovskogo Str., 69063, Zaporizhzhya, Ukraine
[2]Zaporizhzhya National University
66 Zhukovskogo Str., 69600, Zaporizhzhya, Ukraine

ABSTRACT

Analysis of technologies, allowing titanium wastes to be used in the melting process in ingot production, was performed. It is shown that for this purpose, a promising and cost-effective schematic is the one which includes electroslag remelting with preliminary manufacture of a consumable electrode completely from standard wastes of sheet scraps of VT1-0 titanium. The structure and properties of electroslag ingots of titanium of 90×90 mm cross-section and 85 mm diameter was studied. The ingots were produced with application of electroslag remelting in an open mould with sliding current conduit and the slag pool surface protection by argon. Chemical composition of electroslag ingots of unalloyed titanium practically does not differ from that of titanium of VT1-2, VT1-L grades, and a whole range of grades of unalloyed titanium from foreign manufacturers, except for a somewhat higher content of oxygen and nitrogen. Ultrasonic testing of the ingots did not reveal any internal defects. Macrostructure, which was studied on longitudinal and transverse templates, is coarse-crystalline, dense and homogeneous without any defects of technological origin. The angle of inclination of the columnar crystallites to the ingot axis is 40–45°, grain size is 1.8–2.5 mm. The microstructure consists of transformed β-grains of 140–175 μm size. After annealing (620 °C), the mechanical properties of electroslag ingots were as follows: HB = 224; σ_t = 590 MPa; $\sigma_{0.2}$ = 560 MPa; δ = 7.5 %; ψ = 13.5 %. Technical measures were determined to improve the ductility of electroslag titanium by reducing the content of oxygen and nitrogen in the ingots, and refining the cast grain size. Technological properties of electroslag titanium (cutting treatment and weldability) are on the level of VT1-L. The possibility of pressure treatment (hot forging) was established with deformation coefficients of 40 and 90 % of titanium from electroslag ingots. The manufactured semi-finished products did not have any internal or surface defects.

KEYWORDS: processing, sheet scraps, titanium, electron beam melting, electroslag process, ingot, structure, chemical composition, mechanical properties, technological properties, hot forging

INTRODUCTION

For the development of modern electrometallurgy using secondary raw materials, titanium wastes are of particular importance. The most complete and rational use of wastes is a promising and priority way to make titanium products cheaper, which will undoubtedly strengthen the economic positions of the titanium industry. The use of wastes of titanium and its alloys in melting for production of serial titanium alloys, shaped casting, ferrotitanium and other products is the most rational and effective method of recycling [1].

Despite the additional costs caused by the preparation of wastes for melting, including sorting, determination of the chemical composition and impurities content, cleaning from technological contaminants (lubricating-cooling fluids, oil, oxidized as a result of thermal cutting of the surface), every 10 % of titanium wastes, which are additionally introduced to the charge, will reduce its cost by 5–8–%. Also, producing a one ton of ingot, it is possible to save up to 100 kg of titanium sponge and 5–10 kg of alloy elements [2].

The main methods of titanium melting, which allow using titanium wastes are vacuum-induction and vacuum-skull melts, electron beam and electroslag remelts. Vacuum-induction melting was developed by O.O. Fogel. Equipment for this process was developed in the USA (Retech Systems LLC) [3] and Germany (ALD Vacuum Technologies) [4]. In Ukraine, this technology is currently not applied.

In [1] it is proved that the most effective unit for melting of titanium wastes and its alloys is a vacuum-skull furnace, which operates on the technology of skull-consumable electrode (SCE). The most important economic advantage of the technology and SCE furnaces is a significant reduction in the volume of works on titanium wastes preparation for melting. The SCE technology, which uses titanium wastes, also provides the production of consumable electrodes for further vacuum-arc remelting (VAR). The combination of SCE and VAR technologies replaces a threefold VAR during melting of titanium Ti-10-2-3 and Ti–6Al–4V alloys [1].

Due to intensive research works at the PWI of the NASU, in the development of modern equipment and
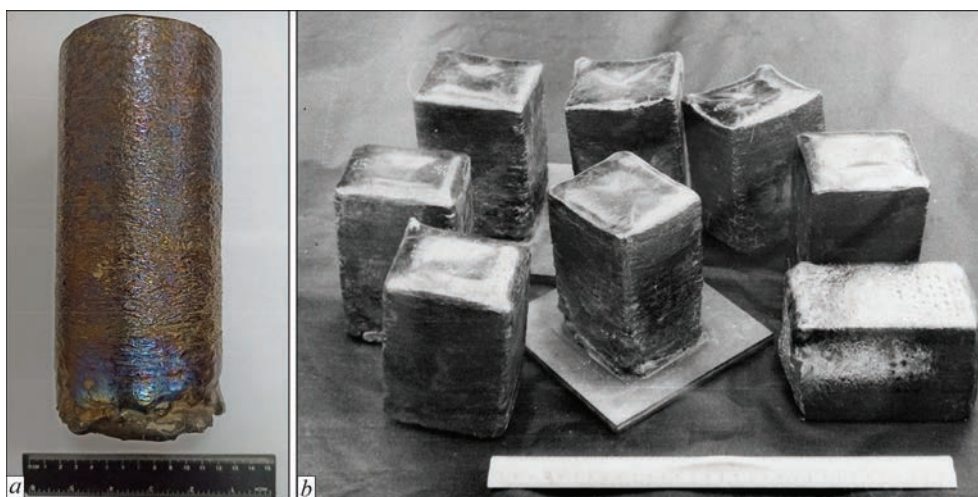
Figure 1. Titanium semi-finished products of two sizes, mm: diameter is 85 (*a*), cross-section is 90×90 (*b*)

technologies in the field of production of titanium ingots and slabs and other titanium products, the leading position was taken by the process of electron beam melting [5–8]. Industrial implementation and further improvement of titanium electron beam melting technology was carried out at such Ukrainian enterprises as SE "Titan Scientific and Production Center" of PWI", LLC "International Company "ANTARES", LLC "ZTMK", as well as in China, Germany, USA and other countries. The technological flexibility of the process of electron beam melting allows a titanium of different grades, shapes and sizes, as well as up to 30–40 % of a low-grade sponge (TG-Tv, TG-op) to be used quite widely in the production. For example, to produce ingots of unalloyed titanium (CP-titanium) of grades VT1-0, Grade 2, the technology of a one-time electron beam melting with an cold hearth was developed. The charge can also be supplemented with specially prepared titanium wastes in the form of chips and bottom parts of slabs [9]. This makes it possible to effectively reduce the cost of products both at the domestic as well as foreign markets.

Electroslag technology is less demanded, which is predetermined by some of the technical and technological nature of the production of commercial titanium ingots. Although, electroslag melting and, especially, the chamber electroslag process are successfully used for melting of low-weight titanium with a fairly wide ability of influencing their chemical composition, structure and properties [10, 11].

Certainly, both scientific and practical interest is represented by the possibility of using 100 % of the wastes of sheet scrap of titanium in the electroslag remelting. In [12], the rationality is substantiated and the fundamental possibility is shown of using the electroslag process in an open mould with a sliding current conduit for melting titanium ingots with the use of consumable electrodes, completely manufactured from

the conditional wastes of sheet scrap of VT1-0 titanium. The titanium ingots are melted with 90×90 mm cross-sections and 85 mm diameter (Figure 1).

The further development in this direction [12] consisted in determination of the qualitative characteristics and technological properties of this material, which include: chemical composition, including gases content; physical homogeneity (macrostructure), microstructure; standard mechanical properties. On the basis of the obtained data, it is possible to give recommendations for the manufacture of specific products from electroslag titanium, and the chemical composition will allow establishing a list of aggressive environments, in which products from electroslag titanium are the most rational for operation.

It should also be taken into account that technological, economic and in general the possibility of manufacturing products from electroslag titanium is determined by such properties, such as cutting treatment, weldability and ability of titanium electroslag ingots to deformation treatment. This requires studying the possibility of using these processes for the manufacture of parts and equipment from electroslag titanium.

The aim of this work is to determine the main indices of metallurgical quality and technological properties of titanium ingots produced with the use of electroslag process in an open mould with a sliding current conduit, protecting the surface of the slag pool with argon and using consumable electrodes, produced entirely from the conditional wastes of scraps of VT1-0 titanium.

MATERIALS AND METHODS OF INVESTIGATIONS

The technology, based on which titanium electroslag ingots (Ti — base; C — 0.024 %; Fe — 0.06 %; Si — 0.05 %; O_2 — 0.25 %; N_2 — 0.058 %; H_2 — 0.016 %) were produced, is presented in [12].

In this work, the quality of the ingots was investigated by the following indices: macro- and microstructure; mechanical properties; cutting and pressure treatment; weldability.

The ingots were preliminary mechanically processed in a lathe to a depth of 2.5 mm in order to remove the alphated layer (Figure 2, *a*) for the further ultrasonic testing and pressure treatment. Ultrasonic testing of ingots was performed at the ZTMK LLC with the use of a flaw detector UD4-T and sensor 5K6.

The macrostructure of the ingots was investigated on longitudinal and transverse templates after etching with a 20 % solution of HF + 20 % HNO_3 + 60 % H_2O. The size of the cast grain was determined by the linear secant method of A.A. Glagolev [13]. Microstructure was detected by the same reagent on polished and etched sections and studied in the metallographic NEOPHOT-32 microscope at a magnification of 300–500 times.

Mechanical tests of cast electroslag metal [14] and welded butt joint [15] were performed in the computerized system Instron-8862. The mechanical properties of titanium electroslag ingots were determined after annealing at a temperature of 620 °C. The results were compared with the mechanical properties given for commercial titanium VT1-L, as well as α-alloys TL3 and VT5l in [16].

The cutting treatment during machining, drilling and cutting outer threads was evaluated by comparing

Figure 2. Ingot of 85 mm diameter with the alphated layer removed by lathe (*a*) and specimens for forging produced of this ingot (*b*)

technological samples from the electroslag ingots of titanium and VT1-L titanium in the process of manufacture. Melting of ingots from VT1-L titanium with a diameter of 80 mm for comparative cutting treatment characteristics was performed by a vacuum-arc remelting with a nonconsumable electrode in a vacuum-arc skull furnace [17]. The melting was conducted with a copper water-cooled electrode with a tungsten tip in a crucible made of grade MPG-7 graphite. As the starting charge materials waste scraps of conditional VT1-0 titanium were used. Before starting the works, the provided materials were preliminary mechanically ground to a fraction of 5–15 mm.

On the technological samples, finished, semi-finished and rough surface treatments were provided. Research procedures, equipment, tools and cutting modes were chosen according to recommendations [18, 19].

Machining was performed by cutters with hard-alloy plates from VK-8 alloy of the following geometry: $\gamma = 0°$, $\alpha = 12°$, $\varphi = 14°$, $\varphi_1 = 45°$. The cutting rate is 30 m/min, the feed rate is 0.5 mm/rev, the cutting depth is 2.5 mm.

Drilling was performed with a 20 mm diameter drill of a quick-cutting steel P9F5 with the following geometry: $\gamma = 3°$, $\alpha = 12°$, $2\varphi = 120°$, $2\varphi_0 = 75°$, the angle of inclination of a spiral groove is 27°. The cutting rate is 20 m/min, the feed rate is 0.1 mm/rev.

Metric thread was cut by cutters with hard-alloy plates of VK-8 alloy with a cutting rate of 25 m/min.

The studies of weldability were performed according to the recommendations [20] on specimens with the sizes of 55×30×5 mm made of electroslag titanium ingots. The specimens were welded by a double-sided butt weld using nonconsumable electrode argon-arc welding with titanium filler (wire VT1-00 GOST 27265–87) on the following modes: current — 110–130 A, voltage — 12–18 V, argon (A class) flow rate is 12–16 l/min. Mechanical properties of the weld were determined according to GOST 6996–66, type of the specimen is XX IV. The produced joints were also tested for tightness by the kerosene sample according to GOST 3242–79. One side was coated with a water suspension of chalk and dried. The opposite side was moistened 2–3 times with kerosene. They were exposed during four hours.

Pressure treatment was performed by the method of hot forging at the SE "UkrNDIspetsstal" in the hydraulic forging press with an effort of 2 MN. For this purpose, from one of the ingots, the specimens (Figure 2, *b*) were produced, which were subjected to varying degree of deformation of 45 and 90 %. The forging technology was accepted the same as for standard ingots of VT1-0 titanium [21] by the following technological mode:
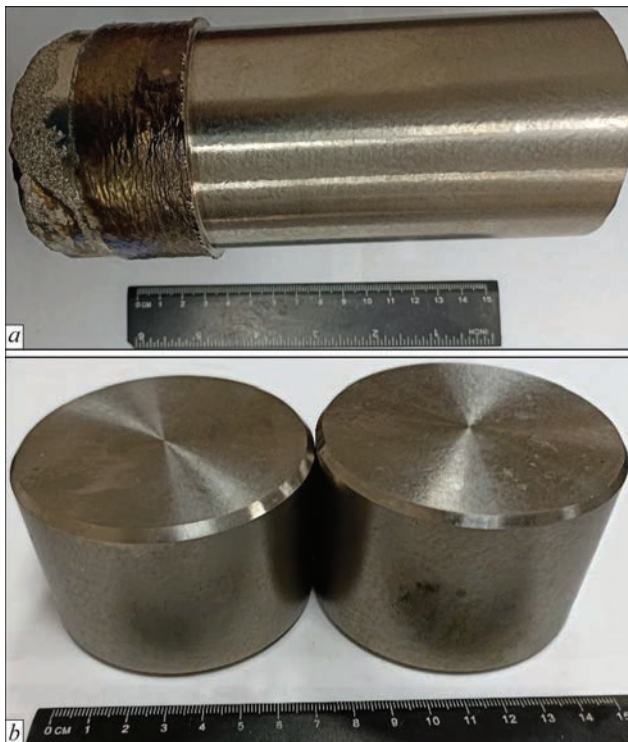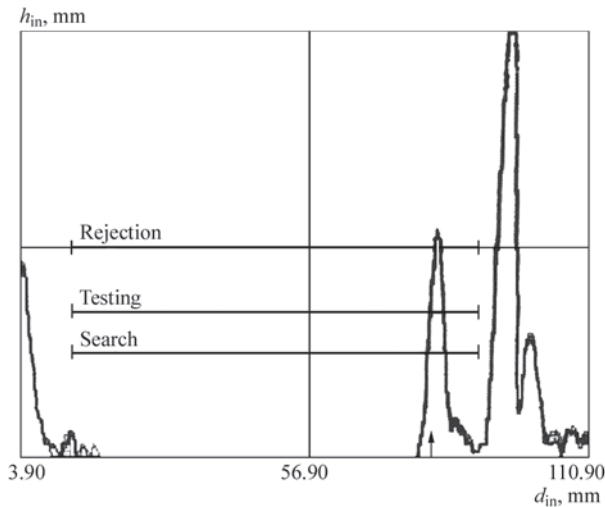
Figure 3. Scan of ultrasonic testing: $T_A = 27.6$ μs; $y_A = 86.2$ mm

preheating of heads before forging, °C 200–220
heating the billets in the furnace to temperature, °C. . . . 900–930
deformation of billets in a one pass, %–20–22
temperature of forging end is not less than, °C. 750
annealing temperature, °C. 620–660
cooling of billets . . . . in air to the environment temperature

RESEARCH RESULTS AND THEIR ANALYSIS

Ultrasonic testing showed that there are no internal defects and large non-metallic inclusions in the ingots. The presence of small-sized shrinkage cavities on the upper ends of the ingots (Figure 3) was recorded, which is predetermined by the fact that after the end of the melting, the shrinkage operation was not performed.

Macrostructure is coarse-crystalline, dense, homogeneous, there are no defects of technological origin (Figure 4). The size of the cast grain was 1.8–2.5 mm. The angle of inclination of columnar crystals to the ingot axis is 40–45° (Figure 4, *a*), which is typical for electroslag ingots produced on the optimal surfacing rate.
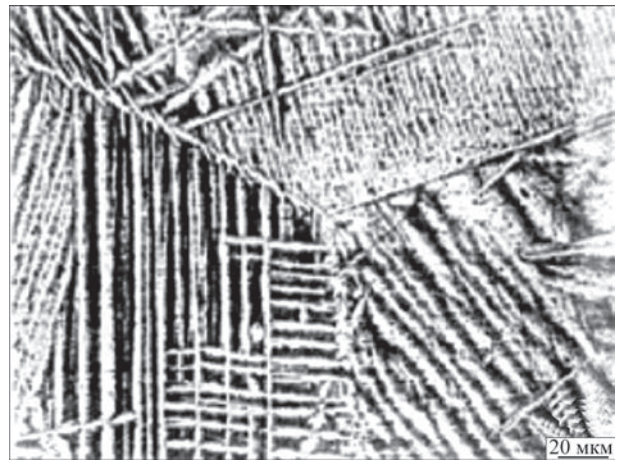

Figure 5. Microstructure of electroslag ingot of titanium

Microstructure (Figure 5) is typical of the cast titanium, i.e. transformed β-grain size from 140 to 175 μm consisted of α-plates.

In the study of the mechanical properties of electroslag titanium, it was established that the characteristics of strength σ_t and $\sigma_{0.2}$ is higher by 1.7 and 1.8 times respectively, than in commercial VT1-L titanium (Table 1). However, in terms of ductility, electroslag titanium is inferior. To increase strength, in α-alloys, TL-3 and VT5-L (σ_t and $\sigma_{0.2}$), alloying with aluminium is used (4.1–6.2 %), however, at the same time, their ductility is reduced (δ and γ). Comparing the mechanical properties of experimental titanium with the mechanical properties of TL-3 and VT5-L alloys, we can conclude that their difference is insignificant.

The lower characteristics of the ductility of the experimental ingots are determined not only by an increased content of oxygen and nitrogen, but also by a coarse-crystalline structure of cast titanium (Figure 4). For our conditions, it is possible to reduce the size of cast grain in ingots in the following way:
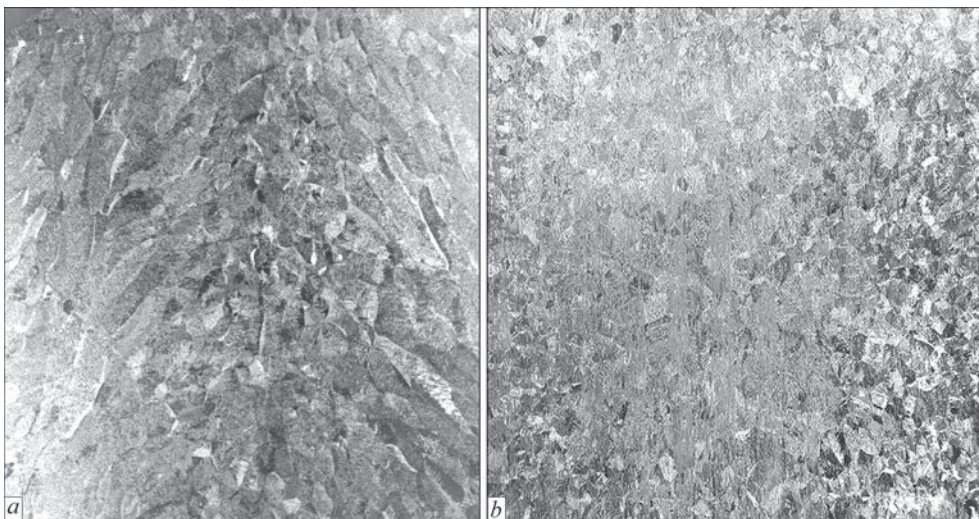

Figure 4. Macrostructure of electroslag ingots of titanium with 90×90 mm cross-section: *a* — longitudinal, ingot centre; *b* — transverse, 1/2 height of the ingot

Table 1. Mechanical properties of cast electroslag titanium, commercial VT1-L titanium and α-alloys TL-3, VT5-L and the quantity of impurities in them

Alloy	Mechanical properties				Quantity of impurities, %					
	σ_t, MPa	$\sigma_{0.2}$, MPa	δ, %	ψ, %	O_2	N_2	H_2	C	Fe	Si
Experimental titanium after annealing	590	560	7.5	13.5	0.25	0.058	0.0016	0.12	0.28	0.10
VT1-L* (commercial alloy)	<343	<297	<10.0	<20.0	<0.20	<0.05	<0.015	<0.15	<0.30	<0.15
TL-3* (Ti + 4.5 % Al)	<588	<539	<8	<16	<0.15	–"–	–"–	–"–	–"–	–"–
VT5-L* (Ti + 6.2 % Al)	<586	<627	<6	<14	<0.20	–"–	–"–	<0.20	<0.35	<0.20
*According to [19].										

● adjust the melting mode (current, voltage, deposition rate, amount of flux) to reduce the depth of the metal pool and increase the crystallization rate;

● modify the ingot by boron, lanthanum or yttrium [22–24].

It is also advisable to provide more effective protection against oxygen and nitrogen of air of a heated part of the consumable electrode and the surface of the slag pool. The application of these measures alone or in complex should significantly improve the ductility of the cast electroslag titanium.

In the study of technological properties, it was established that electroslag titanium is well subjected to mechanical treatment by cutting. No significant difference in cutting treatment was detected compared to VT1-L titanium. This was evidenced by both the nature of cutting (small twisted chips), as well as producing the required class of surface roughness and configuration of technological samples (Figure 6).

The appearance of the welded joint of the specimens produced from electroslag ingots is shown in Figure 7, *a*.

It was found that the formation of welds and the joint itself occurred normally, despite a somewhat increased oxygen and nitrogen content in the specimens, in the fusion area no pores were detected. When studying the welded joint macrostructure, its structural uniformity should be noted. Therefore, in the whole joint, the structure of cast titanium (Figure 7, *b*) is inherent. The strength characteristics of the weld are slightly lower than those of the base metal (electroslag cast titanium) and the ductility is higher (Table 2). The fracture of welded joint in the static tension test occurred over the weld, which is predetermined by the higher purity of the filler wire compared to the base metal. Therefore, in welding of cast commercial electroslag titanium a homogeneous and equal strength joint can be produced if alloyed filled wires, such as OT4sv or OT4-1sv are used. The spots on the chalk coating did not protrude, which evidenced to the tightness of the weld. This indicates that cast electroslag titanium can be used in sealed products.

One of the main types of titanium and titanium alloys is pressure treatment. The variety of technologies and methods of pressure treatment allow receiving a wide nomenclature of titanium semi-finished products for industrial needs. Electroslag ingots of titanium have a slightly increased oxygen and nitrogen content and low ductility characteristics. This can impair the deformation capacity of cast electroslag titanium. Therefore, it became necessary to investigate it.

In the process of hot forging, in the manufactured specimens (Figure 2, *b*), technological difficulties that would require special modes and additional techno-
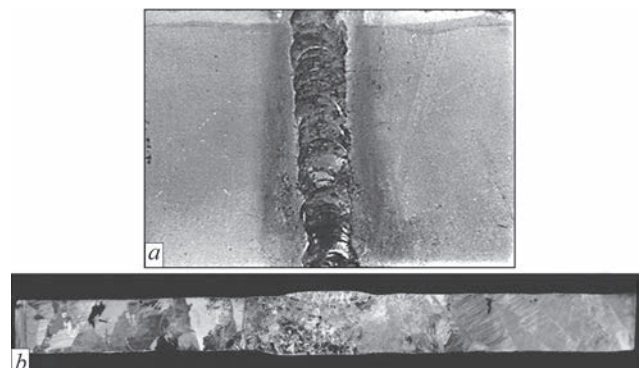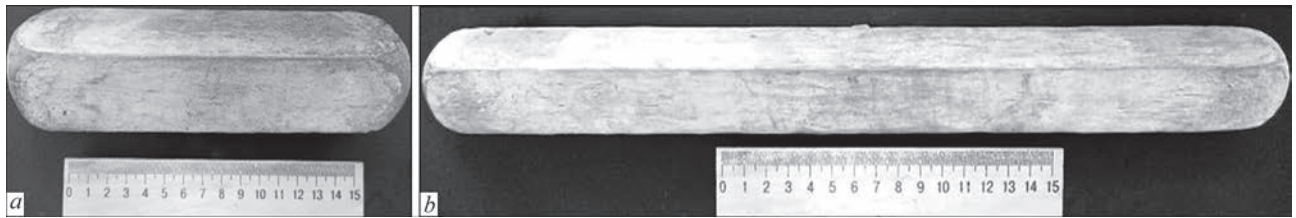

Figure 6. Parts of electroslag titanium after mechanical cutting treatment, ×0.5

Figure 7. Welded specimen from electroslag titanium, ×1: *a* — appearance; *b* — macrostructure

Table 2. Mechanical properties of welded joint of cast electroslag titanium

Specimen	σ_t, MPa	$\sigma_{0.2}$, MPa	δ, %	ψ, %	*HB*
Base metal	590	560	7.5	13.5	224
Weld metal	556	530	8.9	15.8	218

Figure 8. Appearance of deformed titanium semi-finished products with varying degrees of deformation, %: *a* — 45; *b* — 90

logical measures, were not revealed. The produced two semi-finished products, the appearance of which is shown in Figure 8. No surface cracks and other surface defects were detected by outer inspection. During ultrasonic testing of deformed semi-finished products inner defects were also not found.

Thus, in the course of carried out works on the determination of technological properties, it is shown that the produced titanium is well subjected to deformation treatment (hot forging), cutting treatment and have a good weldability.

The further studies will be aimed at developing and using design and technical means for improvement of titanium protection against interaction with air, improving the process of melting in order to improve the ductility of titanium, study of influence of hot deformation of ingots on the structure and properties of produced titanium semi-products.

CONCLUSIONS

1. While studying the structure of the produced ingots, it was established: macrostructure is coarse-crystalline, dense, homogeneous, defects are absent. The angle of inclination of columnar crystals to the ingot axis was 40–45°, the size of the grains was 1.8–2.5 mm; microstructure represents transformed β-grains with the size from 140 to 175 μm consisting of α-plates.

2. When comparing the mechanical properties of titanium of electroslag ingots with similar characteristics of the most common grades of unalloyed cast titanium, it was found out: the characteristics of the strength of titanium of electroslag ingots ($\sigma_t = 610$ MPa, $\sigma_{0.2} = 580$ MPa) are higher by 70 % than those of unalloyed VT1-L titanium; a decrease in ductility in the experimental titanium is explained by an increased content of oxygen and nitrogen, as well as a large crystalline structure; the difference in the mechanical properties of the electroslag titanium and α-alloys TL-3 and VT5-L is insignificant.

3. Investigations of technological properties of titanium of electroslag ingots proved its good cutting treatment and weldability.

4. The fundamental possibility of pressure treatment (hot forging) of titanium of electroslag ingot of 85 mm diameter with the degrees of deforming of 45 and 90 % was established.

REFERENCES

1. Kolobov, G.A. (2013) Recycling of titanium and titanium alloy wastes. *Novi Materialy i Tehnologii v Metalurgii ta Mashynobuduvanni,* **1**, 138–140 [in Russian].

2. Garmata, V.A., Petrunko, A.N., Galitsky, N.V., Olesov, Yu.V. (1983) *Titanium: Properties, raw materials, physical and chemical bases and methods for the preparation.* Moscow, Metallurgiya [in Russian].

3. https://www.retechsystemsllc.com

4. https://www.ald-vt.com

5. Paton, B.E., Akhonin, S.V., Berezos, V.A. (2018) Development of technologies of electron beam melting of metals at the E.O. Paton Welding Institute of the NAS of Ukraine. *Sovrem. Elektrometal.,* **4**, 19–35 [in Russian]. DOI: http://dx.doi.org/10.15407/sem2018.04.01

6. Akhonin, S.V., Kruglenko, M.P., Kostenko, V.I. (2010) Removal of refractory inclusions from titanium in electron beam melting by the precipitation mechanism. *Advances in Electrometallurgy,* **4**, 232–236.

7. Paton, B.E., Trigub, N.P., Akhonin, S.V., Zhuk, G.V. (2006) *Electron beam melting of titanium*. Kyiv, Naukova Dumka [in Ukrainian].

8. Paton, B.E., Trigub, N.P., Akhonin, S.V. (2008) *Electron beam melting of refractory and high-reactive metals*. Kyiv, Naukova Dumka [in Russian].

9. Kalinyuk, A.N., Derecha, O.Ya., Telin, V.V. et al. (2018) Peculiarities of production of slab-type cast billets of VT1-0 and GRADE 2 types of low-grade spongy titanium. *Sovrem. Elektrometal.,* **3**, 20–26 [in Russian]. DOI: https://doi.org/10.15407/sem2018.03.03

10. Ryabtsev, A.D., Troyansky, A.A. (2001) Production of ingots of titanium, chromium and alloys on their base in chamber electroslag furnaces using "active" metal containing fluxes. *Problemy Spets. Elektrometallurgii,* **4**, 6–9 [in Russian].

11. Protokovilov, I.V., Nazarchuk, A.T., Petrov, D.A., Porokhonko, V.B. (2018) Technological and metallurgical peculiarities of melting the titanium alloy ingots in chamber-type electroslag furnaces. *Sovrem. Elektrometal.,* **2**, 45–50 [in Russian]. DOI: https://doi.org/10.15407/sem2018.02.06

12. Bilonik, D.I., Ovchynnykov, O.V., Bilonik, I.M. et al. (2022) Electroslag melting in an open mould of ingots from sheet scrap wastes of titanium VT1-0. *Suchasna Elektrometal.,* **1**, 34–39 [in Ukrainian].

13. Bogomolova, N.A. (1978) *Practical metallography.* Moscow, Vysshaya Shkola [in Russian].

14. (2019) DSTU ISO 6892-1:2019. *Metallic materials. Tensile testing.* Pt 1. Method of test at room temperature [in Ukrainian].

15. (1967) GOST 6996–66. *Welded joints. Methods of determination of mechanical properties* [in Russian].

16. Bibikov, E.L., Glazunov, S.G., Neustruyev, A.A. et al. (1983) *Titanium alloys. Production of shaped castings from titanium alloys.* Moscow, Metallurgiya [in Russian].

17. Ovchynnykov, O.V., Kapustian, O.E. (2020) Technology for smelting zirconium alloy ingots by vacuum arc remelting with a non-consumable electrode in a skull furnace. *Suchasna Elektrometal.,* **4**, 32–38 [in Ukrainian]. DOI: https://doi.org/10.37434/sem2020.04.06

18. Dreval, A.E., Skorokhodov, E.A., Ageev, A.V. (2005) *Guick reference guide of metalworker.* Moscow, Mashinostroenie [in Russian].

19. Glazunov, S.G., Vazhenin, S.F., Zyukov-Batyrev, G.L., Ratner, Ya.L. (1975) *Application of titanium in national economy.* Kyiv, Tekhnika [in Russian].

20. Paton, B.E. (1974) *Technology of fusion electric welding of metals and alloys.* Moscow, Mashinostroenie [in Russian].

21. Nikolsky, L.A., Figlin, S.Z., Bojtsev, V.V. (1975) *Hot stamping and pressing of titanium alloys.* Moscow, Mashinostroenie [in Russian].

22. Samsonov, G.V., Kashchuk, V.A., Cherkashin, A.I. (1970) Effect of transition metals on the grain size of titanium. *Metallovedenie i Termich. Obrabotka Metallov*, **11**, 30–32 [in Russian].

23. Grigorenko, G.M., Akhonin, S.V., Loboda, P.I. et al. (2016) Structure and properties of titanium alloy doped with boron, produced by the method of electron beam remelting. *Sovrem. Elektrometal.,* **1**, 21–25 [in Russian]. DOI: https://doi.org/10.15407/sem2016.01.03

24. Goltvyanchuk, V.S., Bankovskyi, O.B., Tsyvirko, E.I. (2009) Modifying titanium-aluminium cast alloys by boron. *Novi Materialy i Tehnologii v Metalurgii ta Mashynobuduvanni*, **1**, 86–88 [in Ukrainian].

ORCID

D.I. Bilonyk: 0000-0003-3274-0604,
O.Ye. Kapustyan: 0000-0002-8979-8076,
I.A. Ovchynnykova: 0000-0002-4035-129X,
I.M. Bilonyk: 0000-0002-3873-5307,
G.M. Laptieva 0000-0003-4475-2354

CONFLICT OF INTEREST

The Authors declare no conflict of interest

CORRESPONDING AUTHOR

O.Ye. Kapustyan
National University "Zaporizka politekhnika"
64 Zhukovskogo Str., 69063, Zaporizhzhya, Ukraine.
E-mail: aek@zntu.edu.ua

SUGGESTED CITATION

JOURNAL HOME PAGE

https://patonpublishinghouse.com/eng/journals/tpwj

PRODUCTION, PROPERTIES AND PROSPECTS OF APPLICATION OF MODERN MAGNESIUM ALLOYS

V.A. Kostin, Iu.V. Falchenko, A.L. Puzrin, A.O. Makhnenko

E.O. Paton Electric Welding Institute of the NASU
11 Kazymyr Malevych Str., 03150, Kyiv, Ukraine

ABSTRACT

A literature review of the current state of magnesium alloy production technology is given, alloy properties and the influence of alloying elements on them are analyzed, microstructure and the main phases forming in the cast and wrought magnesium alloys are determined, a classification of modern magnesium alloys of foreign production is presented, further paths of their development are outlined, and problems in magnesium alloy application are defined. Magnesium alloying by other elements (Al, Mn, Zn, Si, Re, etc.) or strong nanoparticles allows significant improvement of its existing properties so as to expand its scope of application. Current problems in magnesium alloy application (flammability, combustibility, surface durability, bio-solubility, corrosion resistance, weldability) are solved by alloying, controlling the chemical and structural-phase composition, application of the respective modes of thermomechanical treatment and surface hardening.

KEYWORDS: electrolysis, metallothermic reduction, Bunsen and Pidgeon processes, cast and wrought magnesium alloys, corrosion, biocompatibility, biodegradation

INTRODUCTION

It is impossible to imagine the progress of modern industry without development and application of new structural materials and, primarily, magnesium alloys. Magnesium and its alloys are structural materials, having a unique complex of mechanical, physical and service properties, which allows their application in advanced areas of modern manufacturing — aircraft and space industries, power engineering, defense industry, medicine and electronics [1–3].

Magnesium as an alkaline-earth metal, has a shiny or silvery-white appearance, and high reactivity, and it is never found in a free state [4, 5]. Easy availability of magnesium ores (brucite — 69.1 % MgO, forsterite — 57.3 % MgO, magnesite — 47.8 % MgO, etc.) and unique technologies of producing and restoration ensured a wide application of this metal.

Magnesium alloys are used to produce cases of instruments, pumps, torches and cabin doors. Most of the helicopter fuselages, manufactured by Sikorsky Aircraft (Lockheed Martin Company, USA), are almost completely made from magnesium alloys. In rocket engineering they are used to produce the bodies of rockets, fairing, stabilizers, and fuel tanks, as magnesium alloys do not have enough time to overheat in short flight, due to a high heat capacity (2.5 times higher than that of steel), despite the low melting temperature (650–680 °C). Magnesium alloys form the basis of such structures that allows a significant reduction of the rocket weight by 20–30 % and increase flight range, respectively.

An important industry, where magnesium alloys are used, is nuclear engineering. Owing to their ability to absorb thermal neurons, no interaction with uranium and good heat conductivity, magnesium alloys are used to manufacture shells of heat generating elements in nuclear reactors.

Magnesium alloys are widely used in production of household and sporting goods, and office equipment [6].

Magnesium and its alloys play an important role in organic chemistry and pharmaceutics [7]. Deformable magnesium alloys are used with success in structural elements of flying vehicles (aircraft, rockets, shells, etc.) that ensures reduction of product weight and improves their flight characteristics.

Owing to its excellent biological properties, particularly its biodegradability in vivo, magnesium is a promising biomaterial [8] for treatment and prosthetics and at surgical intervention.

The objective of this work is to analyze and generalize the metallurgical features of magnesium alloy production, establish the influence of the main alloying elements and microstructural components on their structural properties and determine the main problems and further application prospects.

METALLURGY OF MAGNESIUM ALLOY PRODUCTION

There are two main methods of magnesium production: electrolysis of molten anhydrous magnesium chloride and metallothermic restoration of magnesium oxide by ferrosilicium [9]. Typical processes using electrolytic and thermal methods are illustrated in Figure 1.
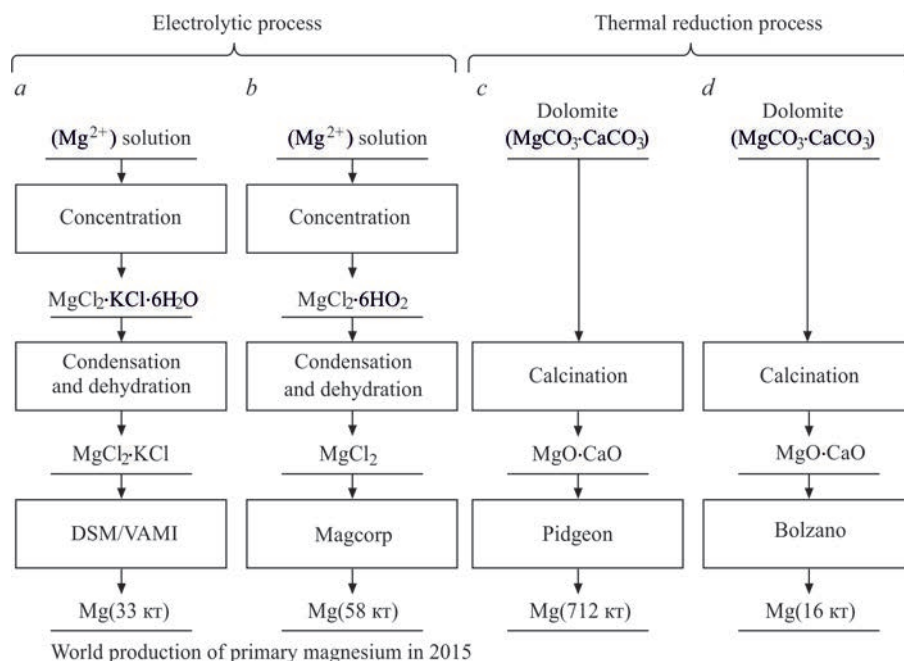
Figure 1. Block-diagram of the processes of primary metallic magnesium production: *a* — DSM/VAMI; *b* — Magcorp; *c* — Pidjeon

In the process of magnesium chloride electrolysis, first the hydrometallurgical preparation of the initial raw material (anhydrous magnesium chloride) is performed with its further feeding directly through the electrolyzers.

In his time, R. Bunsen improved the Faraday process of metallic manganese production to achieve continuous separation of chlorine and magnesium. Prevention of chlorine and magnesium recombination was critically important for success, as anhydrous magnesium chloride is hygroscopic, which may lead to formation of undesirable oxides and oxychlorides during direct dehydration [9]. Production of anhydrous magnesium chloride with a minimal quantity of oxychlorides remains to be a technology problem nowadays [10]. Scheme of Bunsen electrolytic process is shown in Figure 1 [11].

The second method of metallic magnesium production is thermal reduction. Unlike electrolysis, intensive heating during thermal reduction eliminates the need for complex preparation of the initial material [12]. The thermal process proceeds at higher temperatures (above 1200 °C) by metallothermic reduction reaction, in which silicon and/or aluminium remove magnesium in the vapour form from the oxide. Magnesium oxide is usually supplied in the form of calcined dolomite (MgO·CaO), sometimes enriched in calcined magnesite (MgO). The main reaction of producing magnesite is as follows:

$$2CaO(s) + 2MgO(s) + Si(s) \rightarrow 2Mg(g) + Ca_2SiO_4(s).$$
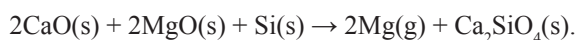
This reaction is highly endothermic and it runs in the periodic mode. Production processes run under vacuum at a lower temperature, so as to limit the

damage to the structure materials and stop unwanted side reactions in gas system.

There exist several variants of the thermal process. The three main thermal processes are Pidjeon process, using a retort with external heating; Magnetherm process — electric resistance heating using an electrode; Bolzano process, where the layer of briquettes consists of ferrosilicium and lime, and the fine fractions react in the furnace using internal electric heating.

In the Pidjeon process dolomite and ferrosilicium are formed into briquettes using a retort with external heating to produce magnesium vapours. Magnetherm process calcinates a mixture of dolomite, ferrosilicium and alumina, in order to produce the same byproduct. Magnesium vapours, produced by both the methods, are cooled and condensed separately before extraction. Nowadays, Pidjeon process is the most widely used one, due to its ability to produce high purity magnesium and a large quantity of its raw material — dolomite [13].

Application of vacuum is a common feature for the above thermal processes and metallic magnesium is condensed from the vapour phase. Magnetherm process is the only one, where the waste products are removed from the furnace as slag.

The main advantage of thermal processes over the electrolytic ones consists in that the main source of magnesium is dolomite, which requires simple calcination, unlike complex cleaning, which is required by the electrolytic method for production of anhydrous magnesium chloride.

On the other hand, the main disadvantages of the thermal processes include a relatively high cost of ferrosilicium reducing agents, and in particular, alu-
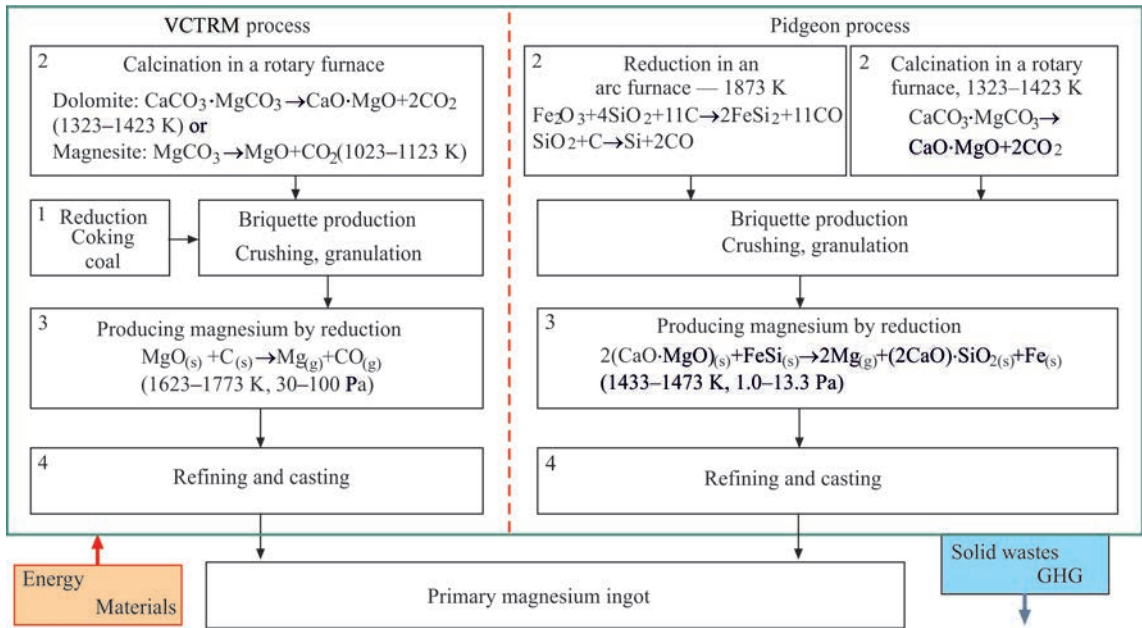
Figure 2. Schematic representation of working stages of Pidgeon and VCTRM processes of magnesium production

minium, and periodic operation, required because of vacuum, causing lower productivity and leading to air ingress, resulting in magnesium loss.

CARBOTHERMAL REDUCTION AS A NEW PRODUCTION TECHNOLOGY

The modern Pidjeon technological process is known by its complex control and high operational costs. Moreover, it consumes a tremendous amount of energy. It necessitated a search for more efficient and sustainable production technologies. An altenative production method is vacuum carbothermal reduction of magnesium (VCTRM) process, when magnesium reacts with carbon with formation of magnesium and carbon monoxide vapour [14] (Figure 2).

Despite the fact that this production process has passed large-scale production trials in the middle of the XX century, it attracted more attention only in the last decades, as carbon is a less expensive reducing agent than ferrosilicium is. It is readily available and in case of success the total production cost will be much lower than with Pidgeon method [11]. Therefore, condensation of magnesium vapors and their separation from carbon monoxide remains a serious problem. Moreover, the researchers' interest to solar carbothermal reduction is growing (Figure 3) [15]. Investigations showed that this process uses less energy and releases less hydrocarbon gas, compared to Pidgeon method (5.31 against 15.9 kg CO_2).

SECONDARY PRODUCTION OF MAGNESIUM

With increase of magnesium application all over the world, greater volumes of magnesium wastes are to be anticipated. Magnesium is readily recycled and its
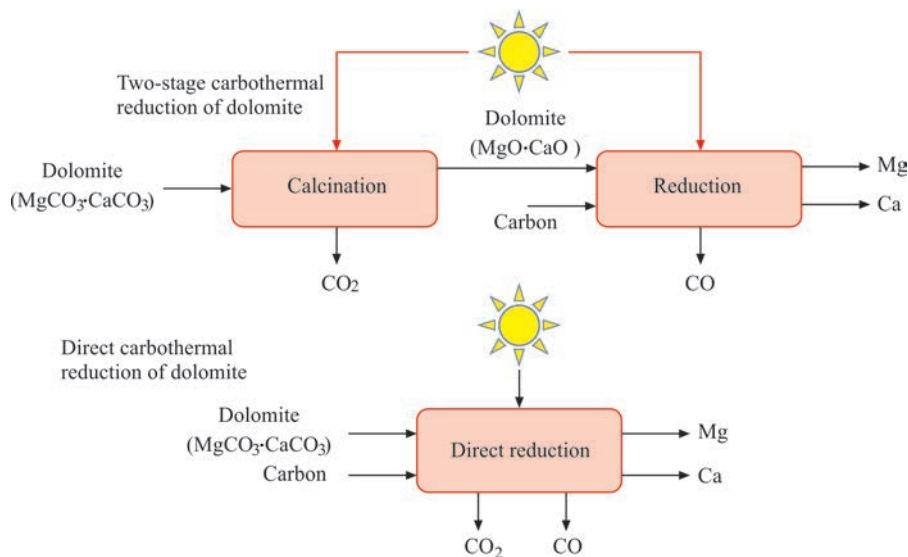

Figure 3. Block-diagram of the processes of solar carbothermal reduction of magnesium

recycling can become an additional supply source for the main production. Nowadays there exist both the flux and fluxless technologies of magnesium recycling. Recycled magnesium preserves the same chemical, physical and mechanical characteristics, as the initial material had. Moreover, magnesium recycling consumes only 5 % of the energy, required for its production. Use of secondary magnesium also reduces carbon emissions and saves material in a renewable economy. Magnesium alloys, however, can be easily recycled only in the case, if their composition is stable and does not contain any impurities [16]. It explains why most of the recycled magnesium is obtained from the wastes of die-cast magnesium alloys, when almost 30 % of magnesium is removed during the production process. To enable real progress of magnesium recycling, it is necessary to develop a recycling process, which would be commercially viable and environmentally friendly. At present, magnesium recycling methods include distillation, salt-free or salt-based remelting, solid-state recycling and direct conversion.

3D PRINTING
AS A NEW PRODUCTION PROCESS

Additive manufacturing or 3D printing is a new method of producing magnesium alloys. In general, the interest to 3D printing of metals grows due to its ability to adjust and optimize the composition of each alloy, in keeping with its application, and obtain the best possible result. Printing alloys in a more complex configuration to suit the anatomic geometry of patient tissues, so as to promote an accelerated growth of the cells, proliferation and regeneration of bones, can be an example [17].

Another example can be printing of complex-shaped parts from magnesium alloys. It could not be achieved earlier using traditional production, which restricted its development. More over, unlike the traditional production methods, part manufacturing using additive technologies can also greatly reduce the technical complexity and cost of individual production, while increasing its effectiveness.

Producing magnesium alloys by additive technologies is promising. However, studies on how magnesium alloys can be printed in 3D printer are rather limited, as it is known to be related to several problems [18]. First, magnesium is a chemically reactive and combustible material. It has a low evaporation temperature that complicates mixing and printing of magnesium alloys of a desirable composition, density, strength, biocompatibility and corrosive behaviour. Preparation of the initial material is dangerous, as magnesium powders have a high explosive tendency. At present, two typical methods of additive manufacturing to produce parts

from magnesium alloys are wire arc additive manufacture (WAAM) and selective laser melting (SLM), known as powder layer melting [18].

ALLOYING, STRUCTURE
AND PROPERTIES OF MAGNESIUM ALLOYS

Magnesium is the lightest engineering metal. Pure magnesium has a very low density (1.74 g/cm³) and it demonstrates a higher strength-to-weight ratio and better ductility and castability than aluminium or steel. Compared to other metals and polymer materials, magnesium is not toxic and it has better values of heat and electric conductivity, vibration and shock absorption, cushioning capacity, as well as good workability, and it can be formed by any established method. Its disadvantage, however, is its corrosion susceptibility. It quickly corrodes under two conditions: when the alloy consists of specific metal impurities, or under the impact of aggressive kinds of electrolyte. Technologies of coating deposition (electrochemical, conversion, anodizing) were developed and used to overcome this feature of magnesium alloys [19]. Pure magnesium (99.8 %) is ideally suitable for metallurgical and chemical purposes, but it has to be alloyed for application in engineering structures, so as to enhance its properties without damage for the key characteristics [6].

The best production method is melting and casting magnesium alloys in an inert vacuum atmosphere, as magnesium solidifies better than other metals do. More over, a chemically inactive environment can prevent any contamination by reactive gases. Solid solution and dispersion strengthening by another phase is as a rule used to strengthen the magnesium alloys [20]. The alloy components and their chemical composition can influence improvement of magnesium alloy physical properties.

ALLOYING ELEMENTS

Aluminium and zinc are the most common and prevailing alloying elements. Both aluminium and zinc are sufficiently cost-effective and readily soluble in magnesium. Aluminium can be used to improve the strength and hardness and to widen the alloy melting range, while at the same time lowering its corrosion susceptibility. The respective range of strength and ductility can be achieved by changing the aluminium content in the alloy [21]. When applied together with zinc, it can further increase the room temperature strength of the alloy.

Zinc addition alone can increase the magnesium alloy castability and improve their dimensional stability. When zinc together with magnesium alloys is mixed with such impurities as nickel and iron, it can
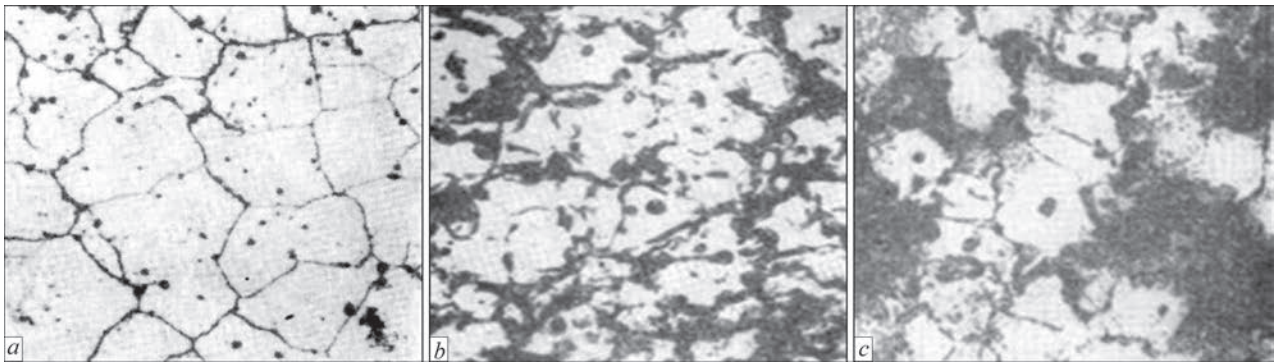
Figure 4. Microstructure (×100) of cast magnesium alloy ML5 (9 % Al; 0.5 % Mn; 0.8 % Zn) after different heat treatment modes: *a* — in the cast state; *b* — after quenching; *c* — after quenching + aging

increase the alloy corrosion resistance. Zinc does not form any independent phases with the alloying component — manganese. An γ-phase ($Mg_{17}Al_{12}$) forms in MA2-1 alloy. This phase precipitates at the alloy recrystallization as a result of heat treatment or welding, as well as during decomposition of the oversaturated solid solution, becoming part of a pseudoeutectic. The pseudoeutectic is mostly located along the grain boundaries. Primary $Mg_{17}Al_{12}$ phase is a strengthening phase. It is preserved in the alloy after deformation and welding. Some authors established that $Mg_{17}Al_{12}$ γ-phase has the ability of enrichment in zinc and additionally in aluminium, forming $Mg_{17}(Al, Zn)_{12}$ intermetallic phase, which is represented by coarse precipitates.

Excessively high concentrations of aluminium lead to ductility lowering and impair the alloy deformability in the hot and cold states. Zinc improves not only strength, but also relative elongation of the alloys with aluminium. However, at more than 1.5 % Zn content, pressure workability of alloys of Mg–Al–Zn system deteriorates. Manganese is added to these alloys predominantly to improve the corrosion resistance.

Investigations conducted over the recent years showed that magnesium alloy doping by rare-earth metals (REM) allows an essential improvement of their strength properties.

Magnesium alloys doped by REM of cerium (La, Ce, Pr, Nd, Pm, Sm, Eu) and yttrium (Sc, Y, Gd, Tb, Dy, Ho, Er, Tm, Yb) groups have their advantages and disadvantages, if compared by their properties. In the alloys with metals of the cerium group, lower strength values are achieved, but shorter aging time is required to obtain maximum strengthening. In alloys with metals of yttrium group a higher level of strengthening is achieved, but after a long-time soaking at aging and a higher content of expensive rate-earth metals. In a number of cases, simultaneous application of REM of both the groups is rational for doping the magnesium alloys.

Magnesium alloy microstructure in the initial state consists predominantly of equiaxed grains of 100 to 1000 μm size in the inner regions and on the boundaries, where dispersed and dispersive strengthening phases are located. These phases can have an important role in the magnesium alloy properties after conducting the respective heat treatment (Figure 4).

The dimensions and distribution of the phases forming during casting or during the subsequent stages of heat or thermomechanical treatment, depend on the respective heat treatment parameters. Dispersed particles counteract grain growth according to Zenner–Straw model, in which the grain size grows with reduction of the size of particles and increase of their volume fraction. The effect of grain boundary fixation by Zr dispersoids and without them in the magnesium alloy is given in Figure 5. In magnesium alloys without aluminium application, zirconium is often used as a dispersing element, while in alloys of Mg–Al system with aluminium, it is rational to use magnesium with formation of AlMn intermetallics. Zr additives are also effective as grain refiners during casting that enables production of fine-grained magnesium alloys.

A considerable part of magnesium alloy products is produced by the extrusion method. As a result, such magnesium alloys differ by their microstructure that is related to the processes of grain recrystallization on the second phase clusters, extruded at higher temperatures (Figure 6).

The structural-phase composition of magnesium alloys is mainly determined by their alloying system. There exist a number of solidification phases forming in the equilibrium state with magnesium solid solution, namely $Mg_{17}Al_{12}$ (Mg–Al system), Mg_2Ca (Mg–Ca system), Mg_2Sn (Mg–Sn system), Mg_4Ag (Mg–Ag system), Al_2Re and Al_2Ca (Mg–Al–Ca–Re system), $MgCu_2$ (Mg–Cu–Zn system), $Mg_6Ca_2Zn_3$ (Mg–Ca–Zn system), X_MgReZn (Mg–Gd–Zn and Mg–Y–Zn system), PHI_AlMgZn (Mg–Al–Zn system). The following metastable phases can also form in the magnesium alloys: $MgZn_2$ (Mg–Zn system) and Mg_7Re (Mg–Re system).
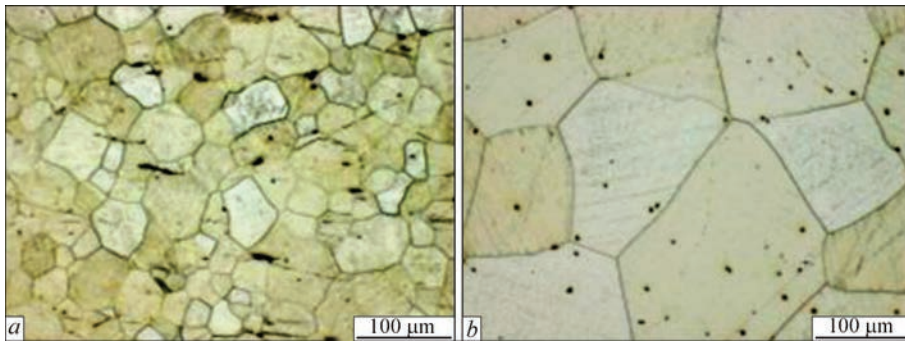
Figure 5. Microstructure of magnesium alloy with REM, after forging and heat treatment: *a* — with zirconium (~ 0.4 wt.%); *b* — without zirconium

A feature of magnesium alloys is a lower rate of diffusion of the majority of the components in the magnesium solid solution. Low diffusion rates promote development of dendrite liquation, require a long soaking time at heating, facilitate solid solution fixation at hardening, but complicate decomposition of oversaturated solid solutions at aging.

Magnesium alloys have a high ductility in the hot state, and deform well when heated. For wrought alloys diffusion annealing is usually combined with heating for pressure treatment. Magnesium alloys are readily cut, ground and polished.

The disadvantages of magnesium alloys are poor casting properties, proneness to gas saturation, oxidation and ignition during casting. Special fluxes are used to prevent defect formation at casting and welding, and small calcium additives (up to 0.2 %) are applied to reduce porosity, and beryllium additives (0.02–0.05 %) — to reduce oxidizability.

Alongside the traditional alloying method, considerable progress has been made over the recent years in application of nanocomposites based on magnesium alloys, which additionally strengthen the alloys [22]. The characteristics of these alloys are affected by both the alloying components and the nanoparticles, reinforcing the alloy [23]. Increased researchers' interest in this area is associated with the fact that strengthening by nanoparticles can improve the magnesium strength and ductility without any negative consequences.

American Society for Testing Materials (ASTM) proposed a system of designations for identification

of magnesium alloys and determination of their composition (Figure 7) [24].

All the magnesium alloys are divided into two large groups, namely cast and wrought. Among the cast alloys, a group of alloys produced by die casting (AZ91, AS41, AE42) stands out. Wrought magnesium alloys are divided into those deformed by forging, rolling or extrusion.

Performed analysis of published sources showed that development of magnesium alloys gradually moved along the path of application of more complex compositions, in order to obtain specific properties, namely strength (superlight, high-strength), toughness (thermally or thermomechanically hardened), creep, thermal expansion, wear, etc. (Figure 8) [25].

Magnesium alloys with aluminium are AZ31 and AZ91. AZ31 alloy is widely used in aircraft construction due to its low mass density and good mechanical properties. At the same time, AZ91 alloy remains to be one of the most popular casting alloys owing to its high strength, excellent corrosion resistance and good castability. Mechanical properties of AZ31 and AZ91D magnesium alloys are given in Table 1.

Performed analysis of publications showed that the main problems are to be anticipated in welding cast magnesium alloys (AZ63F, ZE41F, ZK51A, ZK61A), as a result of development of dendritic liquation, chemical and structural heterogeneity in them, formation of pores and discontinuities and strengthening phase segregation (Table 2), whereas forged magne-
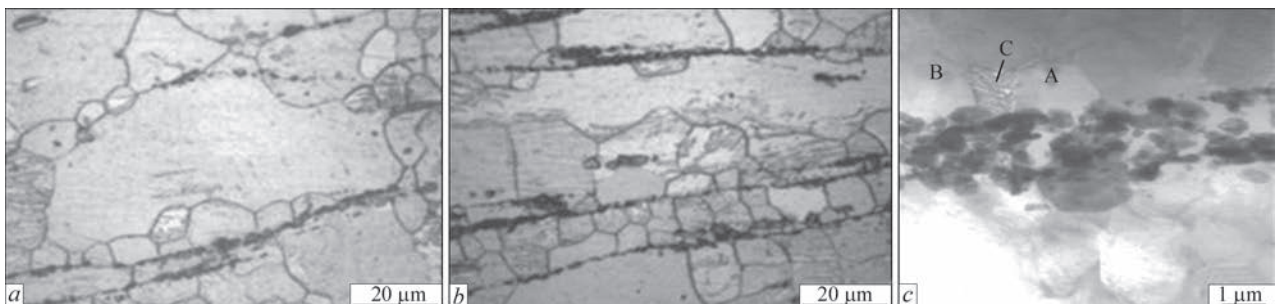

Figure 6. Microstructure of magnesium alloy AZ31 + 0.8 wt.% Sr, extruded at the temperatures of 250 (*a*), 350 °C (*b*) and recrystallization on particles of Al–Sr phases (*c*)
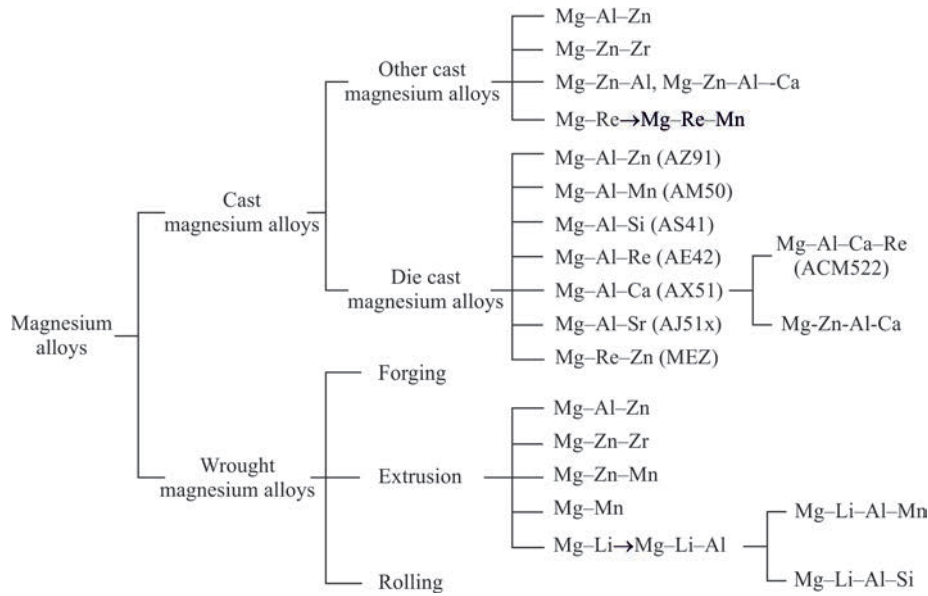
Figure 7. Classification of foreign magnesium alloys [24]
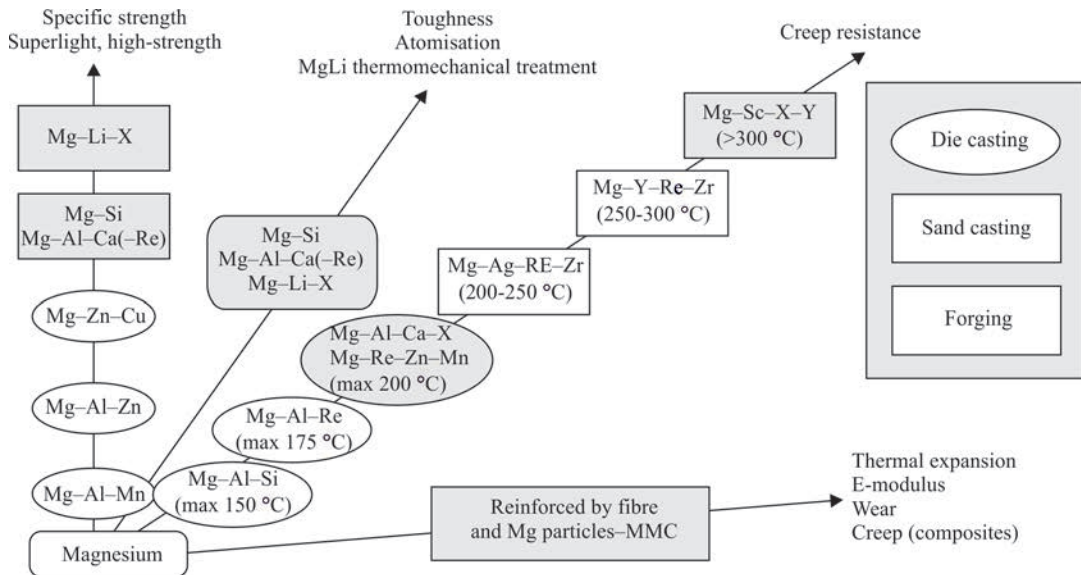

Figure 8. Directions of development of foreign magnesium alloys [25]

sium alloys (NK31A, ZE10A, ZK21A) have excellent weldability.

APPLICATION OF MAGNESIUM ALLOYS

Calculations show that application of lighter magnesium alloys instead of heavier ones (aluminium and titanium alloys or steels) can improve the aircraft fuel efficiency and reduce harmful emissions. It means considerable fuel saving and lower operating costs. Replacement of aluminium alloys by magnesium ones can en-

sure an almost 60 t weight reduction, that makes 28 % of the aircraft weight.

At the same time, limitations and critical aspects of magnesium application in modern aviation were revealed. This is predominantly related to its combustibility, surface durability and corrosion resistance.

Nowadays aluminium and its alloys still have significant advantages over magnesium and its alloys for aerospace structures. However, recent progress is applied studies of magnesium alloy flammability lead to discovery of less combustible materials that enabled

Table 1. Mechanical properties of magnesium alloys

Material/Alloy	Density, g/cm³	Compressive strength, MPa	Tensile strength, MPa	Modulus of elasticity, GPa
Magnesium	1.74	20–115	90–190	45
AZ31 (wrought)	1.78	83–97	241–260	–»–
AZ91D (cast)	1.81	160	230	–»–

Table 2. Relative weldabilly of magnesium alloys

Cast into a chill mold									
AM100	AZ63A	AZ81A	AZ91AC	AZ92A	EK41A	EZ33A	HK31A	HZ32A	OE22A
B	C	B	B	B	B	A	B	C	B

Table 2 (cont.)

Cast into a chill mold				Deformed by forging				
ZE41A	ZH62A	ZK51A	ZK61A	HK31A	HM21A	HM31A	ZE10A	ZK21A
C	C	D	D	A	A	A	A	B
Note. A — very good; B — good; C — satisfactory; D — bad.								

their wider application in passenger aircraft and cars. Increase of mechanical strength of such magnesium alloys as Elektron 21 or Elektron 675, demonstrating two times higher strength than aluminium does, will also promote their further application [26].

Although the first attempts of application of magnesium and its alloys in cars date back to the beginning of the XX century, the overall fraction of magnesium materials in the automotive industry remains to be negligible, compared to steel and aluminium. Figure 9 shows the retrospective of application of magnesium and its alloys in cars of different manufacturers during 1930–2000.

The main type of cast magnesium alloys in the automotive industry is a series of alloys, based on Mg–Al system (AZ, AM), rare-earth elements (WE43, E21) and ZK grade alloys.

Moreover, the possibility of using high-strength magnesium alloys with nanocomposites is considered for higher temperature applications, as they have excellent thermal and dimensional stability [27]. However, except for cast magnesium alloys, other alloy types, for instance, sheet wrought or extruded magnesium alloys are almost not used in modern automotive industry.

Magnesium alloys found wide application in the health care and biomedical industry [24]. Magnesium is a material naturally biocompatible with the human body. It supports physiological functions in the human body, including structural stabilization of proteins, nucleic acids, cell membranes, and it also stimulates special structural or catalytic activities of proteins or enzymes [1]. Moreover, magnesium is not toxic, does not irritate the skin and promotes tissue healing.
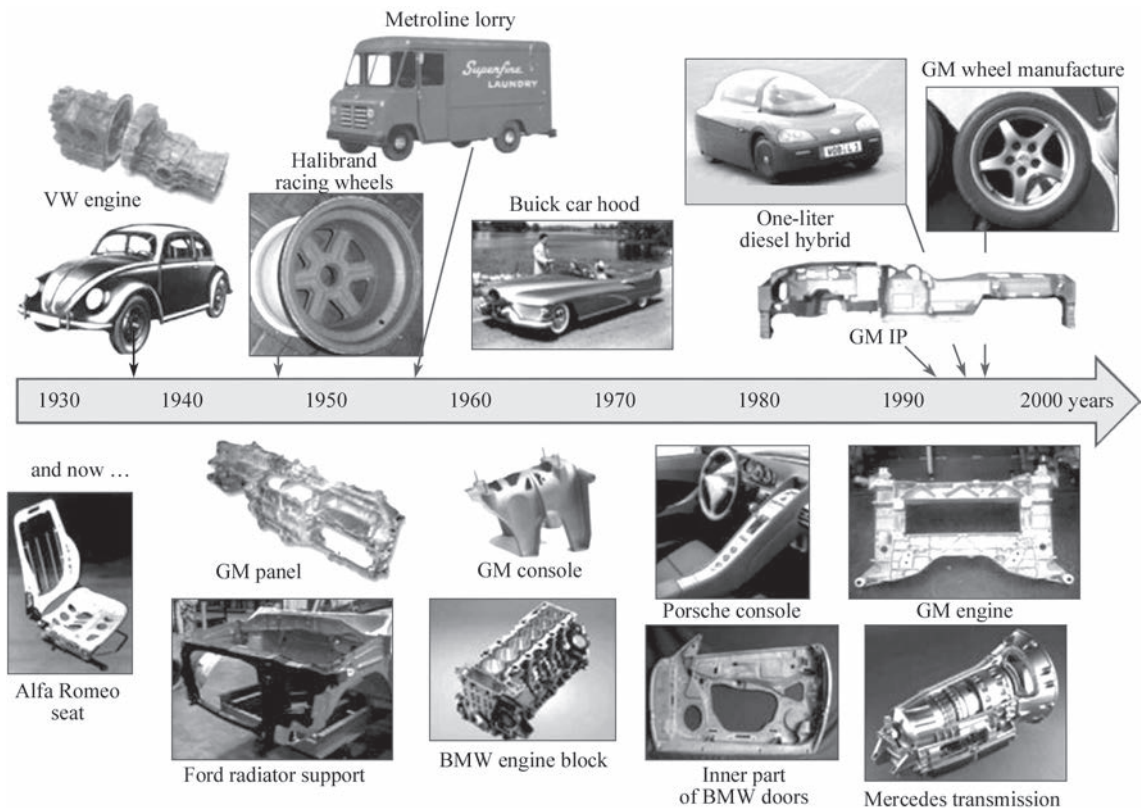

Figure 9. Retrospective of magnesium alloy application in automotive industry

Magnesium also is a bioabsorbable and bioactive material. When used as implants, magnesium alloys have a lower modulus of elasticity, than do other analogs, which is their advantage as a biomaterial. As the modulus of elasticity of magnesium is closer to the rigidity of natural bone at application, it is preferred in most cases.

Often the body requires just a temporary presence of the implant to support tissue regeneration and restoration of the impaired physical functions. Magnesium ability to biodegrade is both its greatest advantage and weakness. Magnesium quickly decomposes in a physiological environment. Such accelerated degradation can endanger the mechanical integrity and strength of the respective implants. It may also lead to undesirable reactions and can cause biotoxicity.

The disadvantages of magnesium alloy application include their wear corrosion resistance. Depending on application conditions, different kinds of corrosion can develop in the magnesium alloys, namely: galvanic, pitting, filiform, intergranular (IGC), exfoliation (EFC), crevice, stress corrosion cracking (SCC), corrosion fatigue (CF) and erosion corrosion wear [5].

Analysis of the used publications showed the key strategies for overcoming the corrosion fracture of magnesium alloys, which consist of cleaning, alloying and surface modification. These strategies use the principle of slowing down the corrosion process due to reduction of hydrogen accumulation rate and local alkalization. Despite the considerable achievements in controlling magnesium corrosion, this problem still remains urgent.

CONCLUSIONS

1. Magnesium accessibility and a unique combination of properties (low weight, specific high strength-to-weight ratio, excellent workability and castability) made it very attractive for application. Magnesium alloying by other elements (Al, Mn, Zn, Si, Re) or strong nanoparticles allowed improvement of its existing properties, so as to expand the range of its applications. These factors allowed magnesium to find its place in the aerospace, automotive, defense and nuclear industries and in medicine.

2. Existing problems in the use of magnesium alloys (flammability, combustibility, fatigue life, biosolubility, corrosion resistance, weldability) are solved by its alloying, controlling its chemical and structural-phase composition, application of the respective modes of thermomechanical treatment and surface hardening.

3. Modern methods of producing primary magnesium and its alloys are rather energy-intensive and inefficient in production, which results in expansion of investigations in the field of additive production of magnesium alloys and use of "green" power technologies. An ecologically safe process of recycling of magnesium and its alloys also is one of the variants of manufacturing the required metal products.

REFERENCES

1. Junxiu Chen, Lili Tan, Xiaoming Yu et al. (2018) Mechanical properties of magnesium alloys for medical application. *J. of Mechanical Behavior of Biomedical Materials*, **87**, 68–79.
2. Radha, R., Sreekanth, D. (2017) Insight of magnesium alloys and composites for orthopedic implant applications. *J. of Magnesium and Alloys*, 5(**3**), 286–312.
3. Yan Yang, Xiaoming Xiong, Jing Chen et al. (2021) Research advances in magnesium and magnesium alloys worldwide in 2020. *Ibid.*, 9(**3**), 705–747.
4. Dobrza´nski, L.A. (2019) The importance of magnesium and its alloys in modern technology and methods of shaping their structure and properties. *Magnesium and its Alloys.* CRC Press: Boca Raton, FL, USA, 1–28.
5. Song, G.L., Atrens, A. (1999) Corrosion mechanisms of magnesium alloys. *Adv. Eng. Mater.*, **1**, 11–33.
6. Dieringa, H.; Stjohn, D.; Prado, M.T.P.; Kainer, K. (2021) Latest developments in the field of magnesium alloys and their applications. *Front. Mater.*, 8(July), 1–3. DOI: 10.3389/fmats.2021.726297
7. Polmear, I.J. (1994) Magnesium alloys and applications. *Mater. Sci. Technol.*, **10**, 1–16.
8. Tae-Hyuk Lee, Toru H. Okabe, Jin-Young Lee et al. (2021) Development of a novel electrolytic process for producing high-purity magnesium metal from magnesium oxide using a liquid tin cathode. *J. of Magnesium and Alloys*, 9(**5**), 1644–1655.
9. (2001) U.S. Geological Survey. 01-341, Magnesium, Its Alloys and Compounds. https://pubs.usgs.gov/of/2001/of01-341/
10. Gao, F., Nie, Z.-R., Wang, Z.-H. et al. (2008) Assessing environmental impact of magnesium production using Pidgeon process in China. *Transact. Nonferrous Met. Soc. China*, **18**, 749–754.
11. Durlach, J. (2006) Overview of magnesium research: History and current trends. *New Perspectives in Magnesium Research.* Springer, London, UK, 3–10.
12. Holywell, G.C. (2005) Magnesium: The first quarter millennium. JOM, 57, 26–33.
13. Yang Tian, Lipeng Wang, Bin Yang et al. (2022) Comparative evaluation of energy and resource consumption for vacuum carbothermal reduction and Pidgeon process used in magnesium production. *J. of Magnesium and Alloys*, 10(**3**), 697–706.
14. Hamed Abedini Najafabadi, Nesrin Ozalp, Michael Epstein, Richard Davis (2020) Solar carbothermic reduction of dolomite: direct method for production of magnesium and calcium. *Industrial & Engineering Chemistry Research*, 59(**33**), 14717–14728.
15. Mendis, C.L., Singh, A. (2013) Magnesium recycling: To the grave and beyond. *JOM*, **65**, 1283–1284.
16. Karunakaran, R., Ortgies, S., Tamayol, A. et al. (2020) Additive manufacturing of magnesium alloys. *Bioact. Mater.*, **5**, 44–54.
17. Davim, J.P. (2020) *Additive and subtractive manufacturing: Emergent technologies.* De Gruyter, Berlin, Germany.
18. Kulekci, M.K. (2008) Magnesium and its alloys applications in automotive industry. *Int. J. Adv. Manuf. Technol.*, **39**, 851–865.
19. Abbott, T. (2019) Casting Technologies, Microstructure and Properties. *Magnesium and its Alloys.* CRC Press, Boca Raton, FL, USA, 29–45.
20. Fujisawa, S., Yonezu, A. (2014) Mechanical property of microstructure in die-cast magnesium alloy evaluated by

indentation testing at elevated temperature. In: *Proc. of Int. Congress on Recent Advances in Structural Integrity Analysis (Apcf/Sif-2014)*. Elsevier, Amsterdam, The Netherlands, 422–426.

21. Gupta, M., Wong, W.L.E. (2015) Magnesium-based nanocomposites. Lightweight materials of the future. *Mater. Charact*., **105**, 30–46.

22. Moosbrugger, C., Marquard, L. (2017) *Engineering properties of magnesium alloys*. ASM International, Materials Park, OH, USA.

23. Krishnan K. Sankaran, Rajiv S. Mishra (2017) *Chapt. 7. Magnesium alloys. Metallurgy and design of alloys with hierarchical microstructures*. Elsevier, 345–383.

24. Jeal, N. (2005) High-performance magnesium. *Advanced Materials & Processes*, **9**, 65–67.

25. Tekumalla, S., Gupta, M. (2020) Introductory chapter: An insight into fascinating potential of magnesium. In: *Magnesium — the wonder element for engineering/biomedical applications*. IntechOpen, London, UK.

26. Luthringer, B.J.C., Feyerabend, F., Willumeit-Römer, R. (2014) Magnesium-based implants: A mini-review. *Magnes. Res*., **27**, 142–154.

27. Zeng, R.-C., Yin, Z.-Z., Chen, X.-B., Xu, D.-K. (2018) Corrosion types of magnesium alloys. *Magnesium Alloys — Selected Issue*. IntechOpen, London, UK.

ORCID
V.A. Kostin: 0000-0002-2677-4667,
Iu.V. Falchenko: 0000-0002-3028-2964
A.L. Puzrin: 0000-0003-0625-2113,
A.O. Makhnenko: 0000-0003-2319-2976

CONFLICT OF INTEREST
The Authors declare no conflict of interest

CORRESPONDING AUTHOR
V.A. Kostin
E.O. Paton Electric Welding Institute of the NASU
11 Kazymyr Malevych Str., 03150, Kyiv, Ukraine.
E-mail: valerykkos@gmail.com

DIAGNOSTICS OF GEAR PAIR DAMAGE USING THE METHODS OF BIPERIODICALLY CORRELATED RANDOM PROCESSES. PART 2. INVESTIGATION OF VIBRATION SIGNALS OF THE WIND POWER GENERATOR GEARBOX

R.M. Yuzefovych[1,2], **I.M. Javorskyj**[1,3], **O.V. Lychak**[1], **G.R. Trokhym**[1], **M.Z. Varyvoda**[1], **P.O. Semenov**[4]

[1]G.V. Karpenko Physico-Mechanical Institute of NASU

5 Naukova Str., 79060, Lviv, Ukraine. E-mail: roman.yuzefovych@gmail.com

[2]Bydgoszcz University of Sciences and Technology.

7 Prof. S. Kaliskiego Al., 85796, Bydgoszcz, Poland

[3]Lviv Polytechnic National University

12 S. Bandery Str., 79000, Lviv, Ukraine.

[4]Odesa National Maritime University

34 I. Mechnikova Str., 65029, Odesa, Ukraine

ABSTRACT

The results of processing the vibration signals of the wind power generator gearbox are given. The model of vibration in the form of biperiodically correlated random processes (BPCRP), which describes its stochastic repeatability with two different periods, is considered. Least squares (LS) estimates of the periods of the deterministic part of the vibration signal and the temporal changes of power of its stochastic part were obtained. The amplitude spectra of deterministic oscillations and dispersion of stochastic oscillations for different degrees of gearbox damage were analyzed. The most effective indicators of defect development, which are formed on the basis of amplitude spectra, are proposed for practical use. The correlation structure of the stochastic vibration component of the wind power generator gearbox was analyzed.

KEYWORDS: wind power generator gearbox, vibration, periodical nonstationarity, deterministic oscillations, correlation function, defect development indicator

INTRODUCTION

Solution of the problems of technical diagnostics is effective using the methods of statistical analysis of vibration signals based on a theory and methods of periodically correlated random processes (PCRP) [1] and their mutual analysis [2]. One of such problems is evaluation and control of operation of elements of complex mechanical systems, detection of defects nucleated in mechanisms, search of indicators reacting on insignificant deviation of parameters of technical condition from standard. Work [3] proposes a model in form of biperiodically correlated random processes (BPCRP) for analysis of vibration of a damaged gear pair of wind power generator (WPG) gearbox where modulation interaction of deterministic oscillations of two wheels is characterized by BPCRP mathematical expectation and interaction of stochastic vibrations by BPCRP correlation function. Fourier series of the mathematical expectation and correlation function consist of harmonics of frequencies of wheels rotation, their multiples and combinations. Harmonics of coupling frequencies are the separate BPCRP harmonics of signal representation. Specific content of

harmonics of deterministic and stochastic oscillations depends on a level of defect development and place of its location.

An approach proposed in [3] was used for analysis of signals of WPG gearbox vibration using PCRP for defect diagnostics. In process of analysis of vibration signals there were determined the amplitude spectra of oscillations deterministic constituent and power of time changes of stochastic constituent was used as typical characteristics for evaluation of level of defect development. Based on the results of vibration signal processing there was proposed the most sensitive indicator for detection of WPG gearbox defects.

ANALYSIS OF REAL DATA

The results of analysis of a half-year monitoring of signals of WPG gearbox vibrations are provided with the following characteristics: number of gear teeth — 25, number of wheel teeth — 94. Duration of obtained vibration signals — 3.35 s (8192 points). Figure 1 shows the fragments of vibration signals corresponding to different stages of development of gear tooth defect. Rotation speeds of a high-speed shaft were measured using a tachometer and made respectively 1451.55, 1442.85 and 1404.75 rpm for each of failure
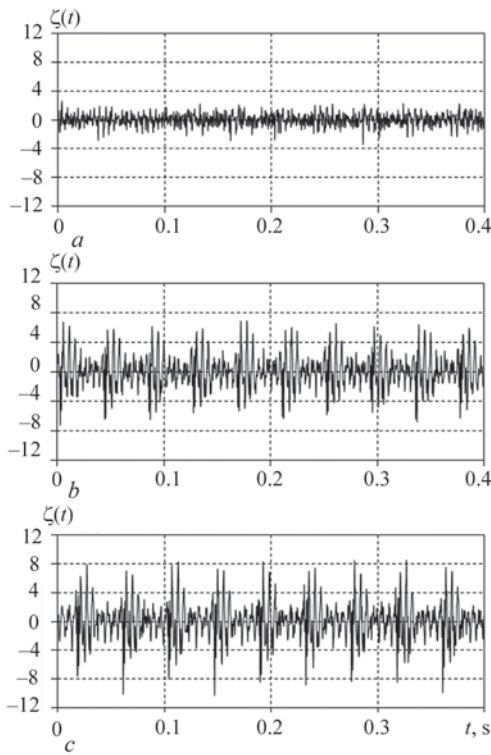
Figure 1. Fragments of realization of vibration signals for three stages of defect development of gear tooth

stages. Figure 1 shows that vibration signals for second (Figure 1, *b*) and third (Figure 1, *c*) failure stages contain clear strokes provoked by presence of developing defect and time intervals between the strokes are close to a period of shaft rotation.

Let's calculate evaluations of spectral densities of stationary approximation of signals for each of the stages using Hamming windows:

$$k(\tau) = \begin{cases} 0.54 + 0.46\cos\dfrac{\pi\tau}{\tau_p}, & |\tau| \le \tau_p, \\ 0, & |\tau| > \tau_p, \end{cases}$$

where τ_p is the point of correlogram truncation. It appears from the obtained results (Figure 2) that a spectrum of oscillation power lies in a range of 0–10 kHz

(Figure 2, *a*) and the main constituent of power spectrum lies in a range limited by 3 kHz (Figure 2, *b*).

Diagrams on Figure 2 have a comb-shape with different amplitudes and bandwidths. The evaluation value acquires peak values in the points matching with coupling frequency and frequencies multiple to it, rotation frequency of gear, multiple to it and their mutual combinations. We note the frequency bands which correspond to powerful resonances, i.e. $[f_p; 1.8f_p]$ and $[2.2f_p; 3f_p]$, where f_p is the coupling frequency. Powers of spectral constituents corresponding to wheel rotation frequency (approximately 6.4 Hz) and multiple to it are insignificant. Therefore, it is possible to assume that deterministic and stochastic modulations caused by PCRP oscillations of a shaft rotation period are also insignificant, and formally current data can be analyzed as PCRP realizations.

Let's carry out an analysis of properties of signal on frequencies less than $1.8f_p$. The evaluations of correlation function and spectral density for stationary approximation of filtered signals corresponding to three stages of gear tooth failure are given on Figures 3, 4.

Presence of undamped "tail" is a typical feature of evaluations of PCRP correlation function. It comes from a formula for stationary approximation of PCRP correlation function [3]:

$$R(\tau) = R_0(\tau) + \frac{1}{2}\sum_{k=1}^{L_1} |m_k|^2 \cos k \frac{2\pi}{P}\tau \tag{1}$$

that a undamped "tail" contains the cosine oscillations with amplitudes corresponding to power of each deterministic constituent of harmonic. In point $\tau = 0$ expression (1) determines the sum power of deterministic and stochastic oscillations. In point $\tau_r = \tau P$, where r is the natural number, for which $R_0(rP) \approx 0$, a value of power of deterministic oscillations is obtained. For three considered stages of degradation of a gear tooth the sum power of vibration signal equals $0.95G^2$, $5.84G^2$ and $7.73G^2$ and power of deterministic
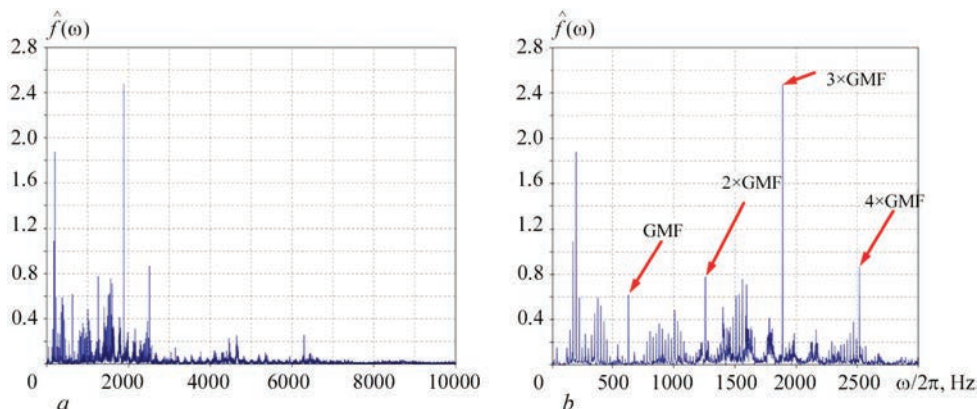

Figure 2. Evaluation of spectral density of power of vibration signal in stationary approximation for first stage: *a* — full spectrum; *b* — LF fragment of spectrum

constituent of oscillations vibration signal is $0.72G^2$, $5.12G^2$ and $6.73G^2$, respectively. Therefore, part of power of stochastic oscillations reduces with defect development. If this part on the initial stage of defect development approximately equals 30% then for the last stage it equals only 14 %.

It is noted that the undamped "tail" of correlation function has a group structure, the time interval between the separate groups is close to a period of shaft rotation. Presence of the undamped "tail" in evaluation of the correlation function results in appearance of discrete constituents in evaluation of spectral density which are presented by peaks on certain frequencies (Figure 4). Detected peaks can also be a result of a narrow band characteristic of stochastic constituents. Therefore, obtained spectra of the vibration signal complicate interpretation of the results of spectral evaluation and their quantitative analysis. For discrete evaluation of spectrum use [3]

$$\hat{f}_d(\omega) = \int\limits_{-\infty}^{\infty} f_d(\omega_1)\lambda(\omega-\omega_1)d\omega_1,$$

where

$$f_d(\omega) = \frac{1}{2}\sum_{k=1}^{L_1}|m_k|^2 f(\omega-k\omega_0)$$

and $\lambda(\omega) = \dfrac{1}{2\pi}\int\limits_{-\infty}^{\infty} k(\tau)e^{-i\omega\tau}d\tau$.

So

$$\hat{f}_d(\omega) = \frac{1}{2}\sum_{k=1}^{L_1}|m_k|^2 \lambda(\omega-k\omega_0).$$

Since $\lambda(0) \le \tau_p$ then the peak values do not equal the power of separate harmonic and change if τ_p changes. Therefore, it is necessary to divide continuous and discrete constituents of spectrum and their separate analysis using corresponding methods. It is in particular important for monitoring of mechanisms since discrete and continuous constituents can be caused by different types of defects.

Evaluation of a period is the initial stage of selection and analysis of deterministic constituent of vibration oscillations. It is necessary to note that the accuracy of period evaluation should be sufficiently high in order to reach the minimum displacement of initial averaging point. Period evaluation is carried out using the method of least squares because in this case we can consider total power of selected harmonics of the deterministic constituent that increase evaluation effectiveness. It should be noted that a systematic error of evaluations of the least squares method of period
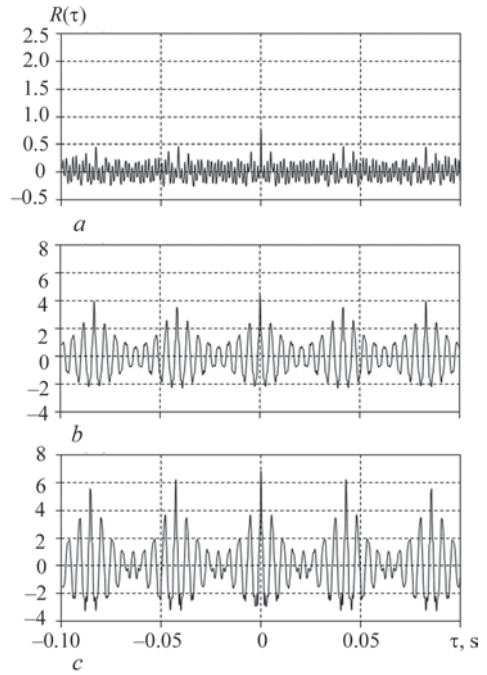

Figure 3. Evaluations of correlation function of filtered signals for three stages of development of defect of gear tooth

has $O(T^{-2})$ order and root-mean-square value of a random error $O\left(T^{-\frac{3}{2}}\right)$ [4].

Dependencies of a quadratic functional, calculated by [3], from a trial frequency for three stages of failure of gear is presented on Figure 5. The points of maximum of functional for each of three stages with accuracy up to three characters after coma correspond to basic evaluation of frequency and equal $\hat{f}_0 = 24.206$ Hz (Figure 5, a), $\hat{f}_0 = 24.055$ Hz (Figure 5, b) and $\hat{f}_0 = 23.423$ Hz (Figure 5, c) respectively. Cal-
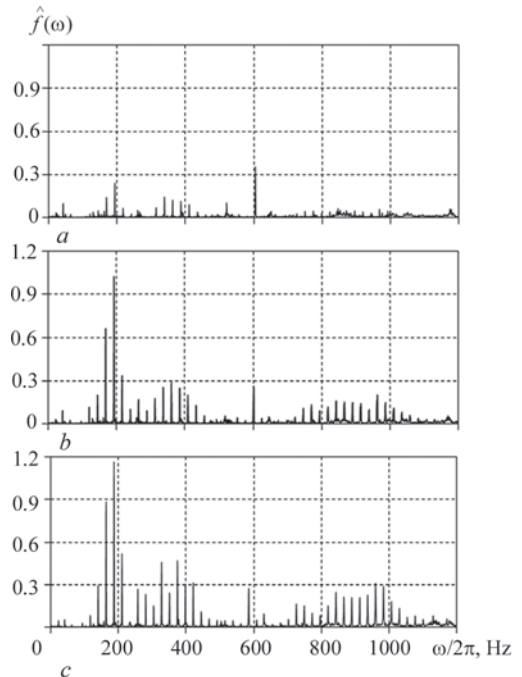

Figure 4. Evaluations of spectral density of power of filtered signals for three stages of development of defect of gear tooth
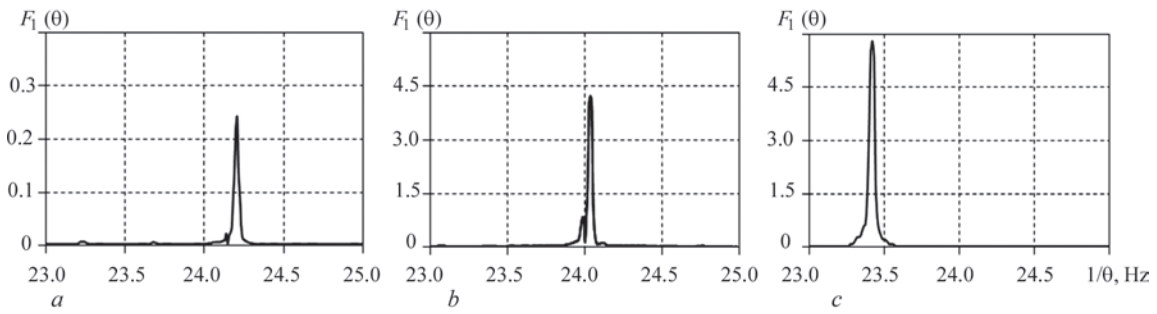
Figure 5. Dependence of quadratic functional of first order on test frequency for three stages of development of defect of gear tooth

culated values of the main frequency of deterministic oscillations are close to the values obtained by means of tachometer measurement, namely 24.192; 24.047 and 23.412 Hz.

Following from the calculation values of the basic frequency there were calculated the amplitudes of harmonics of deterministic constituent of vibration that are presented on Figure 6.

First harmonics of spectra of the deterministic constituent can be interpreted as orders of harmonic of a shaft rotation frequency. Twenty fifth harmonic corresponds to the first harmonic of coupling frequency and frequencies of higher harmonics are linear combinations of frequencies of coupling and rotation frequency. On the first stage of defect development the amplitude of harmonic of coupling frequency is the largest. Increase of damage provokes domination of the harmonics of 6–9th orders, however a general view of amplitude spectra remains similar. Sum of amplitudes of the harmonics for levels of defect development equals 3.47, 7.44 and 10.50, respectively, whereas sum powers of the harmonics equal 0.36,

3.52 and 4.63. Calculated according to [3] values of indicator I_1 change from 2.14 to 3.03 and I_2 indicator from 9.87 to 12.8. Based on the sine and cosine Fourier coefficients [1] it is possible to calculate evaluation of PCRP mathematical expectation for all time moments $t \in \left[0, \hat{P}_1 \right]$ (Figure 7).

On the assumption of [1, 17] and taking into account calculated values of the correlation function it is possible to make a conclusion that for set length of realization a standard deviation $\sigma \left[\hat{m}(t) \right]$ of evaluation of mathematical expectation is less than 0.01. Deterministic oscillations have a group structure and time intervals between the groups are close to a period of shaft rotation and each group consists of approximately eight oscillations.

Further analysis of condition of the gearbox was carried out based on the centered vibration signals obtained by means of subtraction from a signal of evaluation of PCRP mathematical expectation, i.e. $\overset{\circ}{\xi}(t) = \xi(t) - \hat{m}(t)$. Evaluations of correlation function of the centered signals (Figure 8) have a shape of slowly damped groups which follow one by one with
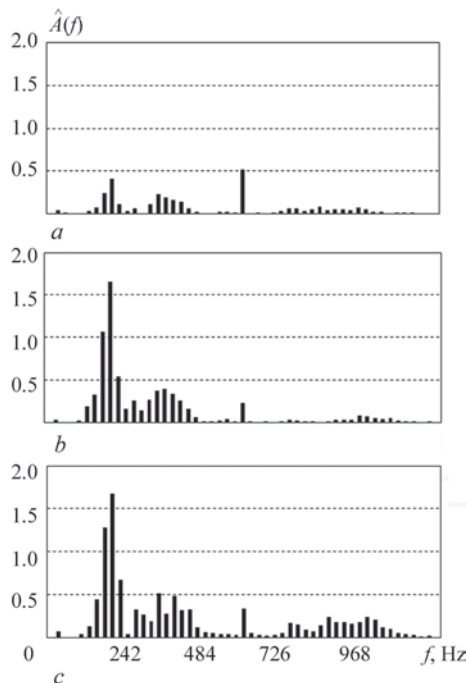

Figure 6. Amplitude spectra of oscillations deterministic constituent for three stages of development of defect of gear tooth
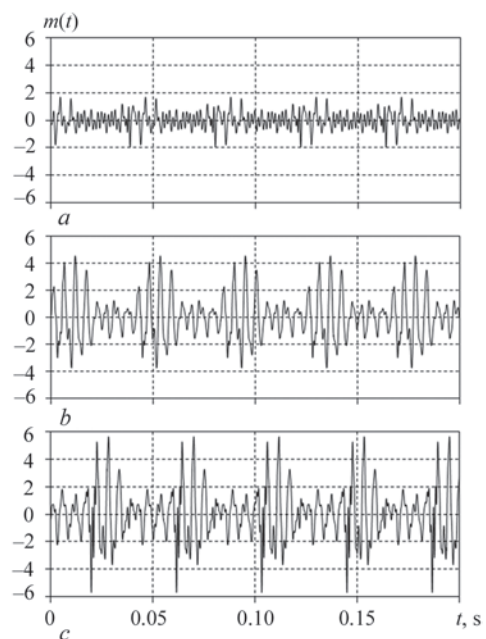

Figure 7. Evaluations of mathematical expectation of vibration signal for three stages of development of defect of gear tooth
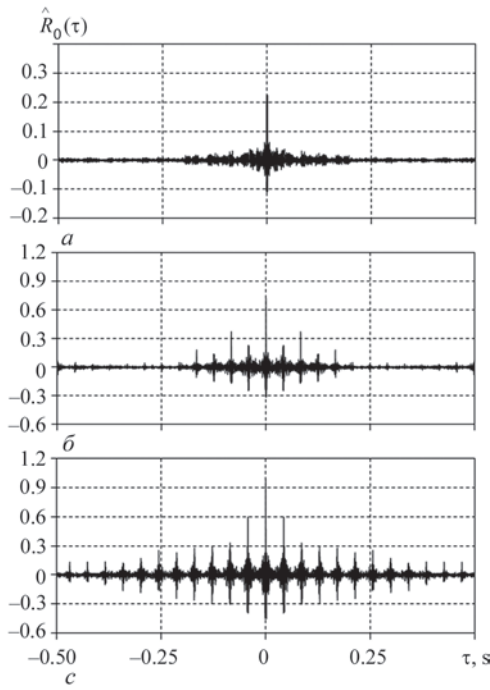
Figure 8. Evaluations of correlation function of stochastic constituent of vibration for three stages of development of defect of gear tooth

Figure 9. Evaluations of spectral densities of stochastic constituents of vibration in area of low frequencies for three stages of development of defect of gear tooth

rotation period. These groups become clearly noticeable for the second (Figure 8, *b*) and third (Figure 8, *c*) stages of defect development. The values of evaluation with increase of a shear τ decrease to fluctuations of small power, so deterministic oscillations are completely separated from vibration signal.

Spectral densities of the stochastic constituent of vibration signals contain only continuous constituent of a signal (Figure 9, 10). A comb-like shape of evaluations of the spectral densities indicates a narrow-band modulation of bearing harmonics of PCRP of low- and high-frequency range. This means that the modulating processes can be represented in form of sum of low-frequency and high-frequency narrow-band constituents which can be modeled using Rice's representation [5]. The conclusions on correlations or absence of correlations between these constituents in the range of low- and high-frequency areas can be made only based on the results of PCRP-analysis.

Dependencies of LSM functional [3] on a test frequency for each stage of failure of gear tooth contain a clearly determined peak (Figure 11) in a point which is considered as evaluation of a period of dispersion or main frequency. The evaluated values of main frequency f_0 equal 24.196, 24.075 and 23.423 Hz.

These values also insignificantly differ from the main frequency evaluations of mathematical expectations of vibrosignals. The clearly defined peak on a diagram on Figure 11, *a* corresponds to early stage of defect appearance. Taking into account powers of the peaks on Figure 11, *b*, *c* the conclusion is made on a
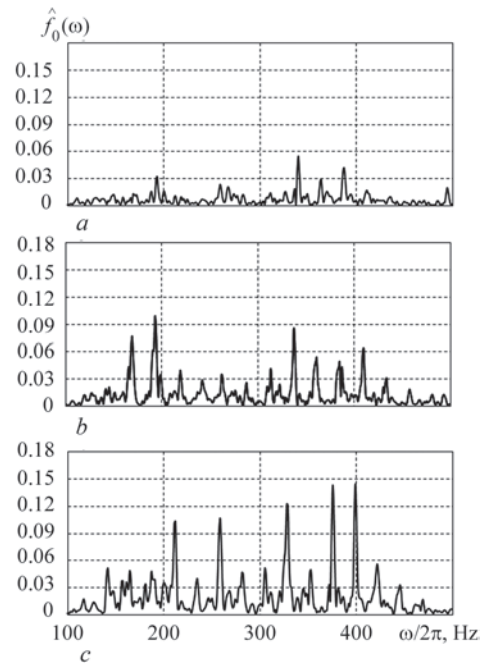
presence of developed defect. An amplitude spectrum of change of dispersion in time (Figure 12) was calculated having the information about $\hat{f}_0$ value.

Figure 13 shows the statistics diagrams

$$\left| \hat{R}_k \left(0, \theta \right) \right| = \left[\left[R_k^c \left(0, \theta \right) \right]^2 + \left[R_k^s \left(0, \theta \right) \right]^2 \right]^{\frac{1}{2}}.$$

As can be seen from Figure 13, the diagrams contain no dominating extremums based on which it is difficult to make any conclusions as for defect development.
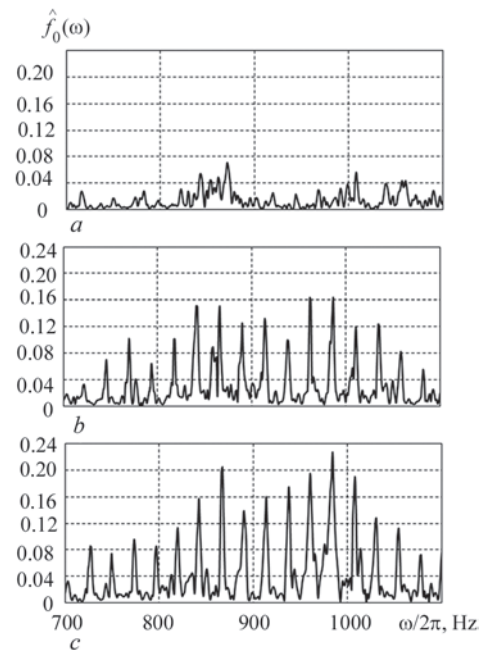

Figure 10. Evaluations of spectral densities of stochastic constituents of vibration in high-frequency area for three stages of development of defect of gear tooth
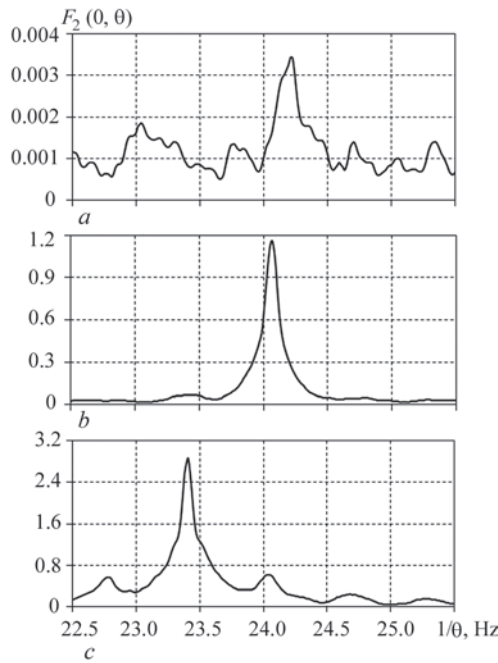
Figure 11. Dependencies of quadratic functional of second order on test period for three stages of development of defect of gear tooth

Amplitude spectra of dispersion $\hat{V}(k\hat{f}_0)$ (Figure 12) slowly drop down with increase of frequency that is especially typical for two last stages of defect development. Spectral constituents distributed on frequency for more than 280 Hz are weakly correlated. Therefore, the low-frequency and high-frequency modulations are non-correlated. An indicator is formed for this peculiarity consideration:

$$I_4 = \frac{\Delta \hat{R}_0(0) + \sum_{k=1}^{L_2} \hat{V}(k\hat{f}_0)}{\hat{R}_0^{(i)}(0)}, \qquad (2)$$

where $\Delta \hat{R}_0(0) = \hat{R}_0^c(0) - \hat{R}_0^{(i)}(0)$. Indicator I_4 has the following values, namely 1.29, 13.82 and 30.72, respectively, for each stage of defect development. Significant increase of I_4 indicator is an evidence of its high sensitivity to change of condition of gear pair.

It should be noted that the indicators used in the work differ from the indicators of cycle stability. A condition of gearbox is described by relationship of a power of change in time of mathematical expectation or dispersion to the initial quantities of these values, but not to an averaged by time dispersion for each condition. The latter significantly changes with defect development. Therefore, it is reasonable to take into account these changes as it was shown above.

Figure 14 shows the diagrams of dispersion change in time. These changes contain a significant projection caused by defect of gear tooth in a time interval which equals a nonstationarity period. These projections are particularly strong for two last stages when a defect of tooth is well developed and close to failure.

A failure of gear tooth was verified after a regular check of the gearbox by a group of maintenance staff (Figure 15). A relative standard deviation of evaluation of correlation function $\sigma_r[\hat{R}(t,0)]$, calculated by [1, 4] for set length of realization is less than 0.04.

Specific features of the damage can also be determined based on the analysis of correlation functions of stochastic constituent of vibration signal (Figure 16).

In this case the correlation oscillations are a superposition of damped waves with close frequencies $\mu_0 \pm k\omega_0$, where μ_0 is the resonance frequency of gear pair.

PCRP methods of vibration analysis proposed in [1, 4] for early defect detection differ from the meth-
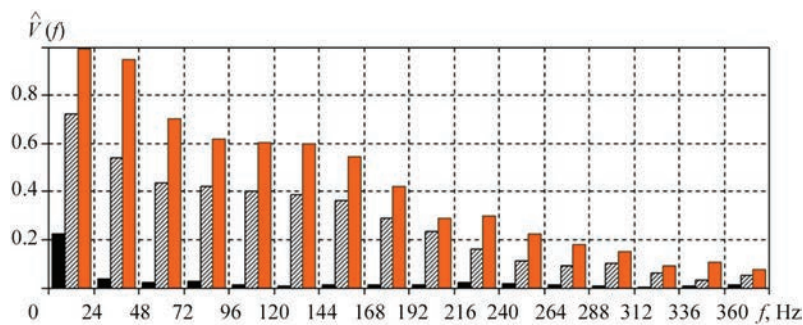

Figure 12. Amplitude spectrum of periodic changes of dispersion for three stages of development of defect of gear tooth

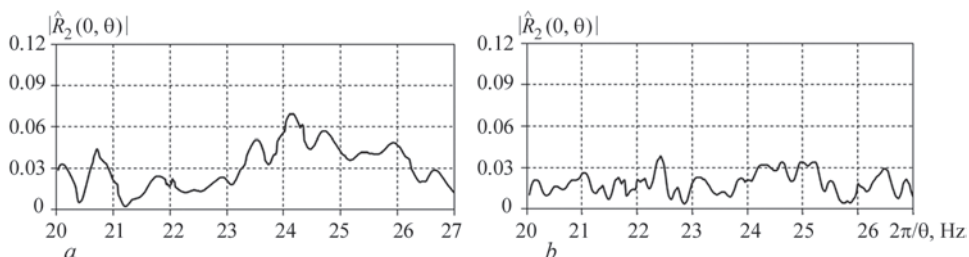**Figure 13.** Dispersion of constituents of first (*a*) and second (*b*) functional for first stage of defect development
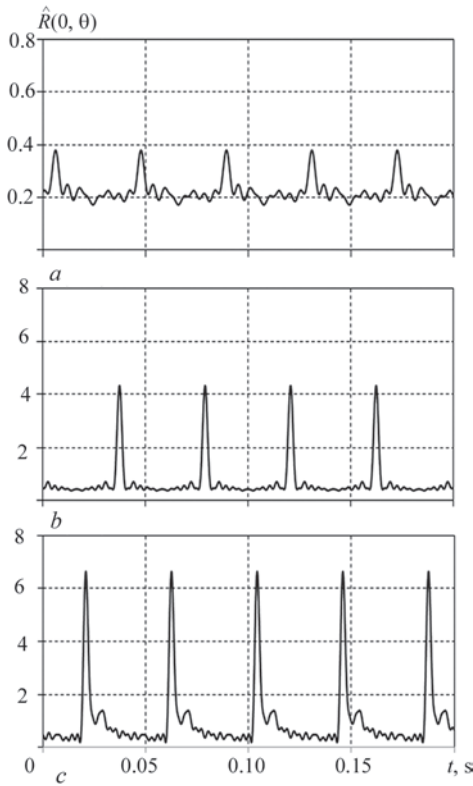
Figure 14. Evaluations of dispersion function of stochastic constituents of oscillations for three stages of development of defect of gear tooth

Figure 15. Photo of driving gear tooth of gearbox

possibility to get the evaluations of corresponding amplitude spectra, which can be used as a basis for evaluation of technical state of machine. An amplitude spectrum of dispersion is determined by modulus of correlation constituents (cyclic functions) in a point with shear $\tau = 0$:

$$\left| R_k\left(0\right) \right| = \int_{-\infty}^{\infty} f_k(\omega)d\omega \quad k = \overline{1, L_2}.$$

An amplitude of separate harmonics of k series is a sum characteristic of correlation of spectral harmonics, frequencies of which are displaced for $k\omega_0$. Summarizing amplitudes of all series a sum characteristic is obtained for all possible correlations of spectral

ods of so-called cycle stationary analysis being traditionally used in literature [5–10].

The cycle stationary analysis includes the calculation of cyclic autocorrelation function depending on time and shear and its 2D Fourier transformation, search of correlated harmonics, calculation of coherence functions and their integration, determination of so-called informative band of frequencies and different developed procedures of final consideration, etc. [11–18].

The PCRP analysis is carried out in a frequency-time area without transition into double-frequency area. A time structure of vibration signal was investigated based on expansion of moment functions of the first and second orders in Fourier series. The amplitude spectra of deterministic constituent of vibration and time changes of power for stochastic part are used for description of conditions of machines. Analysis in a stationary approximation is carried out for determination of the general properties of spectral content of oscillations and identification of frequency interval for detection of the hidden periodicies.

Effective methods of determination of the hidden periodicies of first and second order developed in [1, 4] provide identification of a period of deterministic oscillations and a period of time changes of moment functions of the second order for each separate realization with necessary accuracy. This provides the
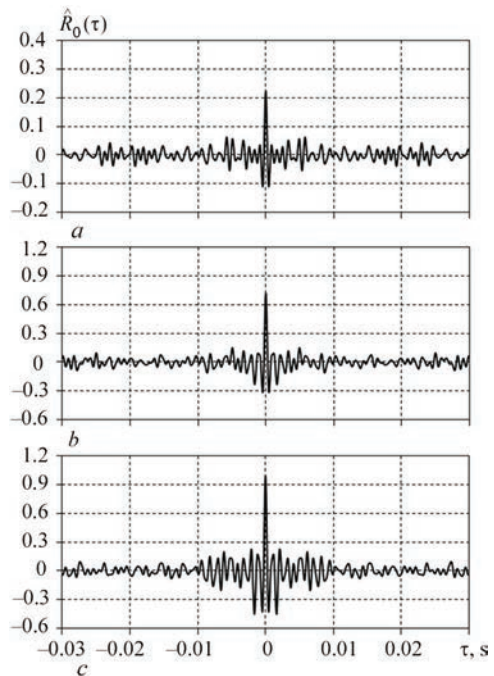

Figure 16. Dependencies of correlation functions of stochastic constituent of vibration signal for three stages of development of defect of gear tooth

Table 1. Stages of defect development

Indicator	Stage				
	Initial	Small	Medium	High	Dangerous
I_2	$I_2 < 0.5$	$0.5 \leq I_2 < 2.0$	$2.0 \leq I_2 < 4.0$	$4.0 \leq I_2 < 10.0$	$I_2 \geq 10.0$
I_4	$I_4 < 2.0$	$2.0 \leq I_4 < 10.0$	$10.0 \leq I_4 < 20.0$	$20.0 \leq I_4 < 25.0$	$I_4 \geq 25.0$

harmonics of the stochastic constituent of oscillations, however, this analysis is carried out only in a cyclic frequency area in scope of harmonic analysis of Fourier series.

Averaged by time power of the stochastic oscillations, determined by $R_0(0)$, rises with defect development. It causes inclusion of value of increment $\Delta R_0(0)$ in (2) for the indicator of defect detection. Thus, it can be expected that indicator I_4 formed based on all coefficients of Fourier dispersion, will be sensitive as much as possible to change of state of gear pair.

The time changes of dispersion in a general case are not localized in a frequency area. The maximum difference of frequencies between correlated harmonics is determined by the largest number of dispersion harmonic.

It should be noted that a dispersion of cyclic statistics, which is used in the analysis of "bypass square" [12, 14, 19, 20] has O(T^{-1}) order, whereas a dispersion of evaluation of basic part has O(T^{-3}) order and LSM evaluation provides significantly higher signal-to-noise ratio. Since amplitude of each separate harmonic for $|R_k(0)|$ dispersion is always less than $R_0(0)$, i.e. $|R_k(0)| \leq R_0(0), \ \forall \ k = \overline{1, L_2}$, then LSM evaluation has an obvious advantage in a hidden periodicities search.

For known basic frequency a cyclic (constituent) evaluation can be considered as a signal filtering with a transfer function in form of comb reaching the peaks in points $f = k\hat{f}_0, \ \forall \ k = \overline{1, L_2}$. These peaks become sharper (narrower) with increase of realization length. Such an approach allows increase of processing accuracy and elimination of laborious procedures being usually used for improvement of the traditional methods based on discrete Fourier transformation [10, 11]. The amplitude spectrum of deterministic constituent of oscillations and, first of all, the amplitude spectrum of time changes of power of oscillations stochastic constituent characterize defect features. The indicators formed on this basis can be effectively used for analysis of state of machines and mechanisms. Following from the numerical results of processing of time series of vibration signals of WPG gearbox it is possible to outline the stages of defect development (Table 1).

It should be noted that an emergency stage of defect development is characterized with a quick growth of both indices. It is recommended to use both these indices on practice. It is noted that the numerical values of indices were obtained based on the analysis of signal in up to 1 kHz frequency range.

CONCLUSIONS

It is shown that the parameters of the first and second series of PCRP vibration in $[0; 1.8f_p]$ frequency band are sufficiently sensitive to changes of mechanism condition and in full provide successful detection of defects and monitoring of their development.

LSM functional was used for detection of hidden periodicities of second order. Its dependencies on test period have sharp peaks in the points which are taken as periods of dispersion time changes. Presence of such peaks of increase indicates nucleation and development of a local damage. The sum amplitude of dispersion harmonics was taken for comparison of different stages of defect development. At that values of amplitudes for harmonics, order of which is more than twelve, were insignificant. This means that the spectral constituents, frequency intervals between which are more than 280 Hz, are low-correlated and, therefore, low-frequency and high-frequency modulations are non-correlated.

Dispersion does not contain time changes at defect absence. Therefore, it is relevant to choose an initial value of zero correlation constituent $R_0(0)$, determining average power of stochastic constituent of vibration oscillations, for quantitative characteristic of a change of the mechanism condition. An average power rises in process of defect development, so this increase was taken into account in the formula for stochastic indicator of the mechanism condition. It is shown that change of this indicator significantly overwhelms change of the "deterministic" indicator. The latter is determined by a power of deterministic constituents of oscillations, at that the power of the latter significantly overwhelms the power of stochastic constituents. Obtained results provide allows recommending the proposed stochastic indicator for monitoring of WPG gearbox.

REFERENCES

1. Javorskyj, I.M. (2013) *Mathematical models and analysis of stochastic oscillations.* PMI, Lviv [in Ukrainian].
2. Jaworskyj, I., Matsko, I., Yuzefovych, R., Zakrzewski, Z. (2016) Coherence function of interrelated periodically non-

stationary random processes. *Radioelectronics and Communication Systems*, **59**(3), 128–140. DOI: https://doi.org/10.3103/S0735272716030043

3. Javorskyj, I.M., Yuzefovych, R.M., Lychak, O.V. et al. (2022) Diagnostics of gear pair damage using the methods of biperiodically correlated random processes. Pt 1. Theoretical aspects of the problem. *Tekh. Diahnost. ta Neruiniv. Kontrol*, **4**, 4–11 [in Ukrainian].

4. Javorskyj, I., Kravets, I., Matsko, I., Yuzefovych, R. (2017) Periodically correlated random processes: Application in early diagnostics of mechanical systems. *Mech. Syst. Signal Process.*, **83**, 406–438. DOI: https://doi.org/10.1016/j.ymssp.2016.06.022

5. Antoni, J., Bonnardot, F., Raad, A., El Badaoui, M. (2004) Cyclostationary modeling of rotating machine vibration signals. *Mech. Syst. Signal Process.*, **18**(**6**), 1285–1314. DOI:https://doi.org/10.1016/S0888-3270(03)00088-8

6. Antoni, J. (2009) Cyclostationarity by examples. *Mech. Syst. Signal Process.*, **23**(**4**), 987–1036. DOI: https://doi.org/10.1016/j.ymssp.2008.10.010

7. Randall, R.B., Antoni, J. (2011) Rolling element bearing diagnostics – A tutorial. *Mech. Syst. Signal Process.*, **25**(**2**), 485–520. DOI: https://doi.org/10.1016/j.ymssp.2010.07.017

8. Randall, R.B., Antoni, J., Chobsaard, S. (2001) The relationship between spectral correlation and envelope analysis. *Mech. Syst. Signal Process.*, **15**(**5**), 945–962. DOI:https://doi.org/10.1016/mssp.2001.1415

9. Antoni, J. (2007) Cyclic spectral analysis in practice. *Mech. Syst. Signal Process.*, **21**(**2**), 597–630. DOI: https://doi.org/10.1016/j.ymssp.2006.08.007

10. Abboud, D., El Badaoui, M., Smith, W., Randall, B. (2019) Advanced bearing diagnostics: A comparative study of two powerful approaches. *Mech. Syst. Signal Process.*, **114**, 604–627. DOI: https://doi.org/10.1016/j.ymssp.2018.05.011

11. Wang, D., Zhao, X., Kou, L.-L. et al. (2019) A simple and fast guideline for generating enhanced/squared envelope spectra from spectral coherence for bearing fault diagnosis. *Mech. Syst. Signal Process.*, **122**, 754–768. DOI: https://doi.org/10.1016/j.ymssp.2018.12.055

12. Patel, V.N., Tandon, N., Pandey, R.K. (2012) Defect detection in deep groove ball bearing in presence of external vibration using envelope analysis and Duffing oscillator. *Measurement*, 45(**5**), 960–970. DOI: https://doi.org/10.1016/j.measurement.2012.01.047

13. Borghesani, P., Pennacchi, P., Randall, R.B. et al. (2013) Application of spectrum pre-whitening for the diagnosis of bearing faults under variable speed conditions. *Mech. Syst. Signal Process.*, **36**(**2**), 370–384. DOI:https://doi.org/10.1016/j.ymssp.2012.11.001

14. Betea, B., Dobra, P., Gherman, M.-C., Tomesc, L. (2013) Comparison between envelope detection methods for bearing defects diagnose. *IFAC Proc.*, 46(**6**), 137–142. DOI: https://doi.org/10.3182/20130522-3-RO-4035.00010

15. Antoni, J. (2006) The spectral kurtosis: A useful tool for characterizing non-stationary signals. *Mech. Syst. Signal Process.*, 20(**2**), 282–307. DOI: https://doi.org/10.1016/j.ymssp.2004.09.001

16. Antoni, J., Randall, R.B. (2006) The spectral kurtosis: Application to the vibratory surveillance and diagnostics of rotating machines. *Mech. Syst. Signal Process.*, 20(**2**), 308–331. DOI: https://doi.org/10.1016/j.ymssp.2004.09.002

17. Wang, D., Tse, P.W., Tsui, K.L. (2013) An enhanced Kurtogram method for fault diagnosis of rolling element bearings. *Mech. Syst. Signal Process.*, 35(**1–2**), 176–199. DOI: https://doi.org/10.1016/j.ymssp.2012.10.003

18. Sawalhi, N., Randall, R.B., Endo, H. (2007) The enhancement of fault detection and diagnosis in rolling element bearings using minimum entropy deconvolution combined with spectral kurtosis. *Mech. Syst. Signal Process*, 31(**6**), 2616–2633. DOI: https://doi.org/10.1016/j.ymssp.2006.12.002

19. Borghesani, P., Pennacchi, P., Ricci, R., Chatterton, S. (2013) Testing second order cyclostationarity in the squared envelope spectrum of non-white vibration signals. *Mech. Syst. Signal Process.*, 40(**1**), 38–55. DOI: https://doi.org/10.1016/j.ymssp.2013.05.012

20. Courrech, J., Gaudel, M. (1987) *Envelope analysis the key to rolling-element bearing diagnosis.* Brüel & Kjær, Denmark.

ORCID

R.M. Yuzefovych: 0000-0001-5546-453X,
I.M. Javorskyj: 0000-0003-0243-6652,
O.V. Lychak: 0000-0001-5559-1969,
G.R. Trokhym: 0000-0002-2472-1676

CONFLICT OF INTEREST

The Authors declare no conflict of interest

CORRESPONDING AUTHOR

R.M. Yuzefovych
G.V. Karpenko Physico-Mechanical Institute
of NASU
5 Naukova Str., 79060, Lviv, Ukraine.
E-mail: roman.yuzefovych@gmail.com

JOURNAL HOME PAGE

https://patonpublishinghouse.com/eng/journals/tpwj

TECHNICAL-ECONOMIC INDICES OF OPERATION OF AC STEEL-MAKING FURNACE WITH APPLICATION OF CORED ELECTRODES

A.G. Bogachenko[1]**, L.A. Sidorenko**[1]**, I.O. Goncharov**[1]**, I.A. Neylo**[1]**, S.G. Kiyko**[2]**, I.N. Logozinskyi**[2]**, B.A. Levin**[2]**, K.N. Gorban**[2]

[1]E.O. Paton Electric Welding Institute of the NASU
11 Kazymyr Malevych Str., 03150, Kyiv, Ukraine
[2]PJSC Dneprospetsstal
81 Pivdenne Shose, 69000, Zaporizhzhia, Ukraine

ABSTRACT

For the first time in the world practice, several series of experimental melts (more than 60) were performed, during which graphitized composite (cored) electrodes of EGC (C) type were used, designed by the E.O. Paton Electric Welding Institute. It is shown that a "cored" arc is fundamentally different in geometrical and power parameters from the arc of a monolithic electrode. A "cored" arc is dispersed, spatially stable and has a high stability in a wide range of lengths and electrical modes. This is especially important during the formation of wells and charge melting. A cored electrode (depending on the composition) provides a 2–5 times decrease in time from the first short circuit to a stable arc burning as compared to a monolithic electrode; 2–4 times reduction in harmonic factor; 6–16 % saving of electric power; 12–23 % growth of furnace output, etc. Cored electrodes improve almost all technical and economic indices of the furnace operation, providing the ability to control high-current arcs and their high stability.

KEYWORDS: electric arc, short circuit, saving of electric power

INTRODUCTION

In recent decades, the world metallurgy has been characterized by a continuous growth in steel production. Thus, in 2012, the total steel production amounted to 1517 bln t, in 2017 it was 1691 bln t and in 2019 it reached already 187 bln t, in 2021 it was 1950 bln t. At the same time, about a third of its total amount is electric steel. The share of electric steel is also constantly growing and currently amounts in Europe to about 42 %, in the USA it exceeds 60 %, in China and Asia it is about 20 %. In countries where ferrous metallurgy appeared relatively recently (Luxembourg, Indonesia, Saudi Arabia), steel is produced only in electric arc furnaces of alternating current (EAF) and of direct current (EAF DC). It is also important to note that in metallurgical production in order to solve problems of environmental safety, the advantage is given to electrometallurgical technologies.

The growth in the production of electric steel occurs simultaneously with the continuous improvement in the design of furnaces, power sources, preparation of charge, melting modes, out-of-furnace steel processing, heat treatment, etc. At the same time, manufacturers of graphitized electrodes are effectively working to improve the electrical and mechanical characteristics of electrodes, provide uniformity of properties in the volume of electrodes, increase their length, etc. Electrodes with protective coatings that reduce the intensity of lateral oxidation are used quite successfully.

Some successful research works are known, in which the properties of electrodes were improved by applying functional layers on their surface. However, such electrodes were not used in industry because of their high cost.

Quite a lot of attention is paid to studying properties of arcs, possibilities of their stabilization in order to effectively improve technical and economic indices of operation of arc furnaces. Thus, hollow electrodes were successfully tested, which provided arc stabilization, increase in furnace output and cos φ, saving of electric power, etc. However, cavity in the electrode causes a sharp increase in its loss (by 20–25 %) as compared to conventional monolithic electrodes. For this reason, hollow electrodes are not widely used in industry.

EXPERIMENTAL

At the E.O. Paton Electric Welding Institute for EAF and EAF DC, fundamentally new — graphitized composite (cored) electrodes (EGC (C)) were designed and investigated. The concept of the work consists in creating favorable thermodynamic conditions in the near-cathode region of a graphitized electrode to ionize gases in the arc column. Based on that, for manufacture of a cored electrode, a standard (monolithic) electrode is used, in which one or more vertical holes are made, which are filled with different functional materials, incl. those, containing elements of the Periodic Table with a low electronic work function, forming a solid insert (core) [1].
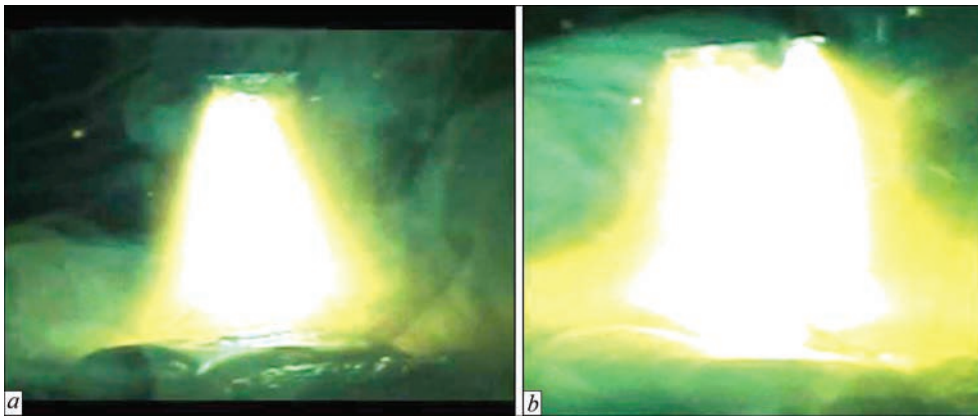
Figure 1. General appearance of the arc of a graphitized monolithic electrode (*a*) and a cored electrode (*b*) (U_A = 60 V, I_A = 700 A; d_C; d_{AN}; L_A, mm: ≈2.5; ≈10; ≈ 11 (*a*) and ≈8.5; ≈16.5; ≈16.5 (*b*) respectively)

The investigations of temperature dependence of electric resistance of cores of different composition, volt-ampere characteristics and cathode processes were carried out in the specialized laboratory units developed at the E.O. Paton Electric Welding Institute with the use of modern software, photo recording and computer equipment. At this stage of works, graphitized electrodes of 50 mm diameter were used. In the industrial furnace, electrodes of 300 mm diameter with the cores of different composition (F_{16}, F_{18}, F_{19}, F_{20} and F_{21}) and control devices showing voltage, current and melting capacity were used. To record current and voltage, the registering "REKON-09MA" archiver was used.

Comprehensive industrial tests of cored electrodes were first carried out in 12 ton EAF DC with the use of different charge, melting modes, core compositions, etc. It was found that the arc of a cored electrode is always maintained on the core, does not migrate along the end of the electrode and fundamentally differs from the arc of a monolithic electrode (at equal voltages and arc currents) in geometrical and energy parameters, Figure 1.

Thus, the volume of the arc of a cored electrode is 3–7 times higher than that of a monolithic electrode, and, accordingly, all parameters referred to a unit surface or volume of the arc of a cored electrode are significantly lower than those of a monolithic electrode. It is very important that the voltage drop in the near-cathode region of the arc of a cored electrode is 2–3 times lower than that of a monolithic electrode. At the same parameters, the arc length of a cored electrode (L_{AC}/L_{AM}) is 1.3–1.5 times longer. Due to the operation of emitters, the same current is provided at a voltage of 1.5–2.0 times lower on a cored electrode than on a monolithic one. At the same voltages, the arc current of a cored electrode, respectively, is 1.5–2.0 times higher, etc.

Due to the mentioned features, the arc of a cored electrode is distinguished, first of all, by a high stability – the main technological and energy factor in a wide range of lengths and electrical modes. A high stability of the electrical mode also determines a high stability of the thermal mode of the furnace, the thermal field

of the electrodes, a complete running of physicochemical processes, and as a result, the improvement of all technical and economic indices of the furnace. Such an arc is also characterized by a high spatial stability, it is dispersed and elastic, i.e. it more rarely breaks off under the action of external factors (for example, charge downslide, etc.). The arc of a cored electrode also poorly reacts to "magnetic blow". Due to the noted features and advantages, cored electrodes in EAF DC-12 industrial furnaces provided 7–10 % saving of active electric power; 20–23 % reduction in reactive power; increase in cos φ from 0.48 to 0.74; 15–20 % increase in furnace output; 12–15 % decrease in loss of alloying elements; 8–12 % reduction in noise of the operating furnace; 2–3 times reduction in dust and gas emissions [2].

Currently, about 1200 electric arc furnaces are operating in the world, incl. about 200 DC furnaces and, accordingly, 1000 AC furnaces. AC furnaces with a capacity of 100–180 t are widely used in Europe, America and Asia. Actually, such furnaces represent high-speed aggregates for melting a steel semi-product, alloying, degassing and finishing of which according to other parameters is carried out in a ladle furnace and a vacuum degasser.

Such furnaces require electrodes of a high quality, large diameter and length with a low electrical resistivity (at the level of 5 µOhm·m). The production of electrodes with a diameter of 810 mm and a length of up to 3500 mm has already been mastered, and the admissible current density reached the level of 40 A/cm². For manufacture of large-sized electrodes, expensive oil needle coke and unique equipment are used. The cost of such electrodes can reach 30 % of the cost of the produced steel. Therefore, the possibility of using cored electrodes in AC furnaces was of undoubted interest for us.

RESULTS AND DISCUSSION

The first industrial experimental melts were carried out in 2018–2019 in a 6-ton three-phase EAF of the type DS-6N1. The graphitized electrodes of 300 mm diameter were used. Five compositions of cores were
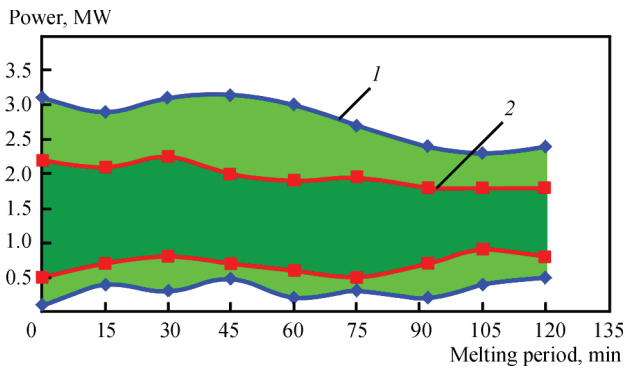
Power, MW

Figure 2. Range of power spread in the DS-6N1 furnace with the use of monolithic (*1*) and cored (*2*) electrodes (average statistical data on power are given with an interval of 15 min)

tested. More than 60 melts were carried out, on which practically the same type of charge — compact lumpy scrap with up to 30 % additives of the total weight of charging chips of power grinding of high-speed steels (HSS) was used. The melts were carried out with different combinations of cored and monolithic electrodes operating simultaneously in the furnace: three cored, 2 cored and one monolithic, one cored and two monolithic electrodes. For an adequate comparison of the results, the melts were carried out on standard electrical modes with the fixation of current and arc voltage signals.

As in the case of DC furnaces, first, a high stability of the electric mode in the DS-6N1 furnace was noted. Figure 2 shows, that in all periods of melting (arc stabilization, formation of wells, charge melting, finishing of liquid metal), the power fluctuation on cored electrodes is 20–30 % lower than on monolithic electrodes. A stable electrical mode is provided by a high current stability and lower distortions of sinusoidal voltage curves (Figure 3). Records of oscillograms of the main energy indices of melts are given in Table 1.

From Table 1, it follows that depending on the composition of cores:

● time of frequent arc breaks in cored electrodes is 3–10 times shorter than in monolithic ones;

● time of arc stabilization from the first interphase short circuit to a continuous burning in cored electrodes is 1.75–5.4 times lower than in monolithic ones.

These factors determine a rapid stabilization of the electric melting mode, a rapid formation of wells and the efficient melting of charge. It also results in decreased frequency and strength of current rushes into the primary network, which improves the quality of electric power, providing more stable operation of such powerful consumers of electric power as neighboring furnaces, units for secondary treatment, rolling mills, etc.:

● cored electrodes provide a higher cos φ and, as a result, a decrease in reactive power and power losses, which leads to a decrease in power consumption and the possibility of stable operation of the furnace at low currents;

● cored electrodes provide low harmonic factors, which also contributes to an improved quality of electric power.

It was found that during melting in a standard mode with the use of monolithic electrodes, the arc length is 50–70 mm, on cored electrodes it is 70–105 mm (1.4–1.5 times more), while maintaining the stability of the electrical and technological parameters of melting.

On cored electrodes, modes with an increased arc voltage "unloading mode" (from 150–160 V to 180–190 V) and reduced current (from 8.0–8.5 kA to 6.5–7.0 kA) were also tested. At the same time, the length of the arcs increased, cos φ increased and stabilized at the level of 0.92–0.94, the harmonic factors decreased to 0.28–0.08. This corresponds to modern concepts and the feasibility of operation of electric arc furnaces on long arcs and lowered currents. First of all, the noted features of cored electrodes provide their effective use on long arcs in furnaces of an old design, where the possibilities of the power source for the secondary voltage are limited and, secondly, they can expand the power and technological capabilities of modern ultra-high-power furnaces.
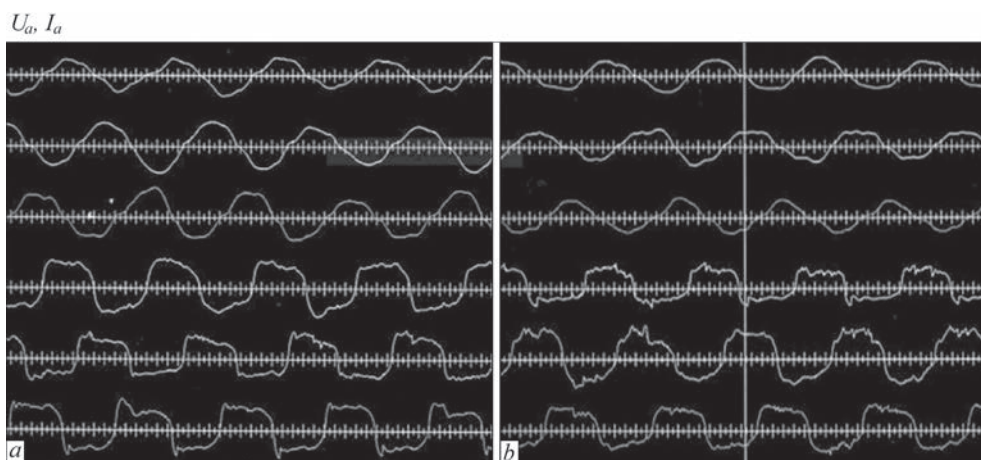

Figure 3. Typical curves of voltages and currents for cored (*a*) and monolithic (*b*) electrodes during penetration of "wells" and charge melting

Table 1. The main energy parameters of melts on AC furnace with monolithic and cored electrodes

Parameter	Type of electrodes				
	Monolithic	F_{16}	F_{18}	F_{19}	F_{20}
Time of frequent arc breaks from the furnace switching, s	Standard electrical mode				
	Up to 30	Up to 10	Not more than 3	Not more than 3	Not more than 3
Time of continuous arc burning, s	Up to 70	Up to 40	Not more than 13	Not more than 13	Not more than 13
cos φ	0.81–0.86	0.90–0.93	0.91–0.94	0.91–0.94	0.91–0.94
Factors of harmonic	0.65–0.59	0.58–0.28	0.36–0.09	0.36–0.09	0.36–0.09

On cored electrodes the forced melting modes (150–160 V and the current increased to 9–10 kA) were also tested. In this case, the length of the arcs decreased to 20–25 mm, an increased end loss of the electrodes, overheating of metal and slag under the electrodes and increased loss of alloying elements were observed. This mode is not recommended for melts on cored electrodes.

The characteristic feature of the cored electrode is the formation of a depression on its working end, which is always formed around the core. In the case of direct current, this depression has the shape of a hemisphere with rather thin walls in the lower part (Figure 4, *a*). In the case of alternating current, this hemisphere always has thicker walls (Figure 4, *b*).

The shape and depth of the hemisphere can be adjusted, since it depends on the composition of the core, electrical modes and has a significant effect on at least two important technological factors. First, the edges of the hemisphere shield the arc, having a significant effect on the degree of radiation of walls and roof of the furnace, i.e. on the life of the lining and, secondly, on the intensity of the end oxidation of the electrode (electrode consumption). At a sufficiently large depth of the hemisphere, up to 40–50 % of the arc power can be concentrated in it. In this case, the life of the lining can be increased by 30–40 %, but there will be an increased end consumption of the electrode. Thus, as a control object, the hemisphere at the working end of

the electrode should have optimal dimensions, taking into account the type of current, diameter of electrodes, composition of cores, etc. In addition, the presence of a hemisphere provides an effective operation on long arcs and lowered currents, which contributes, as noted above, to a decrease in the heating intensity of the cored electrode body and, as a consequence, to a decrease in the intensity of its lateral oxidation. Our studies showed that with the use of cores, the resistance of which is lower than the resistance of the electrode body, it is possible to redistribute the current over the cross-section of the electrode in such a way that its density in the core can be increased to 100–160 A/cm². Naturally, this factor also contributes to a decrease in the temperature of the electrode body and the rate of its lateral oxidation. Visually, this is confirmed by the fact that a lower, most heated part of the electrode (400–700 mm) has a shape close to a cylinder and not to a cone. In other words, on cored electrodes, in contrast to monolithic ones, the lateral oxidation rate is lower, and the lateral oxidation can be adjusted. However, the overall rate of oxidation of a cored electrode (electrode consumption) is lower than that of a monolithic one. This can provide saving of cored electrodes in AC furnaces. To prove this statement, a series of melts was carried out on standard modes, during which one cored electrode of the composition (F_{21}) and two monolithic electrodes were used. The consumption of electrodes was determined by weighing each electrode assembly before melting. The results of this
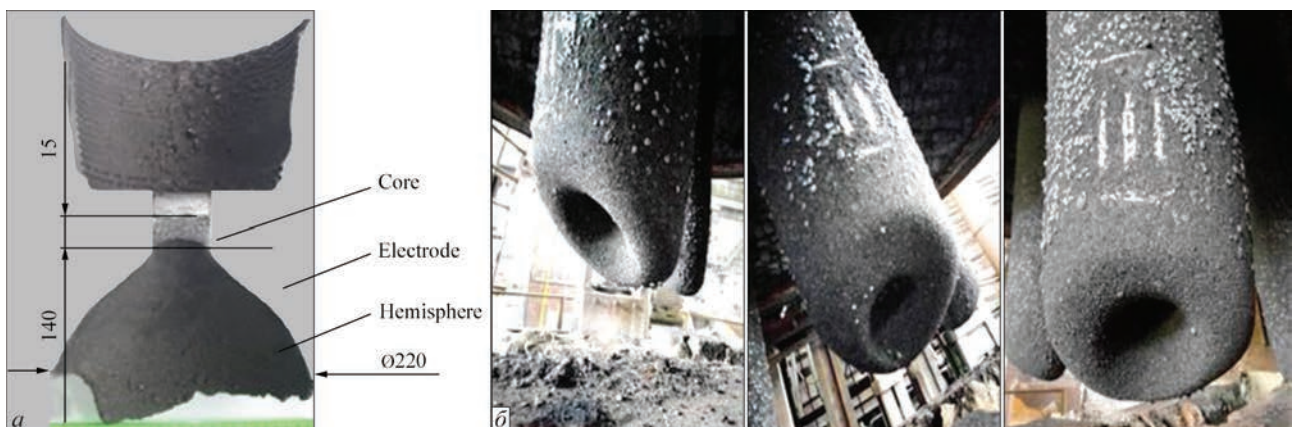

Figure 4. Macrostructure of the end of a cored electrode on direct current (*a*) and a general view of the ends of electrodes on three-phase alternating current (*b*); diameter of all electrodes is 200–210 mm
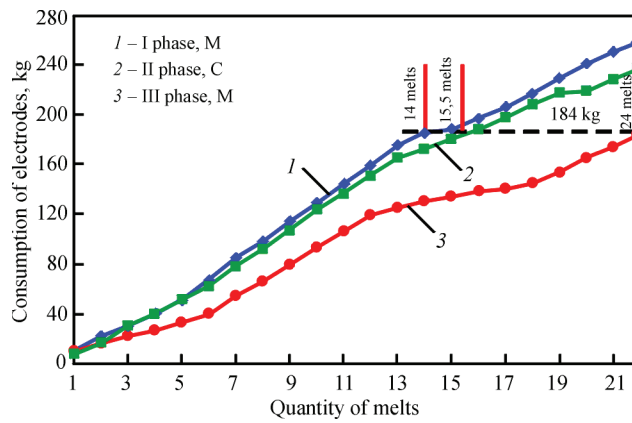
Figure 5. Dynamics of oxidation (burning loss) of electrodes in the furnace DS-6N1, determined by weighing electrode assemblies
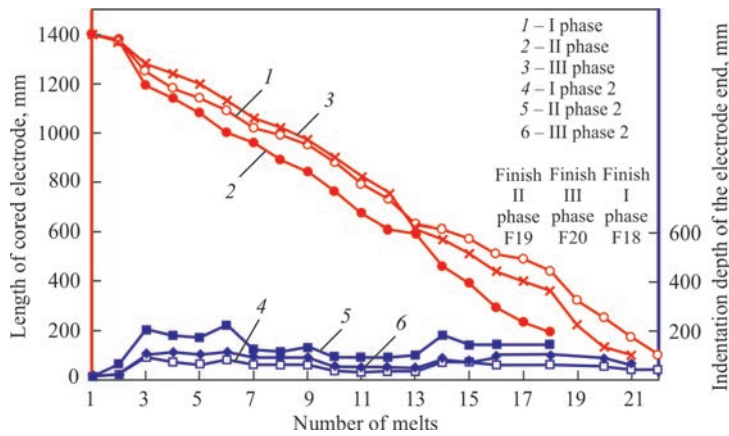

Figure 6. Dynamics of oxidation of cored electrodes of the III series (left diagram) and change in the indentation depth on the ends of the electrode (right diagram)

work are shown in Figure 5. From the mentioned data, it follows that monolithic electrodes (M) provided 14 and 15.5 melts, and cored electrodes (C) provided 22 melts. Therefore, an increase in the durability of a cored electrode by 25 % is observed. As was noted above, the composition of cores has a greater influence on the ratio of core resistances, electrode temperature, etc., which ultimately determines the cost of an electrode. A series of melts with the use of cores of three compositions (F_{18}, F_{19}, and F_{20}) clearly confirmed this statement, Figure 6. The consumption of electrodes was controlled by measuring their length before melting. The core of the composition F_{19} with a low electrical resistance worked out 18 melts, and the electrodes with the cores F_{18} and F_{20} (with a higher electrical resistance) worked out 22 and 21 melts, respectively.

It is known that as a result of the action of the skin effect, a central part of a graphitized electrode with 450 mm diameter or more does not conduct electric current, i.e. an inactive zone exists, the diameter of which naturally increases with an increase in the diameter of the electrode. The calculated averaged diameters of the inac-

tive zone depending on the diameter of the electrode at a frequency of 50 Hz, are given in Table 2 [3].

From the Table 2, it is seen that the electrodes of large diameters used in the industry in AC furnaces have a rather large inactive zone. Making a central hole in the electrode for a core (hollow electrode) already determines the flow of a current of a certain density along the walls of the hole by itself, i.e. a part of the current from the peripheral zones of the electrode goes into its central zone. Moreover, a core with a specific electrical resistivity, which is higher or lower than the electrical resistivity of the electrode body, can enhance or weaken the effect of current redistribution to the walls of the hole, regulating the rate of lateral oxidation of the electrode in such a way.

The production and operation of cored electrodes is featured by the fact that after the manufacture of the core, the electrode is not subjected to heat treatment, i.e. the core is put to the furnace in a "raw" state. Consequently, all processes associated with the formation of its structure and properties occur in the furnace in the process of heating and operation of the electrode. Natu-

Table 2. Relationship between electrode diameter (*D*), mm and diameter (*d*), mm of inactive zone for AC furnaces

D	400	450	500	550	600	650	700	750	800
d	0	45	80	110	180	220	270	328	385

rally, in this case, diffusion of the core components into the electrode body takes place, which form interlayer compounds, providing a significant increase in electrical conductivity (decrease in electrical resistance of the electrode body) [4]. Therefore, it is quite probably that for manufacture of cored electrodes, monolithic electrodes with a higher specific electrical resistivity can be used than it is common for a particular arc furnace. We also assume that it is possible to use cored electrodes with a smaller cross-section than in monolithic ones. Naturally, both of these factors are a significant case in saving graphitized electrodes. At the same time, the use of electrodes of a smaller diameter (mass) will reduce dynamic loads on the mechanical units and short mains of the furnace, which is very important at the beginning of melting in the period of charge melting.

Our experience of using electric arc with oxide cathodes [5], calculated data on the temperature of high-current arcs in ladle furnaces [6] and our data on the specific distribution of current and power in the arc of a cored electrode indicate that the temperature along the axis of the column of a cored electrode can be 12000–13000 K, i.e. by 15–20 % lower than on monolithic electrodes. This feature of cored electrodes can open up new opportunities for technologists in terms of optimizing melting modes, saving lining, extension of the furnace campaign, etc. In our opinion, a lower arc temperature of a cored electrode on a long arc will also significantly reduce the thermal load on the melt, reducing its overheating and contributing to reduce the loss of alloying elements and ferroalloys.

CONCLUSIONS

1. For the first time in the world practice, several series (more than 60 melts) of experimental melts with the use of cored electrodes of different composition were successfully carried out in a three-phase electric arc furnace of the DS-6N1 type.

2. It has been established that the arc of cored electrode is highly stable and provides, in particular, a 20–30 % lower power spread during melting.

3. It was found that depending on the composition of cores and melting mode, cored electrodes provide: 1.75–5.4 times reduction in time from the first short circuit to a stable arc burning as compared to monolithic electrodes; increase in cos φ from 0.81–0.86 to 0.91–0.94; reduction of harmonic factor from 0.65–0.59 for monolithic electrodes to 0.36–0.09 for cored electrodes; 6–16 % saving of active electric power; 12–23 % increase in furnace output; decrease in consumption of electrodes by 20–25 %.

4. We consider it necessary to continue these works on furnaces of a larger capacity, for example, 50 tons or more, as well as in order to determine the durability of the lining, saving of alloying, ferroalloys, further optimization of cores composition, a deeper understanding of power, technological and metallurgical features of melting with the use of cored electrodes as a means of efficient control of high-current arcs operation.

5. It is shown that the best energy performance on cored electrodes is provided by running on long arcs.

6. It has been established that it is not recommended to carry out melting in forced modes (short arcs) in relation to AC furnaces with cored electrodes.

7. The cost of materials and works for the manufacture of cored electrodes did not exceed 0.5 % from the value of the obtained economic effect.

REFERENCES

1. Paton, B.E., Lakomsky, V.I., Galinich, V.I., Mishchenko, D.D. (2011) Cored electrodes of electric arc furnaces. *Chyornye Metally,* **5**, 13–15 [in Russian].
2. Bogachenko, A.G., Mishchenko, D.D., Braginets, V.I. et al. (2016) Saving of electric power at the arc steel melting furnaces of direct current with graphitized cored electrodes. *Sovrem. Elektrometall.*, **1**, 58–64 [in Russian].
3. Okorokov, N.V., Nikolsky, L.E., Egorov, A.V. (1962) Influence of tubular electrodes on thermal operation of arc electric steel furnace. News of higher educational institutions. *Ferrous Metallurgy*, **9**, 105–110.
4. Fialkov, A.S. (1977) *Carbon, interlayer compounds and composite on its base.* Moscow, Aspekt press [in Russian].
5. Lakomsky, V.I. (1997) *Oxide cathodes of electric arc.* Zaporozhie, Internal [in Russian].
6. Krikent, I.V., Krivtsun, I.V., Demchenko, V.F. et al. (2018) Numerical modeling of high-current arc discharge in DC ladle–furnace installation. In: *Physical processes in welding and metal working: Collect. of articles and reports.* Kiev, 135–140 [in Russian].

CONFLICT OF INTEREST

The Authors declare no conflict of interest

CORRESPONDING AUTHOR

A.G. Bogachenko
E.O. Paton Electric Welding Institute of the NASU
11 Kazymyr Malevych Str., 03150, Kyiv, Ukraine.
E-mail: stemet@ukr.net

SUBSCRIPTION–2023

If You are interested in making subscription directly via Editorial Board, fill, please, the coupon and send application by Fax or E-mail.

12 issues per year, back issues available.

$384, subscriptions for the printed (hard copy) version, air postage and packaging included.

$312, subscriptions for the electronic version (sending issues of Journal in pdf format or providing access to IP addresses).

Institutions with current subscriptions on printed version can purchase online access to the electronic versions of any back issues that they have not subscribed to. Issues of the Journal (more than two years old) are available at a substantially reduced price.

Subscription Coupon Address for Journal Delivery				
Term of Subscription Since		20	Till	20
Name, Initials				
Affiliation				
Position				
Tel., Fax, E-mail				

The archives for 2009–2021 are free of charge on www://patonpublishinghouse.com/eng/journals/tpwj

ADVERTISING
in «The Paton Welding Journal»

Address
11 Kazymyr Malevych Str., 03150, Kyiv, Ukraine
Tel./Fax: (38044) 205 23 90
E-mail: journal@paton.kiev.ua
www://patonpublishinghouse.com/eng/journals/tpwj